DESIGN AND IMPLICATIONS OF A ROBOTIC PROSTHETIC LEG WITH LOW-IMPEDANCE ACTUATION

by

Toby B. Elery

APPROVED BY SUPERVISORY COMMITTEE:

Robert D. Gregg, IV, Chair

Yonas Tadesse, Co-Chair

Arif Malik

Tyler Summers

To my wife, Kristi, for supporting, loving,

and standing by me through every step of this journey.

&

To my parents, for equipping and preparing me for life,

and for your continual love and encouragement.

DESIGN AND IMPLICATIONS OF A ROBOTIC PROSTHETIC LEG WITH LOW-IMPEDANCE ACTUATION

by

TOBY B. ELERY, BS, MS

DISSERTATION

Presented to the Faculty of

The University of Texas at Dallas

in Partial Fulfillment

of the Requirements

for the Degree of

DOCTOR OF PHILOSOPHY IN

MECHANICAL ENGINEERING

THE UNIVERSITY OF TEXAS AT DALLAS

May 2020

ACKNOWLEDGMENTS

Getting to where I am today has been quite the journey, but one that I didn't take alone. First, I thank Jesus for the sacrifice he made for me, and for the life He provides. I am blessed beyond what I deserve or could ask for, and I thank God regularly for bringing me this far. Looking back, there have been so many people placed in my life who have supported me in one way or another and deserve my most sincere gratitude.

Someone I have to thank is my advisor, Dr. Robert (Bobby) Gregg. When I was a young undergraduate intern in your lab, you encouraged me to consider graduate school and offered the opportunity to conduct research with you on the graduate level. Making that decision was difficult, but completely worth it. It has become clear over the years that you truly care for your students and want what is best for them. Thank you for challenging me and fueling my passion for design and robotics. Working with you has been a privilege.

I also want to thank my committee members Dr. Tadesse, Dr. Malik, and Dr. Summers, for your commitment to students like me. Dr. Siavash Rezazadeh, thank you for your mentorship and friendship. I will forever be grateful for the many conversations and teachable moments we had together. Thanks to the research engineers Chris Nesler, Vamsi Pedinti, and Yoni Chatzinoff, who were extremely useful in neverending hardware implementation and troubleshooting of the prosthetic leg. To my LocoLab "class", Kyle, David A., and Edgar, it has been an absolute joy and pleasure starting, progressing, and navigating graduate school with you. Dario, David Q., Ge, Leon, Aaron, Anne, Saurav, Nikhil, Jon, Mark, Emma, Jianping, Taha, Alireza, and Amanda: thanks for all the fun and meaningful conversation and for making our lab so enjoyable. I also wanted to thank the many interns that I've had the pleasure to work with. I hope you benefited from working with me as much as I did with you. Specifically, thanks to Jim, Kayla, Sara, Lukas, PK, David M., Lizbeth, Jack, and Calvin for the efforts you dedicated to the prosthetic leg project. A special thanks to my

friends at the UTD Machine Shop, Mark Powell, Jerry Beavers, Kenny Sangston, Andrew Bittner, and Erik Temesi. You repeatedly helped me out when I was in a tight spot, and provided invaluable knowledge on designing for manufacturability. To Leslie Gray, Karen McCain, and Staci Shearin, thanks for your clinical expertise and help with experimentation.

To my parents, thank you for everything you've done, and continue to do for me. Mom, I know that over the years you have done everything possible to set me up for success, so thank you, I'll never forget it. You have taught me how to treat and love people, and are an example worth imitating. Dad, you taught me how to be joyful in life, and that anything is possible with hard work. Thank you for exemplifying what it means to be a man, father, and believer. I know sending me to school was difficult, and you both made sacrifices to make it possible. It is abundantly clear that you both have always believed in me, even when I didn't believe in myself. I couldn't have asked for better parents, I love and appreciate you both more than you know. Mitch and Amanda, thanks for encouraging me throughout school, and for always being someone I can talk to and laugh with. I love you both, I'm proud of you both, and I'm grateful that I can call you family.

Finally, to the person I hold most dear, my wife, my love, Kristi. It has taken over a decade to get here, and you have been by my side every step of the way. You are my biggest advocate. Your encouragement, love, and support has gotten me through every late-night study session, difficult homework problem, stressful exam, and lengthy paper. I hope you know that I would not be where I am, or who I am, without you. As far as I'm concerned, this achievement is not just mine, but ours. Although it's not enough to express my appreciation, thank you and I love you (to the moon and back, times infinity).

March 2020

DESIGN AND IMPLICATIONS OF A ROBOTIC PROSTHETIC LEG WITH LOW-IMPEDANCE ACTUATION

Toby B. Elery, PhD
The University of Texas at Dallas, 2020

Supervising Professors: Robert D. Gregg, IV, Chair
Yonas Tadesse, Co-Chair

Recent developments in the field of powered prostheses have produced several devices that implement a wide variety of actuation schemes, each presenting specific benefits and limitations to prosthetic design and acceptance of robotic prostheses. The work of this dissertation encompasses research focused on the design and implications of an actuation scheme new to robotic prosthetic leg design; low-impedance actuation. Although this style of actuation has shown promise in legged robots, it has potential benefits specifically relating to powered prosthetic legs as well. Such benefits include free-swinging knee motion, compliance with the ground, negligible unmodeled actuator dynamics, less acoustic noise, and power regeneration. To investigate these potential benefits a custom transfemoral (knee-ankle) robotic prosthetic leg with high-torque, low-impedance actuators was created. Preliminary benchtop testing established that both joints can be backdriven by small torques (~1-3 Nm), confirming the small reflected inertia and low impedance. The reduced joint-level impedance was achieved while maintaining the ability to produce very large torque (~180 Nm). Impedance control tests prove that the intrinsic impedance and unmodeled dynamics of the actuator are sufficiently small to control joint impedance without torque feedback or lengthy tuning trials. The negligible effect of the actuator's unmodeled dynamics is further demonstrated through

the direct implementation of biological impedances in amputee walking experiments. The regenerative abilities, low friction, and small reflected inertia of the presented actuators also offer practical benefits through reduced power consumption and acoustic noise compared to state-of-art powered legs. Although these benefits are mainly related to the physical device, this dissertation also extends the investigation into potential benefits to the wearer. Additional walking experiments were conducted with three amputee subjects to study how the powered prosthetic leg with low-impedance actuators affected gait compensations, specifically at the residual hip. A walking controller was implemented on the powered prosthesis to exploit the low-impedance actuators' power density during push-off, impedance control abilities in stance, and trajectory tracking abilities to ensure toe-clearance during swing. Results show that when large push-off power is provided, less work is demanded from the residual hip to progress the limb forward. Moreover, all subjects displayed increased step length and propulsive impulses for the prosthetic side, compared to their passive prostheses. These results reduce demand on the hip to accelerate the body forward and display the ability to improve gait symmetries. Hip circumduction improved for subjects who had previously exhibited this compensation on their passive prosthesis. The improvements made to these compensations lead to reduced residual hip power and work, which can reduce fatigue and overuse injuries.

TABLE OF CONTENTS

LIST OF FIGURES

LIST OF TABLES

CHAPTER 1

INTRODUCTION

1.1 Background

The first use of a lower limb prosthesis dates back to around 400 BC, however, most of what is recorded indicates that prostheses during this period were mostly wooden pylons [101]. This was the standard until around the 19th century when mechanisms such as simple hinge joints were introduced into prosthetic design [3]. Since then, passive prostheses have utilized more advanced mechanisms such as multi-bar linkages, springs, cams, and dampeners to mimic normative gait patterns. Furthermore, advances in materials, such as aluminum and carbon fiber, have led to lighter weight prostheses that can passively store and release energy. By storing and releasing energy in these elastic components, the prosthesis can repurpose energy that is otherwise dissipated, therefore returning some of the lost tendon functionality of the lower limb. Although these passive devices restore some functionality, amputees are typically left with an asymmetric gait [49] that is slower, less stable, and less energy-efficient than able-bodied locomotion [32, 73]. Such passive prostheses are mainly limited in functionality because the mechanisms they utilized can only dissipate or repurpose energy that the user introduces, and cannot inject or produce net-positive energy like legged muscles during gait. Passive prostheses are also limited in their functionality across tasks. Most devices are designed for level-ground walking conditions and do not adequately facilitate tasks such as sit-to-stand or stair ascent/descent. Semi-active prostheses attempt to address these issues by utilizing microprocessors to control the damping of joints with the use of small actuators that vary hydraulic valves during the user's gait [9, 55]. This is frequently implemented at the knee to control motion during the swing phase of gait. This approach allows for a single product to be adaptable to a variety of subjects, environments, and tasks. However, these are still energy dissipating devices, and cannot inject any energy into the user's gait.

Powered prostheses can actively inject energy into the user's gait, and therefore can restore muscle functionality, mobility, and quality of life to those who live with the loss of a limb.

1.2 Actuation Styles and Limitations

Since the development of the first powered prosthesis, several additional devices have been developed which implement a variety of actuation schemes. This section is dedicated to describing these schemes and pointing out their benefits and limitations.

1.2.1 Off-board Actuation

Early powered prosthetic designs, and some current, keep bulky actuators, power sources, and electronic components off-board the prosthesis. These prosthetic devices are typically tethered to their off-board systems through wires and flexible cables, which are used to transfer power from off-board actuators to the prosthesis. This allows the weight, volume, and complexity of the prosthetic device worn by the subject to be minimized. The prosthetic emulator presented in [14, 51] takes advantage of this design method by housing high-power and high-torque actuators off-board and transferring energy through Bowden cables to move the prosthesis's joints. Using this technique, researchers can explore a broad range of control and design schemes. For example, this approach prevents the prosthesis from being cluttered with actuator components and electronics, which can allow the implementation and control of additional degrees-of-freedom at the ankle. However, housing large portions of your system off-board prevents such devices from being self-contained. This has one obvious limitation, the inability to operate separately from the tethered system or outside a laboratory setting, which can pose challenges in testing and clinical acceptance.

Another style of off-board actuation uses hydraulic pumps to control onboard hydraulic cylinders. In fact, one of the first powered prostheses created was a hydraulically powered

prosthetic knee [29]. This device had an onboard hydraulic cylinder powered by an off-board hydraulic pump, computer and power source. It served as a proof of concept that powered prostheses could be useful to return normative gait mechanics to amputees. As stated previously, the main limiting factor of this style of actuation is the complication of consolidation into a single self-contained device. For this style of actuation to obtain clinical acceptance, the off-board hydraulic pumps must be mounted onto the device or user. However, such hydraulic pumps are often too heavy and bulky to be realistic in application. Moreover, many time-varying dynamic characteristics, such as fluid compressibility, limit the bandwidth of hydraulic actuation and increase control difficulty. Although researchers have increased this bandwidth by including sensors that characterize the changing real-time dynamics of the actuator [10], this further increases complexity and difficulty of self-containment.

Other devices have similarly used off-board pneumatic actuation. Such devices use powerful off-board air compressors to power pneumatic actuators, typically resulting in devices that are lightweight, compliant, and capable of producing large loads [20]. For example, the prosthetic leg presented in [114, 116] has pneumatic cylinders mounted to the prosthesis, with off-board air compressors, electronics, and power. Another similar, however slightly different method, uses off-board air compressors to power onboard artificial muscles, such as [18, 52]. These artificial muscles act as bladders that contract in length and expand radially when inflated, providing linear forces between its endpoints, and therefore torques at the prosthetic joints [41, 121]. Aside from the same limitations of autonomy (similar to hydraulic actuation schemes), this style of actuation only produced force in one direction. Therefore, a second antagonistic pneumatic actuator is required to control the joint in the opposite direction. Additionally, since this actuation style requires the muscles to expand in volume, the numerous muscles required for bi-directional motion can easily result in an overall prosthetic volume too large for everyday use.

1.3 Onboard Actuators

1.3.1 High-Impedance Actuators

In the last decade, a great amount of research and development has gone into the design and control of powered prosthetic limbs [57, 82, 120, 123, 127]. Many powered prosthetic devices have emerged from this research, most of which utilize electric motors for their compact size, allowing for simpler integration of the actuation onto the prosthesis [84, 82, 123]. Although the use of electric motors can aid in removing the need for a tether, some research devices still house their power and computing sources off-board for additional simplicity and reduced prosthetic weight, and therefore still require a tether.

For a prosthetic leg actuator to rely solely on an electric motor to achieve biological levels of joint torques and powers, an unreasonably large and heavy motor would be required. Alternatively, small motors have been coupled with high gear reduction transmissions to increase the actuator's torque density and reach biological levels of torque and power. The high-reduction transmissions in some powered prostheses consist of multiple stages of timing-belts, chains, or gears [7, 59, 131]. Other designs include linear ball screws that translate the rotational torque of the motor to linear force at the ball screw. This linear force is then applied to a lever arm to achieve rotational torque around the prosthetic joint [12, 16, 38, 48, 63, 64, 68, 86, 87, 115]. This is the most common actuation style implemented in robotic prosthetic legs, mainly due to its ability to increase torque and power, while maintaining a reasonable low volume and weight. Almost all powered prostheses that implement one of these high-ratio transmission schemes can be described as having high-impedance or low-backdrivability. This means that large forces are required to move the actuator's output when unpowered. Although increased transmission ratios do not strictly equate to high-impedance, they often exhibit high passive impedance. This is partially because joint-level reflected inertia is proportional to the transmission ratio squared. Therefore, as transmission ratios

increases, reflected inertias increase exponentially. Some designs bypass their high-impedance by including continuously varying mechanisms that actively reduce the transmission ratio, and therefore reflected inertia [63]. However, to take advantage of this design feature, the subject must stop their gait and unload the prosthesis while it adjusts. This can be useful when stopping between tasks but limits the prosthesis's real-time adaptability.

The high-impedance style of actuation has proven to have several benefits to prostheses through joint control-ability, torque density, and the ability to remove the tether. In fact, the only commercially available powered knee prosthesis implements this actuation style [77]. However, high-impedance actuation schemes have several limitations. For instance, they can increase torque density, but at the cost of transmission "transparency" [15], which is critical for the high-speed force control necessary in gait [104]. This means that the large mechanical impedance, from reflected inertia and frictional forces within these transmissions, limits the high-speed force and position control performance. A typical trade-off in the actuator selection within powered prostheses is between high torque density and low mechanical impedance. Since the weight of the device is a driving design factor, actuation design has been forced to choose torque density over low mechanical impedance. Moreover, the large frictional forces that result from the numerous meshed components within the transmission are very loud in nature, which hinders the clinical acceptance of powered devices. Lastly, the low-backdrivability of this actuation style limits its ability to exploit the passive dynamics of the leg to store or return energy, which increases power consumption and reduces untethered operational time.

1.3.2 Series Elastic Actuators

Series Elastic Actuators (SEAs) are another category of actuation within powered prostheses, such as the Open-Source Leg and Clutchable SEA [7, 95]. SEAs have a spring-like component between the actuator's motor and output, that stores energy during non-peak loading to be

used during peak loading conditions. This can be useful in minimizing motor requirements when designing an actuator and is even used in the only commercially available powered prosthetic ankle [6, 78]. Apart from energy, SEAs also provide benefits related to compliance. For instance, the added compliance can protect the hardware from damage and provide smoother transitions at ground impact. However, SEAs tend to greatly increase design complexity. Although work is being done to optimize the elastic element in SEAs [11], a single elastic element may not be suitable for varying tasks. This motivates work in the field of Variable Stiffness Elastic Actuators (VSEAs) [130, 2], in which the stiffness of the elastic element can vary. This, however, even further complicates the design, which often leads to increased weight and control difficulties. Additionally, elastic elements in SEAs can limit the available joint impedance [95]. Lastly, SEAs act as low-pass filters, thus slowing control loop frequency and torque bandwidth, which is critical for highly dynamic tasks such as walking.

1.4 Motivation for Low-Impedance Actuators

In efforts to alleviate issues with series elastic and high-impedance actuation in powered prosthetic legs, we draw inspiration from recent research in legged robots. In recent years, advances in electric motor technology have drastically increased their torque density. Legged robots such as the quadruped MIT Cheetah [103], biped ATRIAS [42], and others [50, 90], have embraced these advanced by implementing high-torque electric motors with low-ratio or no transmissions, which result in actuators with low mechanical impedance. Inspired by this approach, exoskeletons have also recently implemented high-torque electric motors in combination with low-ratio transmissions [69, 124, 134]. Advances to the torque-density of modern motor technology allows the pairing of powerful electric motors with low-ratio transmissions to remove the reliance on tethered or high-impedance actuation to achieve biological levels of torque or power.

The low-impedance style of actuation offers several benefits specific to robotic prosthetic legs. Opposite to high-impedance actuators, low-impedance actuation is often described as having high-backdrivability. This implies that relatively low forces are required to move the actuator's output when unpowered. This can facilitate a knee joint that can freely swing under its mass, which can result in a more natural gait and reduced power requirements during the swing phase. Similar to SEAs, the joint compliance of a low-impedance actuator can prevent hardware damage and provide a smoother touchdown impact with the ground, which can, in turn, improve system efficiency and comfort for the user. Moreover, during phases where negative work is done on the leg, the compliant nature of this actuation style can allow power to be regenerated and stored in the batteries, similar to energy storage in SEAs. Lastly, the low mechanical impedance from reduced friction and gear meshings can lead to a quieter device, which is a critical requirement when transferring this technology to the consumer.

With the wide range of control schemes available, the low-impedance style of actuation has additional benefits specifically relating to prosthetic control. The lower joint impedance (reflected inertias and frictional losses) of these actuators minimizes the effect of the leg's unmodeled dynamics, thus returning transmission "transparency". This can help simplify an otherwise complex control problem and lengthy tuning trials, through the direct implementation of biological impedances in low-level joint control. Force control in these actuators can be comparable to SEAs without their design complexities and bandwidth limitations. In fact, this actuation style is typically characterized by larger force magnitude and bandwidth, compared to traditional actuation styles. This can be leveraged to return large push-off ankle power in highly dynamic phases of gait, which is often saturated when using high-impedance actuation [59]. Returning this functionality can be useful toward improving loading symmetries in gait [99, 136], which have been linked to compensatory power at the residual hip [40, 105]. Furthermore, with less friction and inertia to slow down the system, this style

of actuation can display greater position bandwidth compared to high impedance actuation schemes. This can be specifically beneficial when controlling phases of gait that have rapid motion, such as quick ankle and knee flexion between terminal stance and mid-swing for increased toe-clearance [94], which may reduce the need for compensations such as circumduction. Lastly, phase-based controllers, such as [87, 94, 122], can ensure that essential joint kinematics that provide toe-clearance are correctly timed for each step, further diminishing the need for circumduction.

1.5 Dissertation Outline

This dissertation outlines research dedicated to the design of actuation for a robotic prosthetic leg and the implications it has on amputee gait. Chapter 2 begins by describing the potential benefits of this new style of actuation design for powered prostheses, as well as specific details toward the design of the physical device. System-level benefits are then tested and validated through benchtop experimentation. Additional able-bodied and amputee walking experiments are then presented to show preliminary kinematic, energetic, and audible results of this actuation use during gait. Chapter 3 begins by describing the lack of evidence throughout literature for a powered prosthesis's ability to positively impact amputee hip compensations during gait. Low-impedance actuation is then proposed to be uniquely suited to reduce certain compensations by utilizing different control schemes. A unique walking controller is then described which exploits the variety of control schemes applicable to the low-impedance actuation scheme. Amputee walking experiments are then described and results are presented. Chapter 4 discusses relevant implications of low-impedance actuation on the field of robotic prosthetic legs. This chapter also outlines and discusses limitations and future work for the presented research. Chapter 5 points out major conclusions that can be taken from the research presented in this dissertation. Appendix A presents a Bill of Materials, which outlines components, materials, mass, and other part specific information.

Appendix B provides an overview of the LabVIEW code constructed to run the prosthesis in real-time. Since this prosthetic leg operates as a platform for the rapid prototyping of controllers, Appendix C outlines the process to convert controllers written MATLAB into a LabVIEW executable form. Lastly, to further reduce the "barriers to entry" for control prototyping, specific link segment characteristics are presented in Appendix D.

CHAPTER 2

DESIGN AND VALIDATION OF A POWERED KNEE-ANKLE PROSTHESIS WITH HIGH-TORQUE, LOW-IMPEDANCE ACTUATORS[1]

Authors – Toby Elery, Siavash Rezazadeh, Christopher Nesler, and Robert D. Gregg

The Department of Mechanical Engineering, ECSW 3.1

The University of Texas at Dallas

800 West Campbell Road

Richardson, Texas 75080-3021

Corresponding author: Toby Elery

2.1 Author Contributions

T. Elery and R. Gregg devised the project and main conceptual ideas. T. Elery and C. Nesler conducted most of the technical and engineering tasks toward the hardware used in this chapter. T. Elery and S. Rezazadeh conceived, planned, and conducted experiments. T. Elery collected experimental data and conducted data analysis. All authors contributed to the interpretation of the results and discussion. T. Elery wrote the first draft of the manuscript with support from S. Rezazadeh. All authors provided critical feedback and helped shape the final manuscript. R. Gregg supervised the project.

2.2 Abstract

This chapter presents the design of a powered knee-ankle prosthetic leg, which implements high-torque actuators with low-reduction transmissions. The transmission coupled with a high-torque and low-speed motor creates an actuator with low mechanical impedance and high backdrivability. This style of actuation presents several possible benefits over modern actuation styles in emerging robotic prosthetic legs, which include free-swinging knee motion, compliance with the ground, negligible unmodeled actuator dynamics, less acoustic noise, and power regeneration. Benchtop tests establish that both joints can be backdriven by small torques (~1-3 Nm) and confirm the small reflected inertia. Impedance control tests prove that the intrinsic impedance and unmodeled dynamics of the actuator are sufficiently small to control joint impedance without torque feedback or lengthy tuning trials. Walking experiments validate performance under the designed loading conditions with minimal tuning. Lastly, the regenerative abilities, low friction, and small reflected inertia of the presented actuators reduced power consumption and acoustic noise compared to state-of-art powered legs.

2.3 Introduction

Use of conventional passive prostheses after lower-limb loss results in gait that is slower, less stable, and less energy efficient than able-bodied locomotion [73, 32]. Passive prostheses aim to alleviate the effects of amputation using mechanisms such as springs, cams, and dampers to mimic normative gait patterns. However, passive prostheses are limited in functionality due to the fact that such mechanisms can only dissipate energy that the user introduces. Although these passive devices restore some functionality, amputees are typically left with an asymmetric gait [49]. Moreover, most devices are designed for level-ground walking conditions and do not adequately facilitate tasks such as sit-to-stand or stair ascent/descent. Semi-active prostheses, such as the Ottobock C-Leg, utilize microprocessors to control the damping of joints via small actuators that manipulate hydraulic valves during the user's gait [55, 9]. This approach allows for a single product to be easily adaptable to a variety of subjects, environments, and tasks, but semi-active devices can still only dissipate energy from the user's gait. Powered prostheses can actively inject energy and therefore have greater capability to restore mobility and quality of life to those who live with the loss of a limb.

In the last decade, a great amount of research has gone into the design and control of powered prosthetic limbs, resulting in several prosthetic devices that implement a variety of actuation schemes [82, 120, 127, 57]. Rigid, or non-backdrivable actuators, that implement transmissions such as worm gears [66] or cam-follower/leadscrews [64], have recently been implemented in order to reduce the size and weight of the prosthesis. Several other prosthetic legs implement actuators with low-backdrivability, or high-impedance. Such actuators commonly include high-speed, low-torque motors with high-ratio transmissions, such as ball screws or multiple/belt gear stages [82, 30, 131, 87, 55, 83, 59, 5, 114, 38, 63, 12, 48, 68, 119]. This high-impedance actuation scheme, which typically consists of reduction ratios greater than 100:1, results in more rigid joints and large reflected inertias. This can cause more painful impact forces on the residual limb after extended use. This also forces the knee

swing to be actively controlled rather than naturally free-swinging (like, for example, the C-Leg), which results in higher energy consumption and reduced battery life. Additionally, more meshing or rolling parts in the transmission result in more acoustic noise that is bothersome to patients. A recently developed prosthetic leg implements a transmission with a reduced reduction ratio of ~50:1 [7], but the resulting actuator impedance is still high enough to share some of the limitations discussed above.

In the past few years, legged robots such as the quadruped MIT Cheetah [103], biped Cassie [4], and others [50, 90, 69, 135, 124] have embraced high-torque motors with low-ratio or no transmissions. High-torque, low-reduction-ratio actuators (also referred to as low-impedance actuators) offer several benefits for legged robotics that are also desirable in powered prostheses. The lower mechanical impedance (inertias and frictional losses) of these actuators minimizes the effect of unmodeled dynamics, which in turn simplifies an otherwise complex control problem, increases robustness, and makes the system behave closer to an ideal model. Force control in these actuators can be comparable to series elastic actuators without their design and manufacturing complexities and low bandwidth [5, 79]. Low-impedance actuators are also compliant, which aids in regenerating energy and mitigating impact forces [126].

We propose that low-impedance actuators also have benefits specific to powered prostheses, including passive knee-swing motion, energy sharing between joints, acoustic sound reduction, and compliance with the ground through impedance control. A free-swinging knee joint allows for a more natural gait, while reducing the power requirements of the actuator during the swing phase. Energy sharing phases of gait such as mid-stance, where the ankle regenerates energy while the knee demands it, can lead to longer periods of untethered operation, which is critical for robotic legs in consumer applications. The low mechanical impedance from reduced friction and gear meshings can lead to a quieter device, which is crucial for the clinical acceptance of powered prosthetic legs. Lastly, the implementation of

biological joint impedances can promote natural compliance with the ground and provide smoother touchdown impacts, which can in turn improve efficiency of the system and comfort for the user. Although there have been attempts to control prosthesis joints using open-loop torque control [114], the non-negligible dynamics of the actuator would considerably affect the joint torque and thus requiring lengthy sessions of tuning impedance parameters [111].

In the process of designing low-impedance actuators, transmission design is a critical problem. Single-stage planetary transmissions are extremely efficient and have less intrinsic impedance than multi-stage transmissions, but are typically limited to ratios below 10:1. Therefore, efficient single-stage transmissions usually require a customized motor design, such as [103], to achieve the high output torques required during legged locomotion. Other transmission choices used in robotic legs such as harmonic and cycloid gear drives exhibit other problems such as efficiency and manufacturing complexities, respectively [102]. To overcome these shortcomings, we propose using a single-stage stepped-planet compound planetary gear transmission (SPC-PGT) [67] coupled with a high torque-density motor. As we will show, the resulting actuator has low mechanical impedance and high backdrivability. Although this style of transmission has the same number of gears meshing as a single-stage planetary transmission, it offers a higher range of reduction ratios while maintaining high efficiency and low acoustic sound. The manufacturability of this transmission style is also simplified compared to previously mentioned styles.

This chapter presents the benchtop validation of the powered transfemoral prosthetic leg described in [24] through the implementation of a walking controller that utilizes the compliant nature of the leg's actuators to facilitate smooth and easy switching between impedance and position control paradigms at different walking speeds. Moreover, the low impedance of the actuators allows for the direct use of estimated human joint impedance. This can simplify the implementation and tuning of the biomimetic walking controller compared to typical open-loop (no joint torque feedback) impedance control of actuators with

non-negligible intrinsic impedance. Examining the leg during walking allows for the quantification of specific properties not measurable during benchtop testing, such as kinematics and kinetics, electrical power, and acoustic sound levels during normative loading conditions. We validate the actuator design in walking experiments with an able-bodied subject, demonstrating normative kinematics and push-off power with reduced acoustic noise compared to previous designs. These tests also demonstrate that accurate impedance and torque control can be achieved without torque sensors. These sensors are removed in a revised assembly to minimize weight and volume for experiments with a transfemoral amputee subject. In these trials, the joint compliance facilitates energy regeneration and sharing between joints during periods of negative work, such as knee swing extension. This is useful to increase the efficiency of powered prostheses, which leads to extended battery life and usage time [57].

The mechatronic design of the powered prosthetic leg is presented in Section 2.4, including the motor, transmission, electrical system, and structure of both joints. Section 2.5 introduces the leg's control method implemented in Section 2.6. Section 2.6.1 presents a series of benchtop experiments that characterize the velocity, torque, position tracking, and backdrive capabilities of the actuators. Section 2.6.2 presents the setup and results of walking experiments, including power regeneration and acoustic sound reduction during walking at different speeds. Section 2.7 discusses the results and Section 2.8 concludes the chapter.

2.4 Hardware Design

2.4.1 Design Overview

The main objective of this prosthesis design is to achieve human-like joint impedance and dynamics, such that biological joint impedance values can be directly implemented into joint level control. To achieve this, the design must have negligible intrinsic joint inertia similar to human joints [128]. Therefore, our main design goal is to minimize the reflected inertia

of the joint's actuator while preserving the required torque capabilities. For reference, we aim for a substantially reduced actuator inertia compared to that of the state-of-art powered prosthesis (3rd Generation Vanderbilt Leg - knee actuator; 0.1032 kg·m^2) [59]. Additionally, each actuator must be able to meet the necessary torque, velocity, position, and power requirements for level ground, stair ascent, and stair descent ambulation [128, 26], shown in Table 2.1. Fig. 2.1 presents the required joint power and torque throughout the gait cycle for these tasks. We wish to exceed the peak torque and power capabilities of state-of-art prosthetic legs to fully match biological levels for heavier subjects and more demanding tasks, such as fast walking and stair ascent, which require ~130 Nm and ~350 W for a 75 kg individual. Note that the Vanderbilt leg is still capable of navigating stairs with a peak power of 200 W [62, 58]. Lastly, a self-imposed requirement of an adjustable shank length allows for a larger population of potential users.

Structural components of both actuators were optimized using the finite element analysis software, ANSYS, to ensure structural integrity for loading conditions of a 113.4 kg (250 lbs) user and against impacts (~3 times the subject weight) during level ground walking and stair ambulation. Most machined components were made of 7075-T6 aluminum, with a few shafts, gears, and bearings made of stainless steel. The leg was assembled in two iterations (Fig. 2.2): a preliminary one with torque sensors to validate the actuator capabilities during benchtop and able-bodied experiments, and a final one without torque sensors to reduce size and mass for amputee testing. The first assembly (Fig. 2.2, left) weighs approximately 6.05 kg without batteries or 6.61 kg with batteries. A weight breakdown is shown in Table 2.2 under "Preliminary Mass". The leg's Lithium-Polymer batteries, TP1600-4SA80X (Thunder Power, Nevada, USA), were kept off-board for benchtop and able-bodied experiments to ensure safety due to the potential for high regenerative currents. Note that for the second assembly, batteries were mounted onboard with active voltage monitoring of each individual cell. The knee actuator is ~13.7 cm wide (medial-lateral) by 12.9 cm deep (anterior-posterior).

The ankle joint is ~6.5 cm wide by 7.6 cm deep. The section corresponding to the calf is ~11.8 cm wide by ~12.9 cm deep, which equates to approximately the 30th and 50th percentile of adult male and female calf circumference, respectively [71]. Furthermore, the distance from the top of the prosthesis to the knee center is ~7.8 cm, the minimum distance between the knee and ankle center is ~32.9 cm, and the distance from the ankle center and the ground is ~8.5 cm (including the cosmetic foot shell). Lastly, in an effort to reduce weight, components that are under minimal loading conditions were 3D printed in ABS plastic.

2.4.2 Revisions for Amputee Testing

The prosthesis required torque sensors in the testing and validation of its actuators during benchtop and able-bodied walking experiments. However, the results in Sections 2.6.1 and 2.6.2 demonstrated the precise open-loop torque control capabilities of the actuators, thus rendering the torque sensors unnecessary for further experimentation. Therefore, prior to amputee experiments, revisions were made to the structure of the prosthesis to remove both the knee and ankle torque sensors, shown on the right in Fig. 2.2. This is important because it led to a reduction in mass and volume of the leg, both of which are important when translating to the clinical setting. The removal of these sensors reduced the medial-lateral width of each actuator by ~1 cm. In addition to the removal of the torque sensors, smaller batteries (TP870-3SR70, Thunder Power) were selected to be mounted on the leg, which enabled untethered operation of the prosthesis. The mass of the entire prosthesis was reduced by ~0.52 kg, bringing the mass to 6.09 kg, including batteries. A breakdown of the revised mass is given in Table 2.2.

2.4.3 Motor and Driver

High-torque motors typically used in industrial settings have large masses and volumes due to their robust housings and heat sinks. These motors are typically fixed in place, leading

Table 2.1: Combined knee and ankle requirements

	Ankle Requirements	Knee Requirements
Peak Torque	~130 Nm	~120 Nm
Velocity	360°/s	330°/s
Position	−28° to 20°	0° to 105°
Peak Power	345 W	220 W

Table 2.2: Approximate mass of leg components

	Preliminary Mass (kg)	Revised Mass (kg)
Motors	1.18	1.18
Transmissions	1.39	1.32
Torque Sensors	0.38	-
Load Cell	0.19	0.19
Structure	2.29	2.17
CF Foot	0.30	0.30
Electronics	0.29	0.45
Wiring	0.03	0.05
Li-Po Batteries	0.56	0.43
Total	6.61	6.09

to minimal consideration of weight in their design. However, for implementation into a powered prosthetic leg, it was necessary for us to select a motor with high torque density, to ensure that our actuator could produce the required torque while remaining as light and compact as possible. To this end, we selected the ILM 85x26 motor kit, Robodrive, Germany. This frameless, brushless DC motor kit allowed for the design of a custom housing that can withstand loading conditions and dissipate heat, while reducing the weight compared to industrial motor assemblies. This motor has a manufacturer-rated torque of 2.6 Nm, peak torque of 8.3 Nm, and a maximum velocity of 1500 rpm. It is rated at 410 W, 11 A, and 48 V. A 25/100 Solo Gold Twitter motor driver (Elmo Motion Control, Petah Tikva, Israel) is

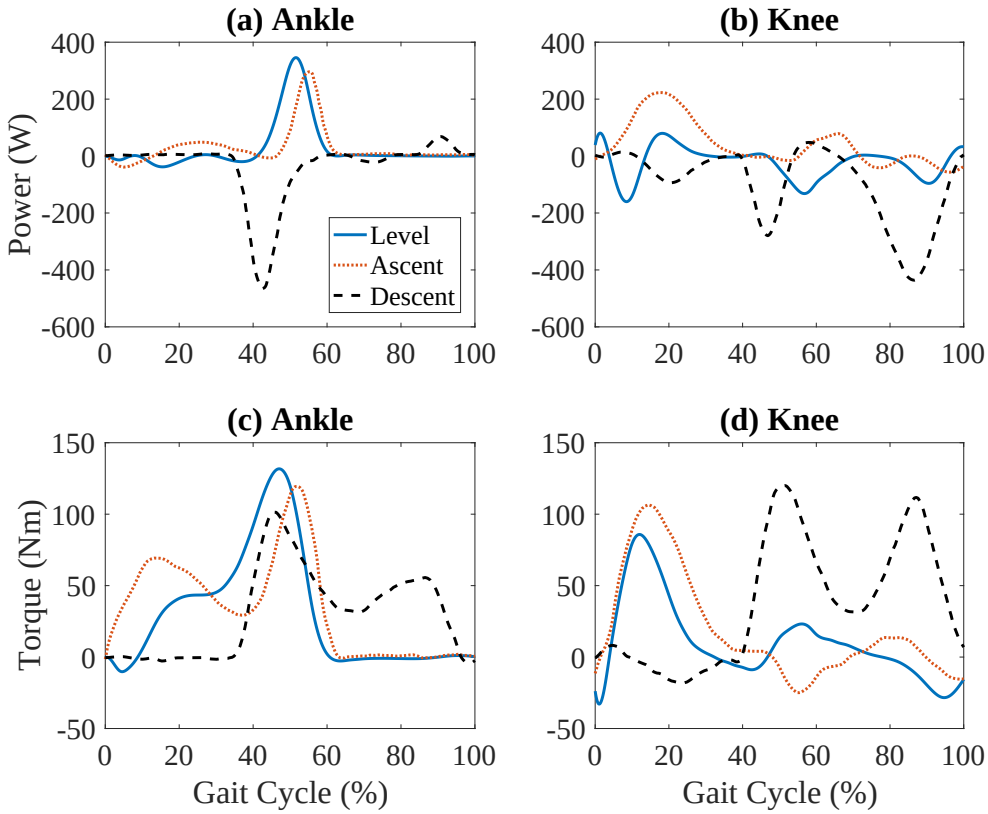

Figure 2.1: Ankle (a & c) and knee (b & d) average joint powers and torques for healthy individuals (75 kg) [128], used for defining peak requirements of the powered prosthesis. Solid blue lines indicate level ground walking at fast speeds, where dotted red lines and dashed black lines represent stair ascent and descent, respectively.

used, which has a rated current of 17.6 A and a peak current of 35.2 A. The small size and mass of the driver (22.2 g) make it ideal for minimizing overall actuator size and mass.

2.4.4 Transmission

It was necessary to realize a transmission which would increase torque and decrease speed of the selected motor to fit within the desired torque/velocity range, while minimizing the reduction ratio, and therefore the reflected inertia. We determined that a reduction ratio of between 20:1 and 25:1 would be needed to achieve maximum torques, while maintaining desired speeds. Therefore, we designed a custom single-stage stepped-planet compound

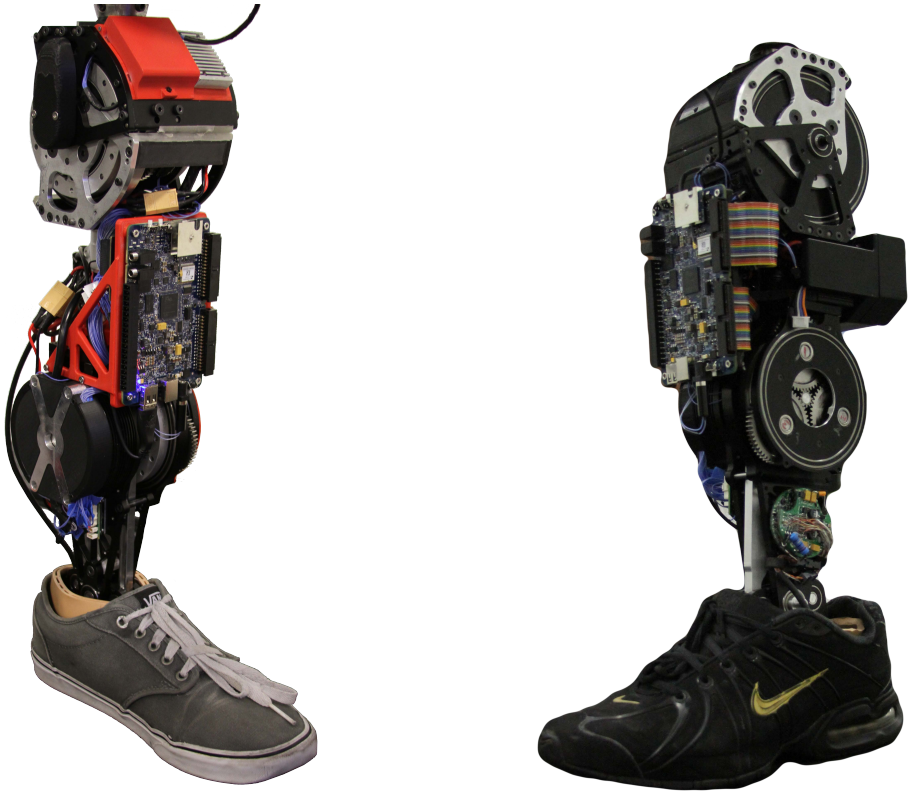

Figure 2.2: Final assemblies of the prosthetic leg. The image on the left displays the first version of the prosthesis (without batteries), which was used in benchtop and able-bodied testing. The image on the right displays the prosthesis after revisions were made for amputee experiments (i.e., torque sensor removal and onboard batteries).

planetary gear transmission (SPC-PGT) with a 22:1 reduction. Considering the peak torque of the actuators (~183 Nm), the Lewis Factor Equation for gear tooth stress was used in the initial selection of off-the-shelf gears (SDP/SI, New York, USA), which were then revised using FEA analysis to optimize for weight. The SPC-PGT consists of one sun gear, one ring gear, and six planet gears. Traditional planetary gear transmissions have only three planet gears, which mesh between the sun and ring gears. However, the SPC-PGT used here calls for three sun-planet gears and three ring-planet gears. Each sun-planet gear is coaxially fixed in relation to its corresponding ring-planet gear through a keyed shaft. The sun-planet gears mesh with the sun gear, radially located 120° apart from each other. Similarly, the ring-planet gears are meshed with the ring gear, and are also radially located 120° apart

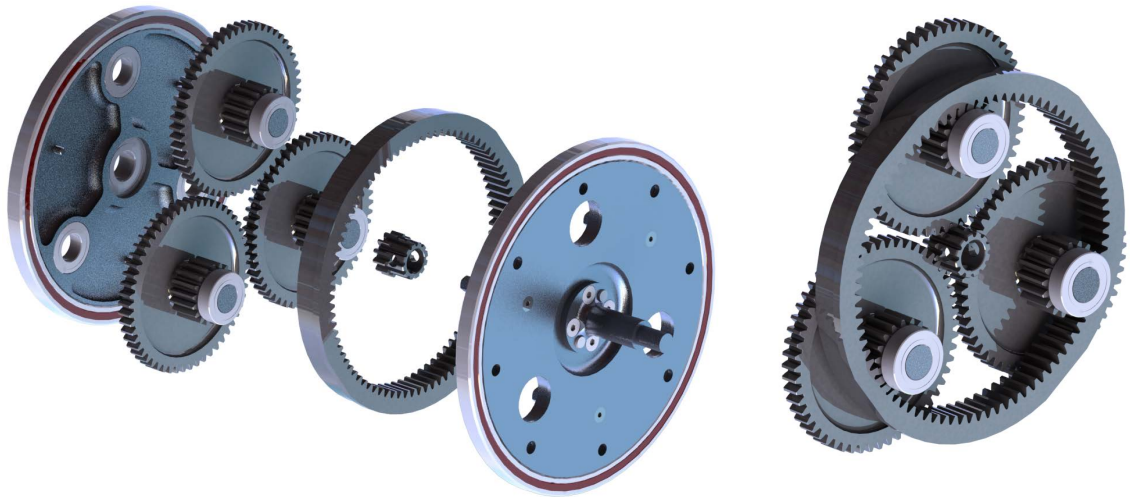

Figure 2.3: CAD model of the planetary gear transmission. The image on the left illustrates an exploded view of the entire transmission (including planet carriers), while the right demonstrates the gear layout after assembly.

from each other. The shafts of the planet gears are held on either side by what is commonly referred to as a planet carrier. The transmission assembly can be seen in Fig. 2.3.

Although planetary gear transmissions have multiple input-to-output configurations, the presented gearbox uses the sun gear as the input and the planetary carrier as the output to achieve the maximum ratio possible given a specific gear set. A traditional single-stage planetary gear transmission with the same input to output configuration has a reduction ratio found by $\tau_m/\tau_j = (D_r + D_s)/(D_s)$, whereas the reduction ratio of the single-stage SPC-PGT is found by $\tau_m/\tau_j = 1 + (D_r D_{\mathrm{sp}})/(D_s D_{\mathrm{rp}})$, where τ_m and τ_j are the motor and joint torque, respectively, and D_s, D_{sp}, D_{rp}, and D_r are the sun, sun-planet, ring-planet, and ring gear diameter, respectively. Due to geometric constraints of a traditional planetary gear transmission, reduction ratios are typically limited to 10:1. However, the SPC-PGT can easily achieve higher reduction ratios in approximately the same geometric volume. Although the presented design differs from a traditional single-stage planetary gear transmission, the number of gears meshed together is the exact same, thus increasing the obtainable reduction ratio without decreasing efficiency or increasing acoustic sound [34]. This also minimizes

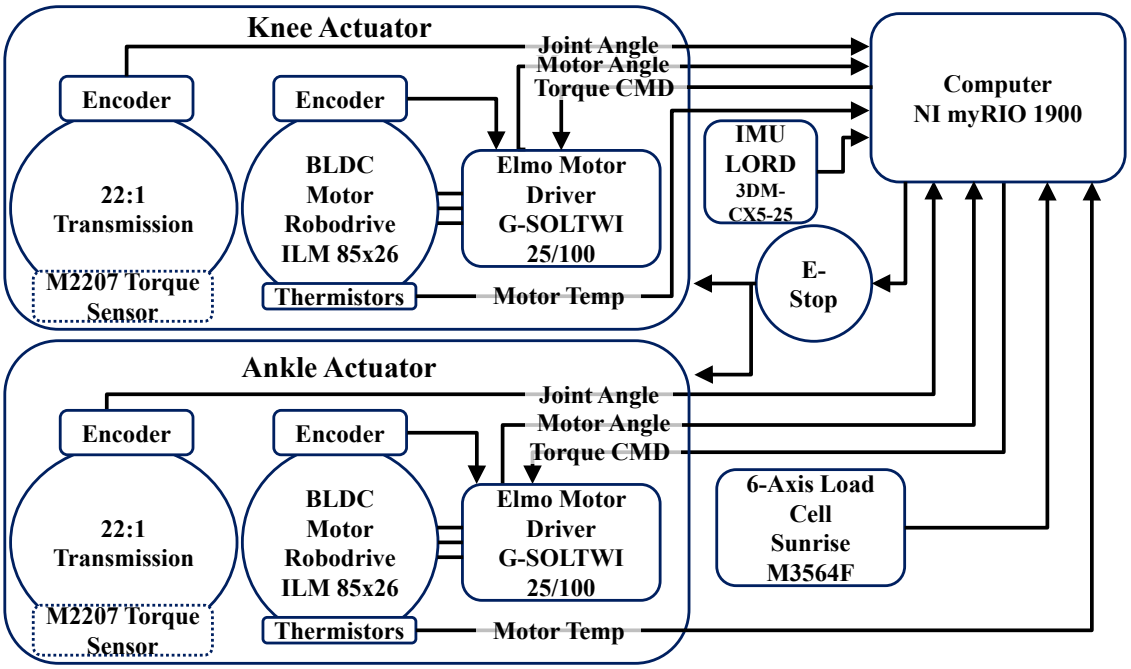

Figure 2.4: Block Diagram of Electrical System: The system's computer receives feedback related to the user's gait and sends torque commands to the motor drivers. Torque sensors are indicated in dashed boxes to represent their presence during benchtop and able-bodied testing but absence for amputee testing.

backlash, which measured less than 36 arcmin (0.6°) during walking. Values between 30 and 120 arcmin (0.5° and 2°) are seen in similar robotic applications [22, 102]. Coupled to the high-torque motor, this transmission provides a continuous torque of 57.2 Nm and a peak torque of 182.6 Nm, demonstrating a larger scale application of a SPC-PGT transmission compared to the jumping robot in [22].

Lastly, it is necessary to estimate the reflected inertia of the actuator with this choice of motor and transmission. We obtained this estimate by taking the inertias from the CAD model of everything rigidly fixed to the motor's rotor, such as the motor shaft and sun gear, and multiplying it by the square of the gear ratio. We then added the inertias of all components that rotate with the actuator's output, such as the planet gears and carriers, to arrive at an estimated reflected inertia of $I_j = 0.0625$ kg·m^2. This value will later be validated through benchtop experiments.

2.4.5 Sensors and Electrical System

Sensor feedback is critical for both the control and safety features of the device. The knee and ankle actuators have one optical quadrature encoder, E5 and EC35 (US Digital, Washington, USA), with 4096 and 5000 cycles per revolution, respectively. Fixed to the motor shaft, the encoder sends motor position data to the motor driver and system controller. Once at the controller, this data is multiplied by the transmission reduction ratio for position and velocity feedback. The leg's design allows for a second encoder at the actuator output, which was used to quantify transmission backlash and then removed. For this reason, some renderings show two encoders per actuator. Additionally, both motors contain two Pt1000 thermistors embedded in the stator. These monitor the internal temperature of the stator to ensure that the motor is not damaged during use. A M3564F 6-axis load cell, Sunrise Instruments, Nanning, China, is located below the ankle joint axis to detect ground contact and monitor ground reaction forces/moments. It is capable of reading 2500 N/200 Nm along the x and y axes and 5000 N/100 Nm along the z axis. In addition to the load cell, a single axis M2207 torque sensor, Sunrise Instruments, Nanning, China, is located at the output of the knee and ankle actuators in the preliminary assembly used to validate the actuator capabilities, but not in the final assembly used for amputee testing.

These sensors interface with the system's microcontroller, a myRIO (National Instruments, Texas, USA). The controllers presented in Section 2.6 and Section 2.5 are implemented in the National Instruments LabVIEW software environment and then imported onto the myRIO. Fig. 2.4 displays a systemic view of the described electrical system.

2.4.6 Knee Mechanical Structure

Although the physiological knee is a polycentric joint and many passive prostheses are modeled after this, powered prostheses are often modeled as a single axis joint due to the minimal benefit gained from such an increase in design complexity[113, 81]. Therefore, the presented

Figure 2.5: CAD design of the knee actuator. The exploded view on the left displays the components/sub-assemblies of the knee actuator, such as the upper/lower hinges, encoders, transmission, motor, and pylon. The image on the right presents the assembled knee actuator. The pyramid adapter on top connects to the user's socket, and the length-adjustable pylon on bottom connects to the ankle actuator module.

knee actuator shown in Fig. 2.5 is designed as a simple hinge, which includes an upper and lower hinge piece. The upper hinge attaches to the socket on the user's residual limb via a pyramid adapter. The lower hinge is rigidly attached to the gearbox output (e.g., torque sensor), thus acting as the actuator output. Components of the actuator, such as the motor and transmission, are attached to the upper hinge, instead of the lower hinge, to minimize cable movement during gait. This design keeps the motor, transmission, and knee joint coaxial, which avoids the need for additional material/components to transfer motion from the motor axis to the knee joint axis.

This actuator is designed to allow simple changes to adjustable components so that the prosthesis may be configured for different use cases (i.e., modified range of motion and shank length). This is accomplished through the use of swappable hard stops and modular actuators separated by a pylon. Knee motion is constrained by bumpers that are 3D printed

using a compliant material, TangoPlus (Stratasys, Minnesota, USA), to dampen the impact of the upper and lower hinges at maximum flexion and extension. Interchangeable bumpers of varying thickness allow the actuator to be configured with desired limits to knee flexion and extension. With no bumpers in place, the actuator's range of motion includes 112° flexion and −5° hyperextension.

Connected to the bottom of the lower hinge is an adjustable pylon system. This system consists of a universal prosthetic pylon held by two tube clamps. Each tube clamp uses a single bolt to apply pressure around the circumference of the pylon, thus holding it in place. Due to this design, the distance between the two joints can be continuously adjusted for subjects with heights ranging from 1.52m to 1.98m (5' to 6'6"), which can accommodate approximately 99.5 and 91.8 percent of all males and females, respectively [17]. The pylon can also be rotated by a prosthetist to properly align the abduction/adduction of the prosthetic leg's ankle actuator.

2.4.7 Ankle Mechanical Structure

Similar to the knee actuator, the ankle is designed with a single axis of rotation. Although the concept and capabilities of the two actuators are the same (i.e., torque and velocities), the physical layout of the ankle actuator, Fig. 2.6, is different from that of the knee. At the knee, the axis of rotation of the motor and the joint output are coaxial. At the ankle, the motor axis of rotation is moved proximal to the body for two main reasons: users apply greater hip torque and therefore expend more metabolic energy when wearing a mass that is more distal on the body [13], and overall actuator width would not allow the prosthetic foot to wear a cosmetic foot shell or shoe. With the motor and the transmission moved proximal to the body, a parallelogram 4-bar linkage mechanism was implemented to translate the torque from the output of the gearbox distal to the location of the anatomical ankle joint. Other powered prosthetic ankles have utilized linkage mechanisms to alter joint torque or align

Figure 2.6: CAD design of the ankle actuator. The image on the left presents the assembled ankle actuator. The exploded view on the right displays the components/sub-assemblies of the ankle actuator, such as the motor, structure, 4-bar linkage, transmission, electronics, and foot.

impact loads [16, 56]. The ankle joint is mechanically constrained by hard stops located at approximately $\pm 45°$. This provides ample rotation for a wide range of tasks, while preventing excessive ankle flexion. The 6-axis load cell is mounted directly below the ankle joint. An off-the-shelf Ottobock LoRider prosthetic foot is attached to the bottom of the 6-axis load cell. Finally, a cosmetic foot shell is installed onto the prosthetic foot, allowing the user to wear most styles of shoes.

2.5 Control Design

In this section, we present our approach for the control of the powered prosthesis. We show how the specific attributes of the designed actuator can be leveraged to facilitate the design of a dynamic walking controller.

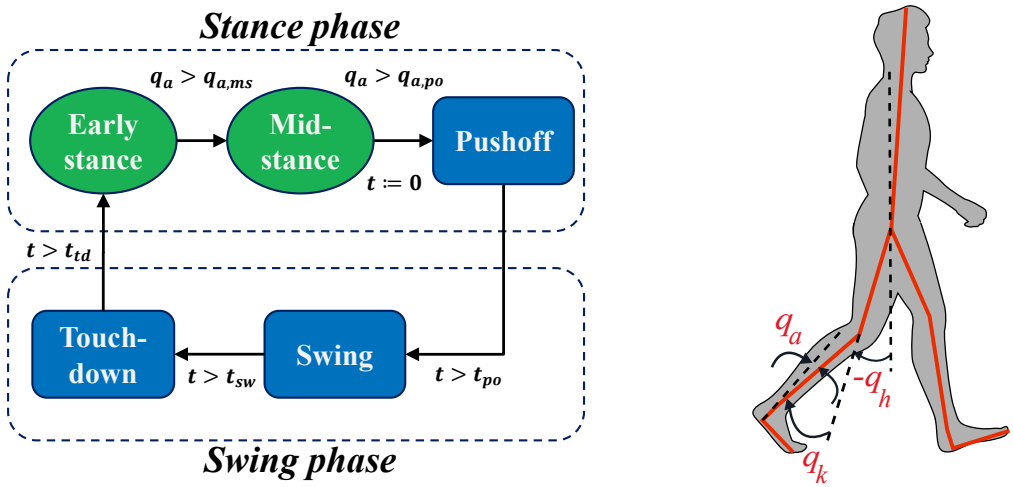

(a) (b)

Figure 2.7: (a) Finite state machine (FMS) for walking control. Blue rectangles and green ellipses indicate time-based (position control) and impedance-based states, respectively. (b) Definition of the joint angles.

2.5.1 Joint-Level Control

Due to its inherent simplicity and robustness, a PD controller is the most common choice for the joint position control of robotic systems:

$$\tau_m = \frac{1}{n}[K_p(\theta_d - \theta) + K_d(\dot{\theta}_d - \dot{\theta})], \tag{2.1}$$

where K_p and K_d are positive PD gains and θ_d and θ are the desired and actual positions, respectively. Since the PD gains determine the pole's frequencies of the closed-loop system, these gains are set as high as possible to minimize tracking error and phase lag. In applications such as prosthetic legs, controllers that rely on a kinematic phase variable generally utilize this approach [33, 87, 93].

An alternative approach which is commonly used in control of powered prostheses is impedance control [37]. Generally, in robotics systems, the most common way to produce accurate joint impedance control is by using joint torque feedback to produce the desired behavior. Note that for a fixed transmission ratio n, the general relationship between motor

torque τ_m and joint torque τ_j can be written as

$$\tau_j = n\tau_m + n^2 I_m \ddot{\theta} + n^2 b_m \dot{\theta} + f(\theta, \dot{\theta}, t), \tag{2.2}$$

where I_m and b_m are motor inertia and damping, respectively, θ is the joint angle, and f contains nonlinear and time-dependent losses such as Coulomb friction, stiction and hysteresis. Note that $\tau_m = k_t i_m$, where k_t is the motor's torque constant and i_m is its current, commanded from the motor driver. Torque feedback is typically necessary to decrease the effect of unmodeled dynamics (f) and common uncertainties of inertia and damping parameters in (2.2). However, an actuator designed with minimal unmodeled dynamics can be utilized to reliably simulate any desired dynamics (an arbitrary impedance, for instance) without requiring torque feedback. This is especially important in a control problem such as walking, where unexpected interactions with the environment (impacts) are always likely to occur.

The high noise and limited speed of closed-loop force control during walking strongly motivates low-impedance actuation to achieve more natural dynamics. With an ideal actuator, a PD controller can be considered an open-loop impedance controller, with proportional and derivative gains acting as stiffness and damping, respectively [37]. Based on this, we expect that changing the stiffness and damping coefficients in (2.1) will enable a wide range of dynamic behaviors through highly variable joint impedances. Furthermore, the controller effectively can work as a position control scheme by increasing the gains, without any other change in the control structure.

As shown in [19], the discrete-time implementation of a controller in the form of (2.1) can lead to instability when the system interacts with a passive environment (in particular, a human). This depends on the human's emulated stiffness, actuator inertia and damping, and sampling frequency. Furthermore, it limits the range of the impedance coefficients (PD gains) that the controller can emulate. Based on this, we will later select the controller gains considering the actuator parameters and the humans' applicable range of stiffness.

2.5.2 Walking Control

As discussed, the low-inertia design of the actuators facilitates smooth and easy switching between position and impedance control paradigms. Here, we show how this characteristic can be leveraged in a walking controller.

In [114], Sup et al. designed a walking controller for their powered knee-ankle prosthesis based on a Finite State Machine (FSM). For each state of the FSM, they used an impedance controller of the form

$$\tau_m = K_p(\theta_d - \theta) - K_d\dot{\theta} + K_2(\theta_d - \theta)^3, \tag{2.3}$$

where K_p, K_d, and K_2 are tunable constant values for each state. The form of the impedance controller (2.3) was chosen to fit human joint torque profiles. However, due to high impedance of the actuators, the final values of the tuned parameters were quite different from biological values. This implies that the total joint impedance is different from the commanded impedance due to the non-negligible actuator impedance. The small correlation between the tuned and reference values of these parameters often requires lengthy sessions of tuning for each set of parameters to achieve the desired performance, since they are not known beforehand and change from one subject to another [112].

The controller we use in this work is similar to the one presented in [59]. Fig. 2.7 depicts the FSM corresponding to our controller. As in [59], impedance controllers have been used for control of early and mid-stance. This was motivated by the fact that impedance control provides reliable and smooth interaction with the environment (i.e., the ground). Since there is no interaction with the environment during swing phase, a time-based position tracking controller was designed based on able-bodied reference trajectories [128]. In contrast with [114] wherein θ_d is constant for each subphase, we followed [59] by tracking a time-based trajectory, which provides a stronger push-off and a smoother transition to swing phase. Based on this, time t is set to zero when the transition to push-off takes place. The duration

of push-off, swing, and touchdown subphases are determined by the preset speed-dependent parameters t_{po}, t_{sw}, and t_{td}. At the start of each subphase, the change of parameters (K_p and K_d, and also θ_d for impedance-based subphases) is performed through the use of a third-order spline to avoid any discontinuity in the commanded torque.

The purpose of the touchdown subphase is to change the PD parameters for smooth transition to the impedance control of the early stance subphase. The idea is that as the knee extends, the controller "expects" the ground contact rather than sensing and then reacting to it. Thereby, the reaction to impact becomes a part of the natural (open-loop) dynamics of the system. This type of natural response is also observed in biological locomotion [46] and used in legged robot applications [97, 91, 92]. Based on this, gains are gradually changed throughout the touchdown subphase to match those of early stance. This smooth transition paradigm can be considered as an extension of the methods proposed in [23] and [109], in which transition to stance is detected without contact sensing. The main difference in these works is that the gains are held constant for each phase.

The default stiffness values (equivalent to K_p as discussed) for the impedance control subphases were picked from the quasi-stiffness of able-bodied subjects, as estimated in [107, 106]. A small damping coefficient (K_d) was added to obtain a smoother operation. The details of the walking experiments and the selected gains are presented in the next section.

2.6 Experiments and Results

To validate and characterize the leg, benchtop and walking experiments were conducted. Benchtop experimentation aimed to verify specific characteristics of the actuators, whereas the walking experiments aimed to verify the leg's ability to perform under its designed loading conditions. A supplemental video of the experiments described in this section is available for download.

2.6.1 Benchtop Experiments

This section presents several benchtop experiments that demonstrate the position and impedance control capabilities, backdrivability, and bandwidth of the prosthesis's actuators.

Backdrive Torque

These tests aim to quantify the backdrive torque of the actuators, i.e., the torque required at the output of an actuator to rotate the motor through its transmission. For the first experiment, the ankle actuator was rigidly fixed to the benchtop setup with motion still being allowed at the ankle joint. A force was then applied with one finger to the toe of the foot (Fig. 2.8(a)). The applied force gradually increased until the joint moved. A total of nine trials of this experiment were conducted, three each with the ankle initially positioned at $-20°$, $0°$, and $20°$. For the case of $0°$ and $20°$, a downward force was applied to result in plantar flexion. For the case of -20°, an upward force was applied to result in dorsiflexion.

Throughout this experiment, torque data was collected from the 6-axis load cell. Torque maxima for each trial were extracted from the collected data and averaged for each initial starting position. These maxima occurred directly before the applied torque overcame the backdrive torque within the system. The magnitudes of the mean peak torque values were 3.41 Nm, 3.23 Nm, and 3.22 Nm for the initial ankle positions of -20°, 0°, and 20°, respectively.

In another experiment, the knee actuator was fixed to the benchtop and its output disconnected. Starting at 0 Nm and with intervals of 0.1 Nm, the commanded torque was slowly increased until the the joint started to move, which occurred at ~1 Nm. This consists of Coulomb friction and the uncompensated portion of cogging torque (depending on the cogging compensation methods used in the driver). Additionally, the Coulomb friction of the knee actuator, without the motor stator (in order to eliminate the cogging torque), was measured with a torque wrench to be ~0.2 Nm. These results suggest that the remaining

(a)

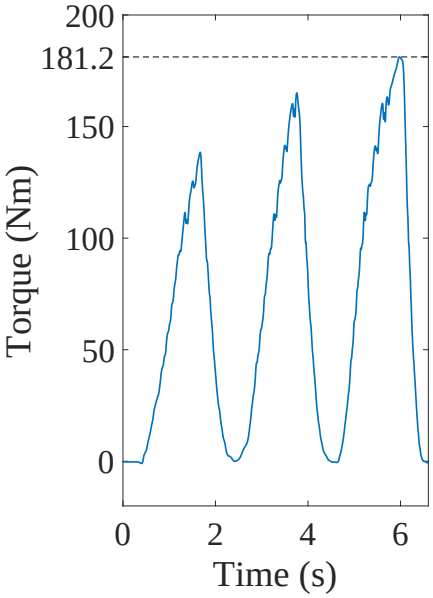

(b)

Figure 2.8: Benchtop torque tests. (a) shows the experimental setup for backdrive torque test. (b) Measured torque during peak torque tests.

backdrive torque can be attributed to the cogging torque of the motor. Therefore, we can conclude from these experiments that both actuators were able to be backdriven with low amounts of torque.

Peak Torque

To further verify the actuator capabilities, a simple test was conducted to quantify its peak torque. For this test, the knee and foot were separated from the ankle actuator. The ankle actuator was then fixed to the benchtop through the 6-axis load cell, which measures the output of the ankle actuator. During this experiment, the position controller of the ankle actuator, presented in Section 2.5.1, was set to regulate a fixed angle (zero). An oscillatory load was dynamically applied by hand to the shank. Note that this is similar to how the prosthesis will interact with the ground during impedance-based states of the walking controller, see Section 2.5.2. The pylon that typically connects the two actuators was replaced with an extended pylon to increase the lever arm and achieve larger torques. Force

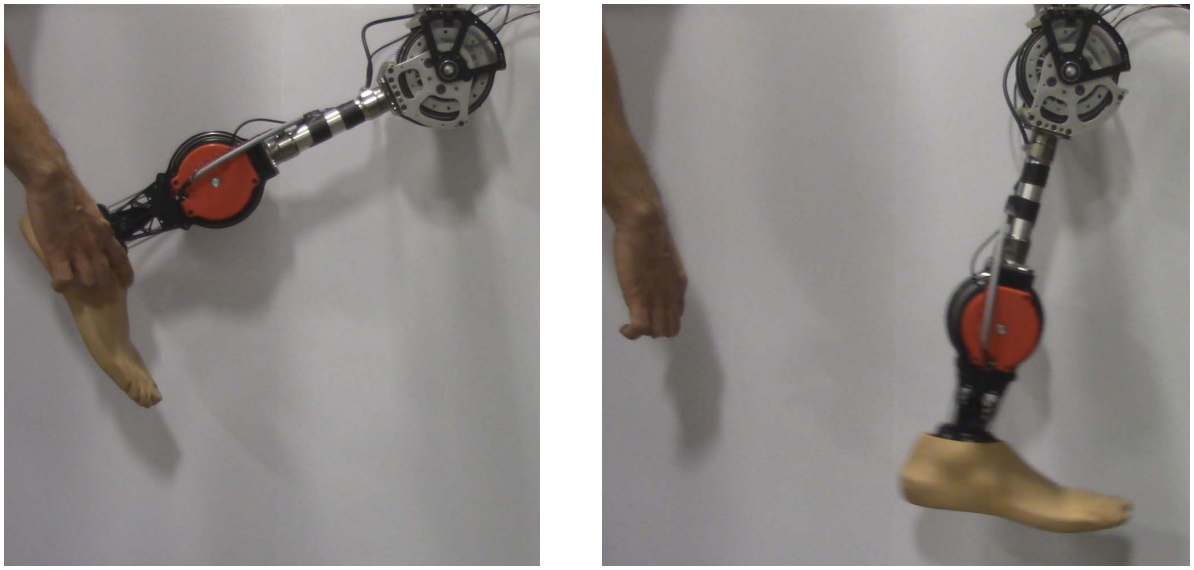

(a) (b)

Figure 2.9: Experimental setup for free swing test. (a) shows the unpowered leg when the knee is held in flexion. (b) shows the shank of the leg in motion after being released.

was applied by hand to the pylon for three consecutive cycles, with an increased magnitude for each cycle, see Fig. 2.8(b). The last force applied resulted in a peak measured torque of 181.2 Nm, which is ~1 Nm less than the peak rated torque of the actuator.

Free Swing

A free-swinging knee has the benefit of simplifying control effort during swing phase, therefore leading to more natural, energy-efficient operation. Toward this end, we performed a simple experiment to show that the knee could be backdriven by the weight of the shank and foot alone, thus simulating the swing phase of gait. With the motors unpowered, four trials were performed in which the top of the knee was fixed to the benchtop setup, flexed between 65°and 70°, and then released without a push. This experimental setup can be seen in Fig. 2.9. Fig. 2.10 shows the knee position for each of the four trials from the point of release until it reached the mechanical hard stop. With knee flexion peaking at approximately 70° for level walking, it can be seen in Fig. 2.10 that the knee exhibits free swing capabilities,

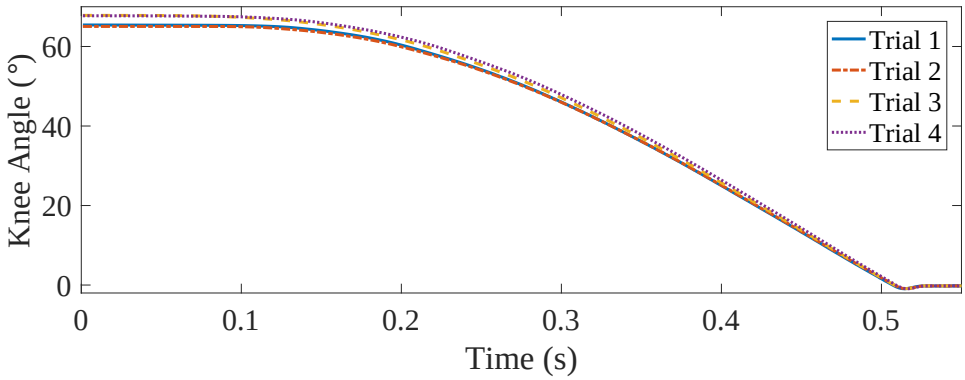

Figure 2.10: Recorded position of the knee as it returns to zero following release from an initial offset.

since the knee repeatedly returns to zero after being released from heights common during walking.

Parameter Identification

To identify the inertia and damping of the actuator, open-loop frequency response tests were performed with the knee actuator fixed to the benchtop and disconnected from its output/load. Sinusoidal torque commands were directly sent to the motor driver and the actuator's velocity was recorded. The sinusoidal signal began at a very low frequency, and was incrementally increased to higher frequencies until the test had to be halted due to excessive shaking and vibrations, i.e., 0.1 to 35 Hz. The resulting magnitudes presented in Fig. 2.11 show a DC offset of 7.6 dB and a cut-off frequency of 6 rad/sec at 4.6 dB (or -3 dB from DC offset). Assuming first-order dynamics of the form

$$G(s) = \frac{1}{Is + b}, \tag{2.4}$$

the inertia, I, and damping, b, were identified as 0.0696 kg·m^2 and 0.4169 N·m·s/rad, respectively. The frequency response of the system (2.4) with these values has been plotted over the experimental results in Fig. 2.11. The strong agreement between the two responses verifies that (2.4) closely explains the dynamics of the system.

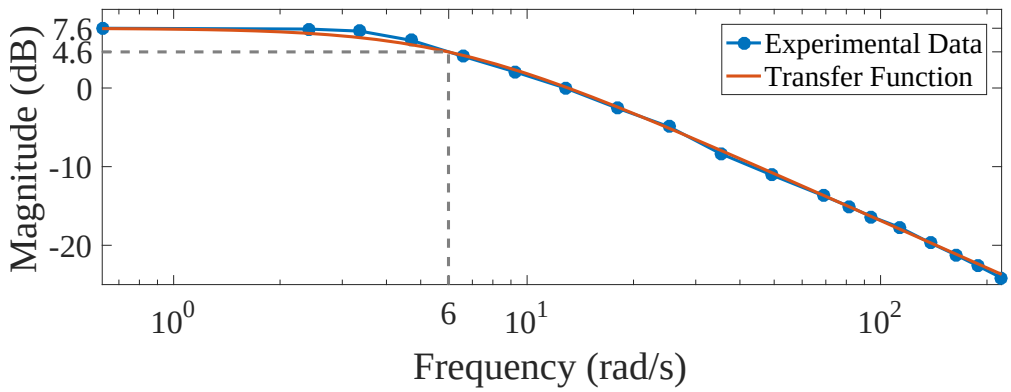

Figure 2.11: Magnitude plot for open-loop frequency response tests. This displays the DC offset and and cutoff frequency used to determine actuator impedance and damping.

Range of Stable Controller Gains for Interaction with a Compliant Environment

Following [19] with the identified actuator parameters, the discrete-time stability margin for the controller can be obtained from the points at which the roots of the characteristic equation $1 + C(z)L^*(s)$ satisfy $|z| = 1$. Here, $C(z)$ is the discretized PD controller of (2.1), and $L^*(s)$ is the sampled-time version of $L(s)$, the transfer function of the actuator dynamics (2.4) interacting with the human's impedance $H(s)$:

$$L(s) = \frac{1 - e^{-Ts}}{s^2} \frac{1}{Is + b + H(s)}, \tag{2.5}$$

where T is the sampling time.

Although stability can be investigated for any passive $H(s)$ in (2.5), it will result in unnecessarily conservative limitations on the gains. As discussed in [19], considering the human impedance as a limited-stiffness spring provides a more realistic set of conditions for the interaction stability. Since the stiffnesses that human leg joints emulate are typically less than 3000 Nm/rad [27, 53], we performed the stability analysis with three different stiffness values: 100 Nm/rad, 1000 Nm/rad, and 10,000 Nm/rad to cover a range of compliant to rigid interactions. The stability margins are depicted in Fig. 2.12. The PD gains will be selected with regard to the obtained stable region.

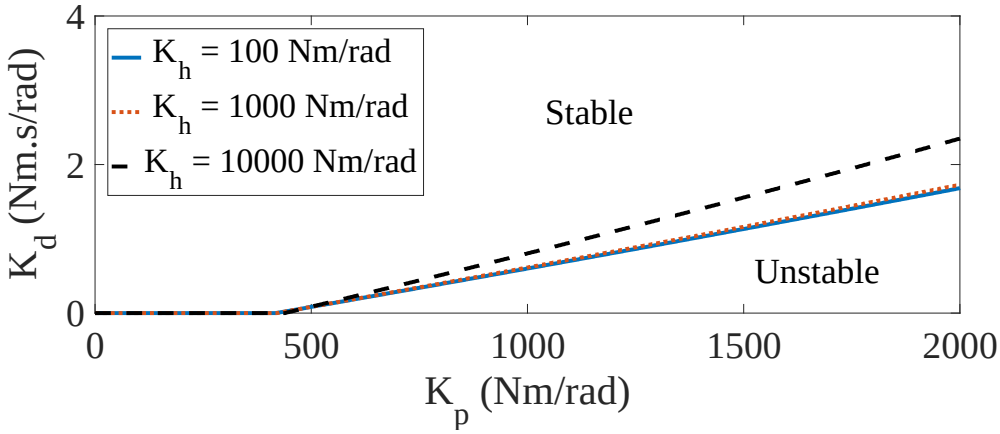

Figure 2.12: Stability margins for three different human stiffness values, K_h = 100, 1000, and 10,000 Nm/rad. The region above the margins is the stable region.

Note that the stable region obtained in Fig. 2.12 is still a conservative estimation. This is due to the fact that we did not consider the link inertias in our analysis to avoid nonlinearities, and as discussed in [19], the stable region grows with the increase in inertias. Moreover, we neglected interaction with the ground because the effective joint stiffness of prosthetic feet is much smaller than 10,000 Nm/rad [1], and thus it does not affect our analysis.

Closed-Loop Position Bandwidth

Real-world physical systems generally act as low-pass filters, attenuating high frequency inputs. In the case of actuators, especially electric ones, the cut-off frequency of the system becomes an important factor in characterizing the speed by which the output can be actively controlled through changing the input signal. Since closed-loop position controllers are implemented in some powered prostheses [87, 65, 70], closed-loop position control bandwidth tests were conducted to characterize the maximum frequency that the presented low-impedance actuators can achieve.

With the knee actuator fixed to the benchtop, the experiment began at a very low frequency, which was incrementally increased to higher frequencies until the test had to be halted due to excessive shaking and vibrations. The experiment was conducted with an

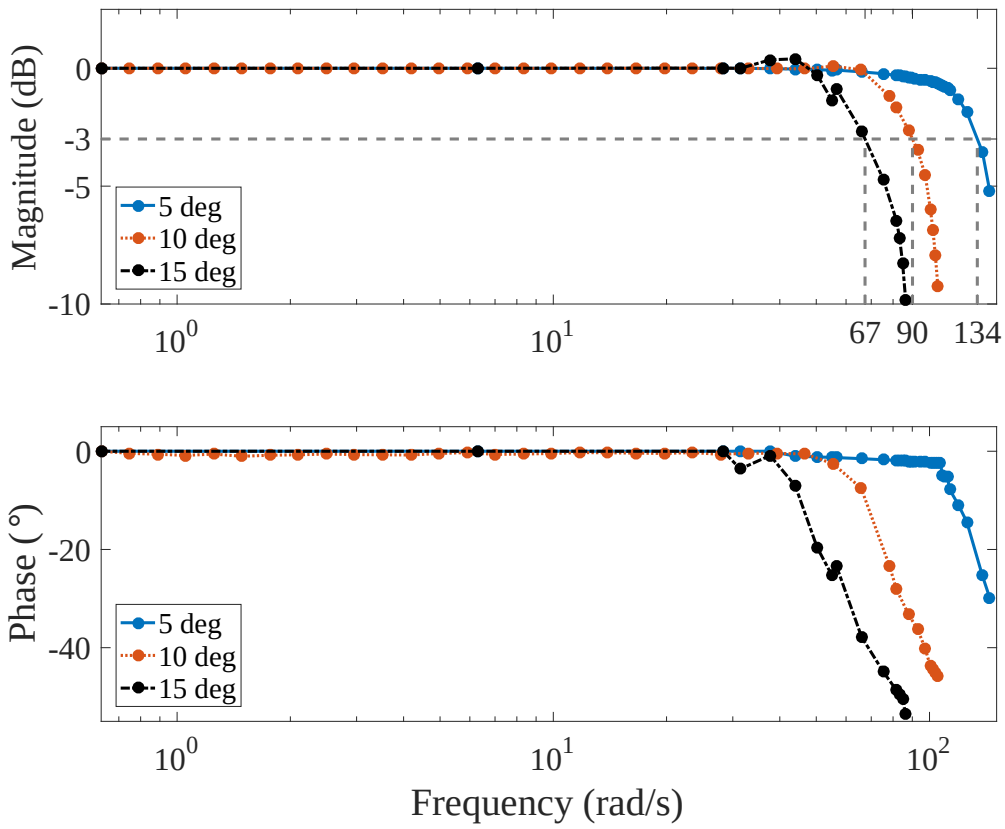

Figure 2.13: Bode plots for closed-loop position bandwidth tests. Inputs with amplitudes of 5, 10, and 15 degrees produce cutoff frequencies of approximately 134.0, 90.1, and 67.4 rad/s, or 21.3, 14.3, and 10.7 Hz, respectively.

input sine wave with three separate amplitudes: 5°, 10°, and 15°. The results, shown in Fig. 2.13, indicate respective cut-off frequencies of 134.0, 90.1, and 67.4 rad/s. Noting that a frequency analysis of human gait shows that the highest frequency content of walking is in the range of ~6-22 rad/s [98, 128], the actuator is expected to be completely capable of tracking the human-like joint trajectories.

Closed-Loop Position Control

To examine the actuators' position-tracking capabilities, a proportional-derivative (PD) controller with a gravity compensation term was implemented for each actuator. For this experiment, both joints were assembled together and the complete leg was mounted onto the

benchtop setup, as in Fig. 2.9. The normative joint trajectories from [128] were tracked at frequencies of 0.5 (slow walking), 1.0 (fast walking), and 1.3 Hz (running)

Fig. 2.14 displays tracking performance per joint for the increasing frequencies. For all three frequencies, the ankle actuator was able to track the position with little error (max 0.27°, 0.45°, and 0.55° for 0.5, 1.0, and 1.3 Hz, respectively). Although the knee tracking errors were relatively small for 0.5 and 1 Hz (max 1.04° and 6.42°, respectively), at 1.3 Hz the difference between desired and actual trajectories starts to become visible (max 13.17°). This error was mainly due to phase lag between desired and measured trajectories. Neglecting this phase lag reduces the maximum knee tracking error to 2.05° and 4.56° for 1.0 and 1.3 Hz, respectively. The higher error in the knee angle was due to both larger mass and inertia acting against the knee actuator, as well as the larger range of motion and higher acceleration compared to the ankle. Note that joint torque was limited to ±120 Nm for safety during these benchtop tests. This limitation will be relaxed for walking experiments, which will also have an aiding hip moment to swing the knee.

Open-Loop Impedance Control

In the previous sets of experiments, we showed that the design of the actuator and its high bandwidth make it capable of supporting walking control paradigms based on precise joint position tracking. Here we show that the actuator design also works well for compliant walking control paradigms (as discussed in Section 2.5). This specifically becomes important when one considers the most difficult portions of human trajectories to be mimicked by position control, namely the quick flexion and extension of the knee immediately after impact (Fig. 2.14(f)). In humans this happens due to natural compliance of the knee joint, rather than precisely following a prescribed position trajectory [113, 107]. This motivates us to test the ability of the designed actuator to demonstrate specific impedance behaviors.

As discussed in Section 2.5.1, we simply set the position control PD gains, K_p and K_d, equal to the desired spring and damper coefficients with units of Nm/rad and Nm·s/rad,

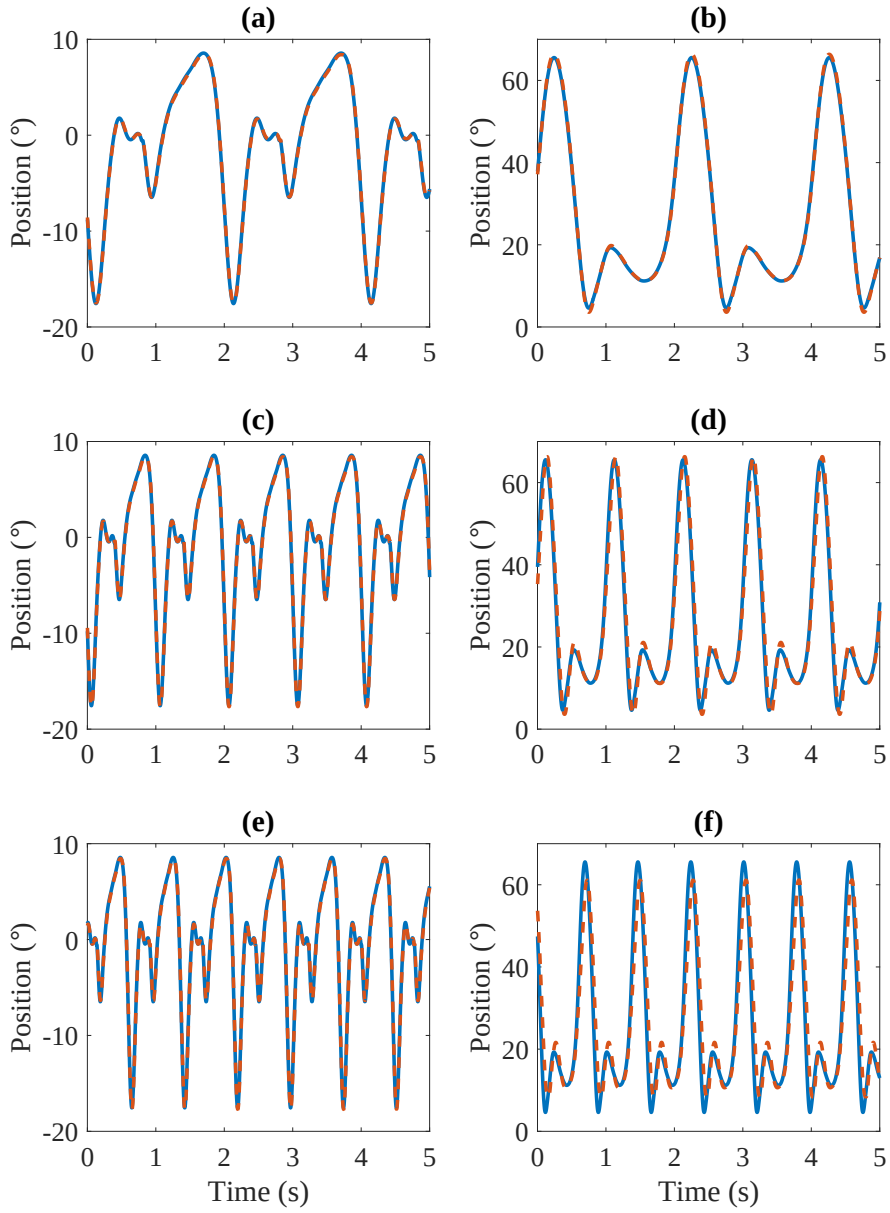

Figure 2.14: Position tracking of normative gait trajectories at various frequencies. Solid blue and dotted red lines denote the desired and measured position, respectively. Plots a), c), and e) present ankle tracking at 0.5, 1.0, and 1.3 Hz, respectively. Plots b), d), and f) present knee tracking at 0.5, 1.0, and 1.3 Hz, respectively.

respectively. During these experiments, the position control was set to regulate a fixed angle (zero) as a person tried to move the ankle joint by hand, as in Fig. 2.8(a). The six-axis load cell was used at the joint to measure the torque applied by the person (which is the same as joint torque), and compare it to the commanded torque.[2] In an ideal case, these two torques will be equal, i.e., $\tau_j = n\tau_m$.

Fig. 2.15 depicts the resulting ankle torques of four different experimental cases. The first case, Fig. 2.15(a), shows a pure damping test (K_p=0 and K_d=29). The commanded torque has noise when the torque changes directions because this case only uses damping with joint velocity feedback, which has noise from taking the time derivative of the encoder reading. Cases two and three, Fig. 2.15(b–c), show low stiffness, reduced damping tests (K_p=46 and K_d=3) at small and large torques, respectively. Lastly, case four in Fig. 2.15(d) depicts a combined stiffness-damping control (K_p=172 and K_d=9). The figures show a strong agreement between measured joint torque and commanded motor torque in cases (a), (c), and (d), demonstrating that the effect of unmodeled dynamics is negligible for torques over ~10 Nm. Note that joint torques are much larger than 10 Nm during the stance phase of walking [128], making the actuator suitable for any type of compliant control during stance. The unmodeled dynamics only become apparent during the low torque tests, where a noticeable difference exists for amplitudes less than ~5 Nm (Fig. 2.15(b)). Interestingly, the difference between joint and commanded torque is around the previously observed value for the backdrive torque (~3 Nm).

Using the measured joint torque from the load cell and the measured angle and velocity from the encoder, we identified the K_p and K_d values from (2.1) as: (a) K_p=0 and K_d=23, (b) K_p=46 and K_d=2, (c) K_p=46 and K_d=2, and (d) K_p=172 and K_d=7. These closely resemble the prescribed values used for each individual test, especially K_p values. The least

[2]Note that the load cell was merely used for measurements and not for any kind of feedback control since the control paradigm does not require it. However, future controllers may require its feedback.

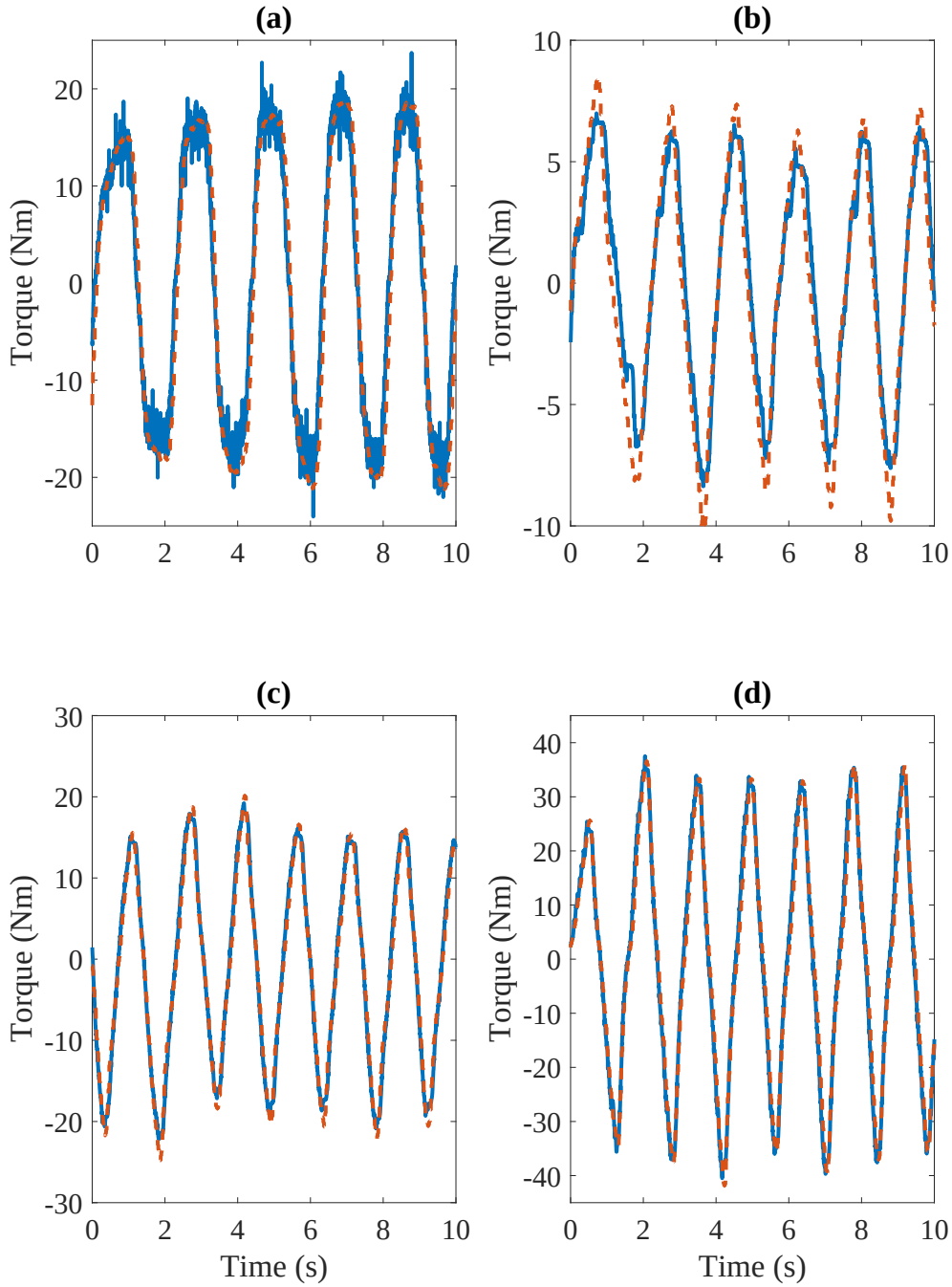

Figure 2.15: Open-loop impedance of the ankle joint with various K_p and K_d gains. Solid blue and dotted red lines correspond to commanded and measured torque, respectively. PD gains used are: a) K_p=0 and K_d=29, b) K_p=46 and K_d=3, c) K_p=46 and K_d=3, and d) K_p=172 and K_d=9.

Table 2.3: Subject specific information

Subject	Height (m)	Age (yrs)	Weight (kg)	Passive Knee	Passive Ankle
AB	1.760	39	73	N/A	N/A
TF	1.798	62	104	Rheo Knee XC	Pro-Flex XC Torsion

squares method was used to quantitatively evaluate the closeness of commanded torques, determined using the prescribed and identified gains in (2.1). For all trials, the coefficient of determination between the prescribed-commanded torque and the identified-commanded torque is 0.999, or $R^2 \cong 1$. The strong agreement between these values further proves that the effects of the system's unmodeled dynamics are negligible.

2.6.2 Walking Experiments

Walking experiments were conducted with one able-bodied (AB) subject and one transfemoral (above-knee) amputee (TF) subject. AB experiments aimed to assess and validate the capabilities of the hardware, whereas TF experiments aimed to assess clinical performance of the leg under the loading conditions for which it was designed. Note that the AB subject was an expert user of powered prostheses, having substantial experience walking on such devices. In contrast, the TF subject had never walked with a powered prosthesis prior to these experiments. Subject specific information and measurements are presented in Table 2.3.

Methods

Using the walking controller in Section 2.5.2, both subjects walked on the leg at different speeds on a treadmill (Fig. 2.16 and 2.17). All experimental procedures were approved

Table 2.4: Speed-independent control parameters. Parameters K_p and K_d are in Nm/rad and Nm.s/rad, respectively, and $q_{a,ms}$ and θ_d are in radians. Stance K_p are according to biological stiffness estimates from [106] and [107].

	K_p **(ankle)**	K_d **(ankle)**	θ_d **(ankle)**	K_p **(knee)**	K_d **(knee)**	θ_d **(knee)**	$q_{a,ms}$
Early stance	246	11	0	284	11	0.09	-
Mid-stance	992	17	0.07	284	11	0.09	0.07
Pushoff	-	17	time-based	458	11	time-based	-
Swing	688	17	time-based	573	23	time-based	-

Table 2.5: Speed-dependent control parameters. Parameters K_p and $q_{a,ms}$ are in Nm/rad and rad, respectively, and times are in seconds.

Subject	Speed	K_p**(ankle, push-off)**	$q_{a,po}$	t_{po}	t_{sw}	t_{td}
AB	0.9 m/s	344	0.14	0.55	0.86	0.95
	1.1 m/s	401	0.13	0.47	0.74	0.82
	1.3 m/s	458	0.12	0.40	0.63	0.70
	1.6 m/s	458	0.11	0.30	0.54	0.60
TF	0.9 m/s	286	0.10	0.35	0.58	0.65
	1.1 m/s	401	0.10	0.35	0.54	0.60
	1.3 m/s	458	0.10	0.35	0.54	0.60
	1.6 m/s	458	0.09	0.25	0.44	0.50

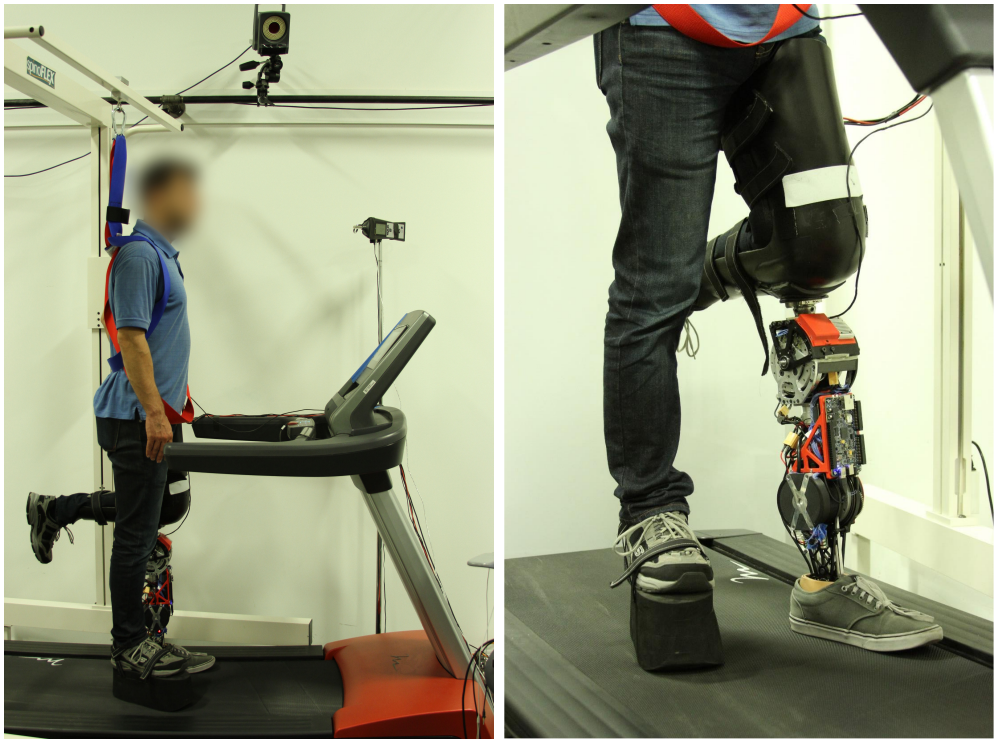

Figure 2.16: Experimental setup for able-bodied walking experiments. The image on the left shows the subject, safety harness, treadmill, and sound level meter. The image on the right shows how the prosthetic leg was connected to the bypass adapter, and how it was attached to the subject's leg.

by the University of Texas at Dallas Institutional Review Board, and signed consent was obtained from each subject prior to testing.

The AB subject wore the prosthetic leg through a custom bypass adapter and a shoe lift on the non-prosthetic leg to equalize their leg length to that of the prosthetic leg. A practicing, certified, and licensed prosthetist was present during the TF subject's experiment. This prosthetist fit and aligned the prosthetic leg directly on the TF subject's personal socket. While walking on the treadmill, both subjects wore a safety harness around their torso to prevent injury in the case of tripping or falling. An emergency stop button, which would disable the motors when pushed, was given to the subjects if they felt the need to stop at any time.

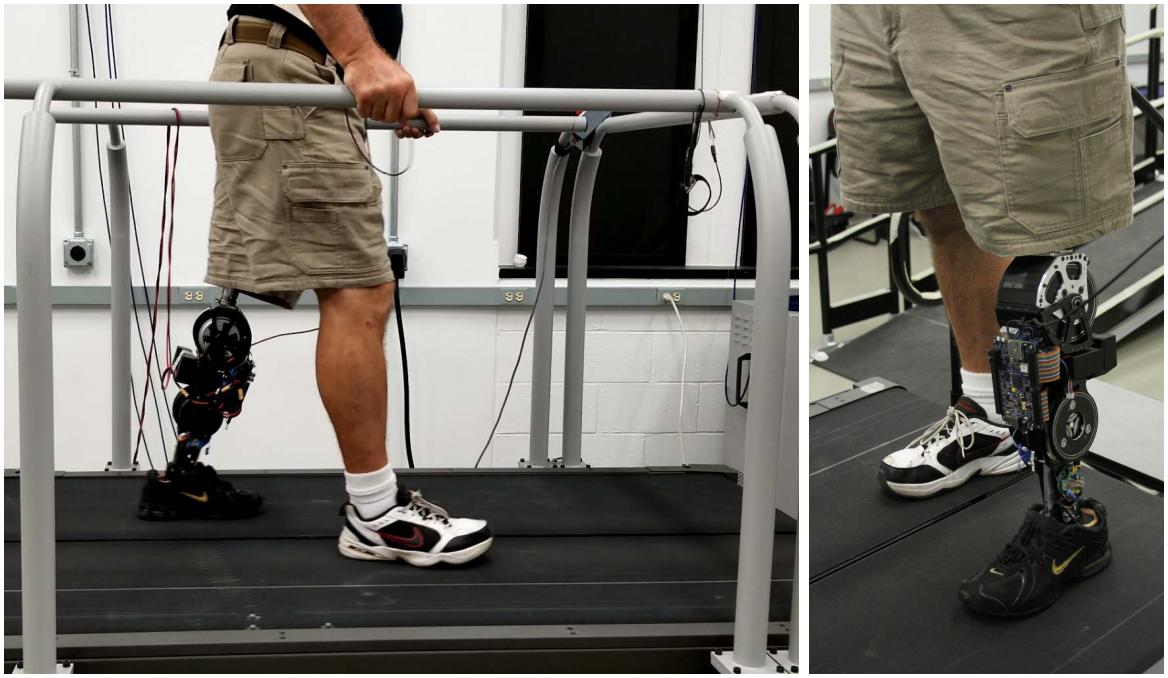

Figure 2.17: Experimental setup for amputee walking experiments. Both images show the amputee subject wearing the prosthesis on the instrumented treadmill. Note that although the batteries were mounted to the leg during these experiments, the leg was powered by identical off-board batteries to allow for the off-board measurement of current and voltage.

Each subject was asked to walk on the treadmill for approximately 60 seconds at a range of walking speeds (0.9, 1.1, 1.3, and 1.6 m/s), while wearing the powered prosthetic leg. In order to follow the speed-independent results of [106, 107], K_p and K_d values corresponding to impedance control states were held constant across speeds. The swing-phase PD gains were also held constant because of their negligible effect across different walking speeds. For the AB subject, only the push-off ankle gains (K_p) were tuned until the subject felt a comfortable propulsion force. Moreover, only push-off timing variables and one K_p value were tuned to be different for the TF subject relative to the AB subject. All other gains were kept consistent across subjects to display the potential for reduced tuning time. Tables 2.4 and 2.5 summarize the parameters used for these trials. The acclimation/tuning period before recording data with the TF subject lasted less than 30 minutes. Throughout the trials, gait kinematics and kinetics were collected for validation of the prosthetic leg. Disregarding

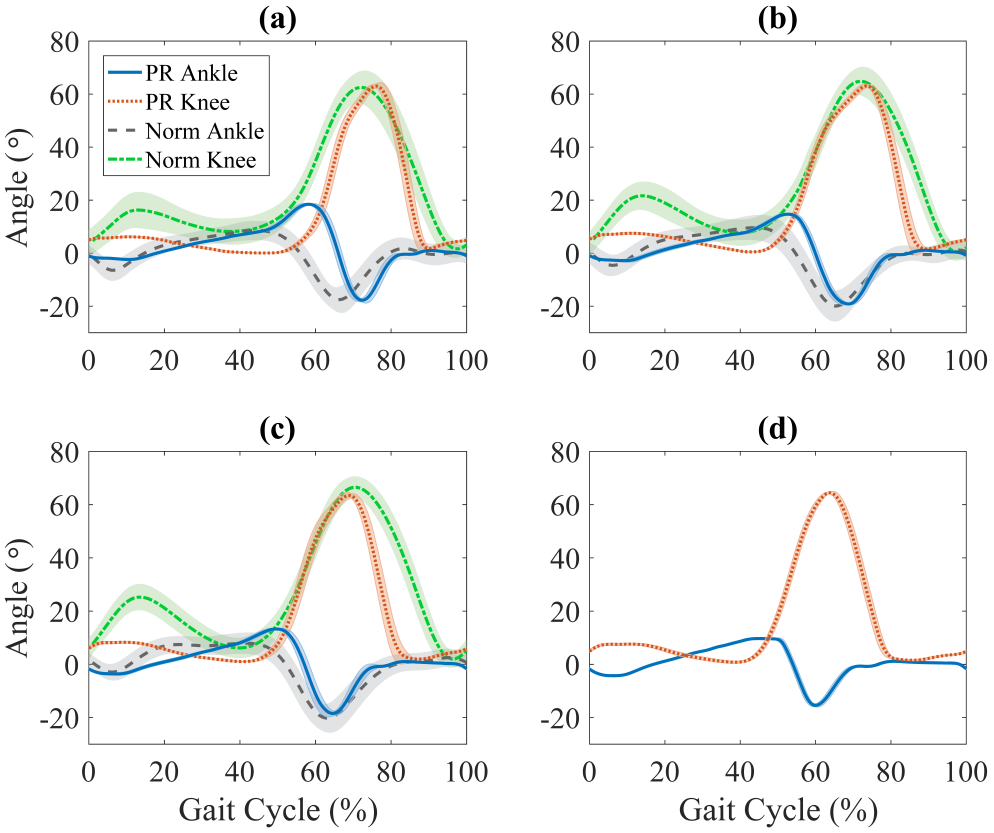

Figure 2.18: Prosthetic (PR) knee and ankle joint position during able-bodied walking with the prosthesis. Solid blue and dotted red lines correspond to the average ankle and knee joint angles, respectively for speeds: a) 0.9 m/s b) 1.1 m/s c) 1.3 m/s d) 1.6 m/s. Standard deviations (± 1) are indicated by shaded regions around the mean. Normative (Norm) knee and ankle trajectories [128] (not available for 1.6 m/s) are shown as a reference in green dash-dotted and gray dashed lines, respectively.

gait acceleration and deceleration at the beginning and end of the walking trial, 30 seconds of continuous, steady-state walking was captured for each speed. The data was divided and normalize by stride, which in turn allowed the calculation of gait statistics, such as means and standard deviations. To further study the actuator design during gait, two other measurements were recorded: power drawn from the battery and acoustic sound levels. To evaluate the electrical power consumption and regenerative capabilities of the leg, a current probe, TCPA300 (Textronix, Oregon, USA), was used to measure real-time current flowing to and from the entire leg. Current measurements, along with the battery's voltage, were

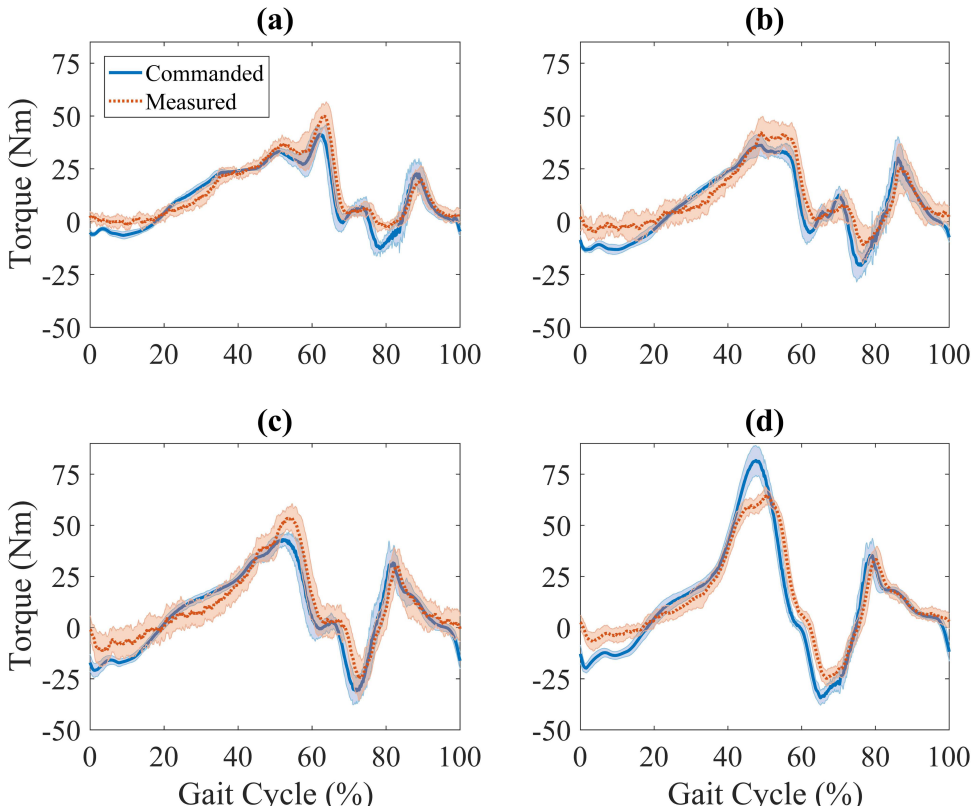

Figure 2.19: Average knee commanded and measured torque during able-bodied gait. Solid blue and dotted red lines correspond to the commanded and measured torque, respectively, for speeds: a) 0.9 m/s b) 1.1 m/s c) 1.3 m/s d) 1.6 m/s. Standard deviations (± 1) are indicated by shaded regions around the mean.

recorded by an off-board oscilliscope, DPO 2024B (Textronix, Oregon, USA), and saved to an off-board computer. Lastly, to investigate the acoustic sound level of the powered prosthetic leg, a PCE-322A sound level meter (PCE Instruments, Florida, USA) recorded the magnitude of sound coming from the leg during the walking trials. The sound meter was placed at the height of the user's ear, approximately 1.5 m away, to measure the magnitude of the sound heard from their perspective. Note, that sound level measurements were only taken during AB trials.

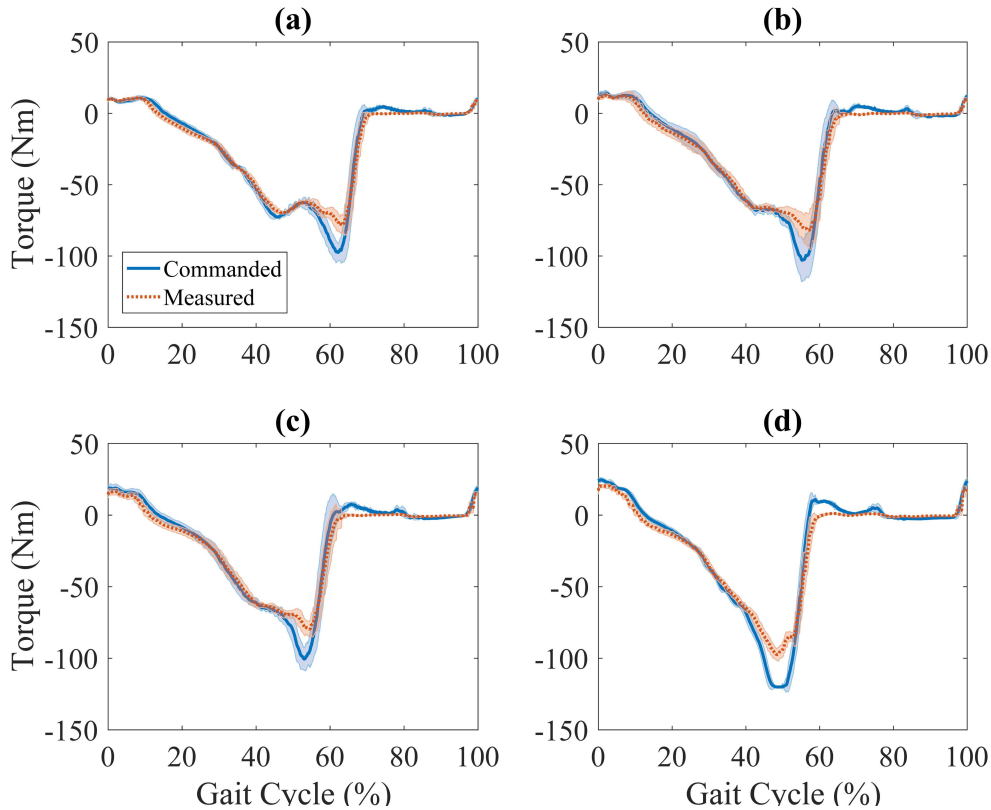

Figure 2.20: Average ankle commanded and measured torque during able-bodied gait. Solid blue and dotted red lines correspond to the commanded and measured torque, respectively, for speeds: a) 0.9 m/s b) 1.1 m/s c) 1.3 m/s d) 1.6 m/s. Standard deviations (± 1) are indicated by shaded regions around the mean.

Able-Bodied Walking to Validate Leg Capabilities

Kinematic and Kinetic Analysis: Fig. 2.18 shows the collected knee and ankle joint angles for different walking speeds and compares them to healthy (normative) gait kinematics [128]. Note that the healthy data set in [128] does not include high speed gaits for inclusion in 2.18(d). The gait cycle begins and ends at ground impact of the prosthesis, with the transition from stance to swing occurring around 60% of the gait cycle.

Figs. 2.19 and 2.20 depict the commanded versus measured torques of the knee and ankle joints, respectively, during walking experiments. As expected from the results of the bench-top tests, the commanded and measured torques closely match, confirming the hypothesis

regarding low actuator impedance and unmodeled dynamics. One notable difference is at peak negative torques in Fig. 2.20. At this point in gait, the excessively large joint acceleration makes the motor's inertia contribute more to the unmodeled dynamics of the actuator. However, since the joint's acceleration is larger than what is seen in healthy gait [128], we expect this discrepancy to be mitigated in future control schemes that better limit the joint's acceleration to normative values.

These biomechanical results demonstrate that the prosthetic leg can indeed perform as intended across walking speeds, and justify removing the torque sensors in the revised leg assembly used for amputee testing in Section 2.6.2.

Power Capabilities: This section examines the ability of the leg to output sufficient power during walking. Fig. 2.21 displays the leg's electrical and mechanical power over the average stride at each speed condition. The combination of the leg's current, i, and voltage, v, allows for the calculation of the prosthetic leg's total or consumed electrical power at each instant, $P = i \cdot v$. This power is indicated in Fig. 2.21 by $P_{Total:iv}$, where $Total$ indicates the inclusion of power at both joints, and iv indicates that it is based upon measured current and voltage. This power is compared against the leg's total output mechanical power, calculated using $P_{Total:\tau\omega} = \tau_{knee} \cdot \omega_{knee} + \tau_{ankle} \cdot \omega_{ankle}$, where $\tau\omega$ indicates that the power is based upon measured torque, τ, and measured velocity, ω. Additionally, knee power ($P_{Knee:\tau\omega}$) and ankle power ($P_{Ankle:\tau\omega}$) are presented.

Peak mechanical powers for the knee were 236.7, 192.1, 298.7, and 389.4 W, and the ankle peak mechanical powers were 246.1, 275.4, 294.2, and 371.6 W for 0.9, 1.1, 1.3, and 1.6 m/s, respectively. Peak specific powers (normalized by the subjects mass) were 3.24, 2.63, 4.09, and 5.33 W/kg for the knee, and 3.37, 3.77, 4.03, and 5.09 W/kg for the ankle across speeds.

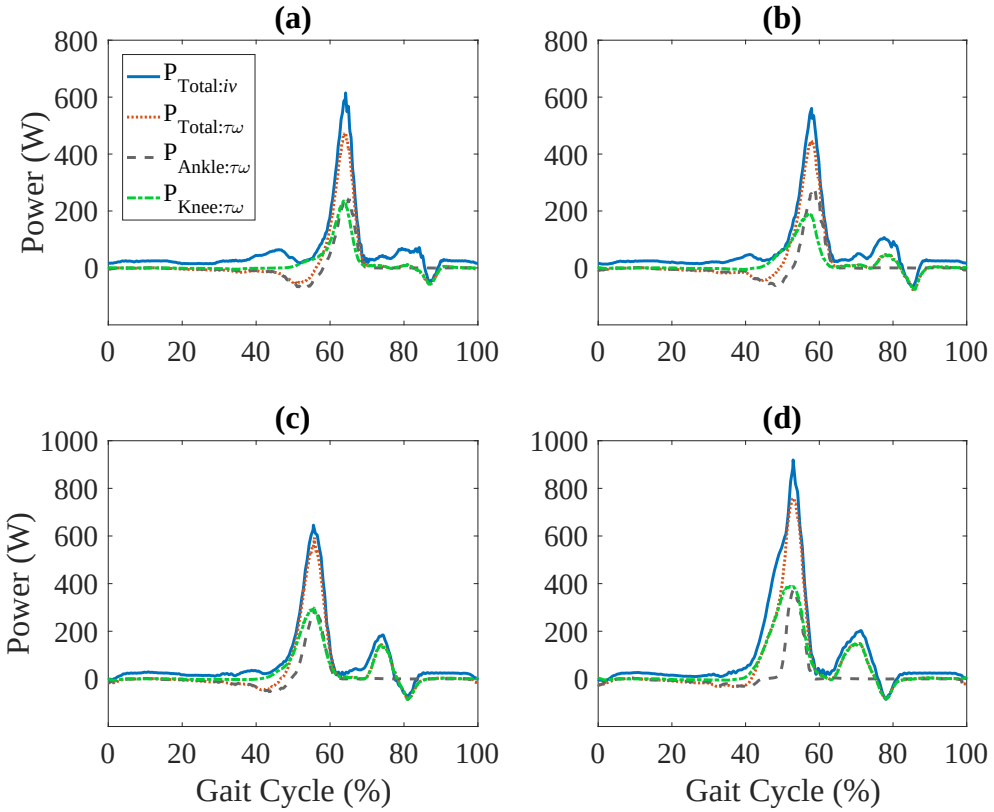

Figure 2.21: Average power per gait cycle of the prosthetic leg at different walking speeds for the able-bodied subject at a) 0.9 m/s, b) 1.1 m/s, c) 1.3 m/s, and d) 1.6 m/s. Solid blue lines indicate power calculated from measured current and voltage to and from the batteries. Dotted red lines indicate power calculated from measured torque and velocity. Dashed gray and dash-dotted green lines indicate joint power from measured torque and velocity for the ankle and knee, respectively.

Acoustic Sound Level: Fig. 2.22 compares the sound level of the presented prosthetic leg to a previously published leg that utilizes high-impedance actuators [86]. Note that the y-axis scale (dBA) is not linear, but logarithmic. In this figure, the gait cycle begins and ends at ground impact, with the transition from stance to swing occurring at about 60% of the gait cycle. It is evident that the leg with low-impedance actuators is much closer to the sound level of able-bodied walking than the leg with high-impedance actuators. As speed increases, the ambient, able-bodied, and low-impedance leg's sound levels were generally shifted upward in the figure, which is related to the increased sound of the treadmill. In

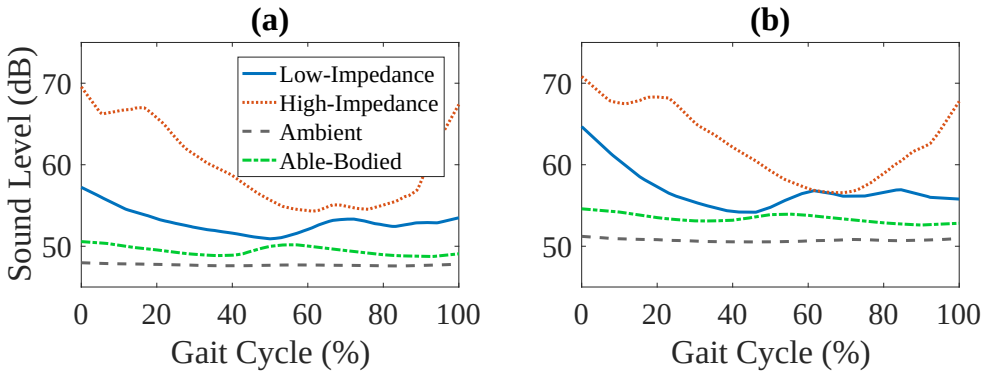

Figure 2.22: Acoustic sound level during gait at a) 0.9 m/s, b) 1.3 m/s. Solid blue, dotted red, dashed gray, and dash-dotted green lines represents the presented prosthetic leg with low-impedance actuators, a traditional powered prosthetic leg with high-impedance actuators, an able-bodied subject, and ambient sound levels, respectively, during treadmill walking. Ground contact of the prosthetic leg starts at 0% of the gait cycle.

fact, the difference between able-bodied and the low-impedance actuator's sound levels were fairly similar across speeds, not considering impact with the ground. Note that due to the low sampling rate of the sound level meter (10 Hz), large changes in sound level readings may look like instantaneous jumps in data, which explains why the values at 0% and 100% do not align for all cases. Interestingly, these instantaneous jumps between endpoints were not seen in the traditional actuation style. This likely due to the large velocities, and therefore increasing sound, of the prosthetic actuators leading up to impact impact. Therefore, we can conclude that since the low-impedance actuators are much quieter than the high-impedance actuators, ground-impacts and ambient sound levels have a greater contribution to the sound level of walking with low impedance actuators.

It is evident that the low-impedance actuation is much quieter than the traditional actuation. Specifically, the presented leg is on average 7 dB and 6 dB quieter (including impacts) than that of the conventional powered leg at 0.9 and 1.3 m/s, respectively. If impacts were disregarded, we expect the difference would be much greater.

Amputee Walking to Assess Clinical Performance

Kinematic Analysis: Fig. 2.23 shows the collected knee and ankle joint angles of the prosthesis during TF walking at different speeds, and compares them to healthy (normative) gait kinematics [128]. Although the subject typically preferred that push-off began earlier in the gait cycle than healthy averages, their joint kinematics resemble that of healthy joints in terms of magnitudes and general trends. Specifically, as speeds increase, push-off shifts earlier in the gait cycle. Furthermore, the early push-off resulted in a decreased prosthetic stance phase, and therefore a prolonged prosthetic swing phase, which is common in amputee gait. This resulted in a longer period of knee extension before heel strike. However, this affect was diminished at faster speeds, where the kinematics became more normative.

Power & Energy Analysis: Fig. 2.24 presents the power of the prosthesis during walking with the TF subject, similar to the AB case in Section 2.6.2. Because the torque sensors were removed in the TF case, the power is based upon commanded torque, τ, and measured velocity, ω, where we previously saw that commanded torque is an accurate representation of actual torque. By integrating these curves, electrical and mechanical energies were calculated and presented in Table 2.6. Positive values in this table indicate produced energy (integral of power greater than zero), whereas negative values indicate regenerated energy (integral of power less than zero). Specifically, $E_{P_{Knee:\tau\omega}}$, $E_{R_{Knee:\tau\omega}}$, $E_{P_{Ankle:\tau\omega}}$, and $E_{R_{Ankle:\tau\omega}}$ indicate produced knee, regenerated knee, produced ankle, and regenerated ankle mechanical energies, respectively. Furthermore, $E_{P_{Total:\tau\omega}}$ and $E_{R_{Total:\tau\omega}}$ indicate the produced and regenerated mechanical energies of the combined joints (i.e., from $P_{Total:\tau\omega}$). Note that these two values do not directly equal the sum of the produced or regenerated energies of the individual joints. Instead, they arise from the combined joint mechanical energies of the leg as a whole, which accounts for power sharing between the joints. The total efficiency of the prosthesis is defined as $\eta = (|E_{R_{Total:iv}}| + E_{P_{Total:\tau\omega}})/(E_{P_{Total:iv}} + |E_{R_{Total:\tau\omega}}|)$, where $E_{P_{Total:iv}}$ and $E_{R_{Total:iv}}$ are the

Table 2.6: Average energy (E) in joules and efficiency (η) of the leg per gait cycle during amputee walking. P and R indicate energy produced and regenerated, respectively. K and A represent mechanical energy of the knee and ankle joint, respectively. $Total : \tau\omega$ represents the combined mechanical energy of both joints. $Total : iv$ represents electrical energy from the battery.

	$E_{P_{Knee:\tau\omega}}$	$E_{R_{Knee:\tau\omega}}$	$E_{P_{Ankle:\tau\omega}}$	$E_{R_{Ankle:\tau\omega}}$	$E_{P_{Total:\tau\omega}}$	$E_{R_{Total:\tau\omega}}$	$E_{P_{Total:iv}}$	$E_{R_{Total:iv}}$	η (%)
0.9 m/s	5.9	-10.4	9.5	-13.8	13.0	-21.8	27.4	-6.7	40.1
1.1 m/s	7.8	-15.0	7.7	-12.4	9.7	-21.6	21.8	-7.4	39.4
1.3 m/s	8.4	-18.7	7.4	-13.3	9.3	-25.5	21.4	-11.2	43.7
1.6 m/s	21.3	-14.4	17.8	-12.5	36.8	-24.6	57.6	-11.4	58.7

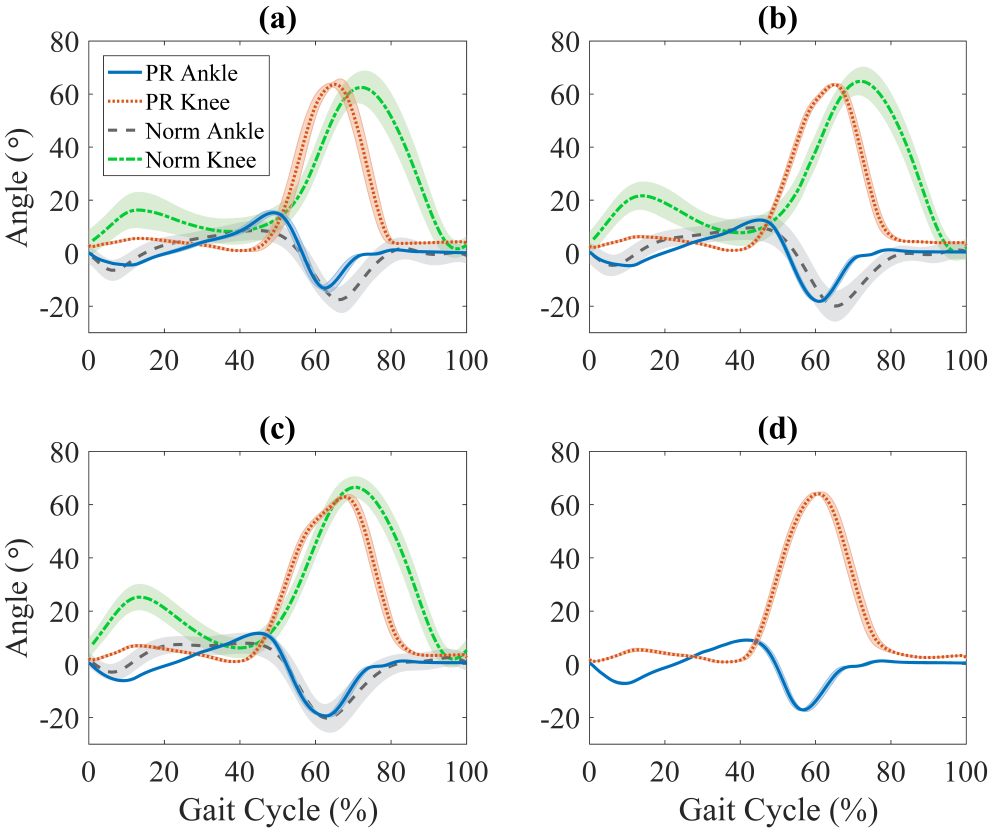

Figure 2.23: Prosthetic (PR) knee and ankle joint position during amputee walking with the prosthesis. Solid blue and dotted red lines correspond to the average ankle and knee joint angles, respectively for speeds: a) 0.9 m/s b) 1.1 m/s c) 1.3 m/s d) 1.6 m/s. Standard deviations (± 1) are indicated by shaded regions around the mean. Normative (Norm) knee and ankle trajectories [128] (not available for 1.6 m/s) are shown as a reference in green dash-dotted and gray dashed lines, respectively.

produced and regenerated electrical energies, respectively. The numerator accounts for the "output" energy flowing to the battery and environment, and the denominator accounts for the "input" energy flowing from the battery and environment. Note that as speed increases, efficiency also increases. One contributing factor to this was the constant 20 W consumed by the electronics and onboard computer, which has more influence on the efficiency relative to mechanical power during slow walking. Moreover, at slower walking speeds, the motors provide torques at lower velocities, where the electric motor is less efficient due to winding losses.

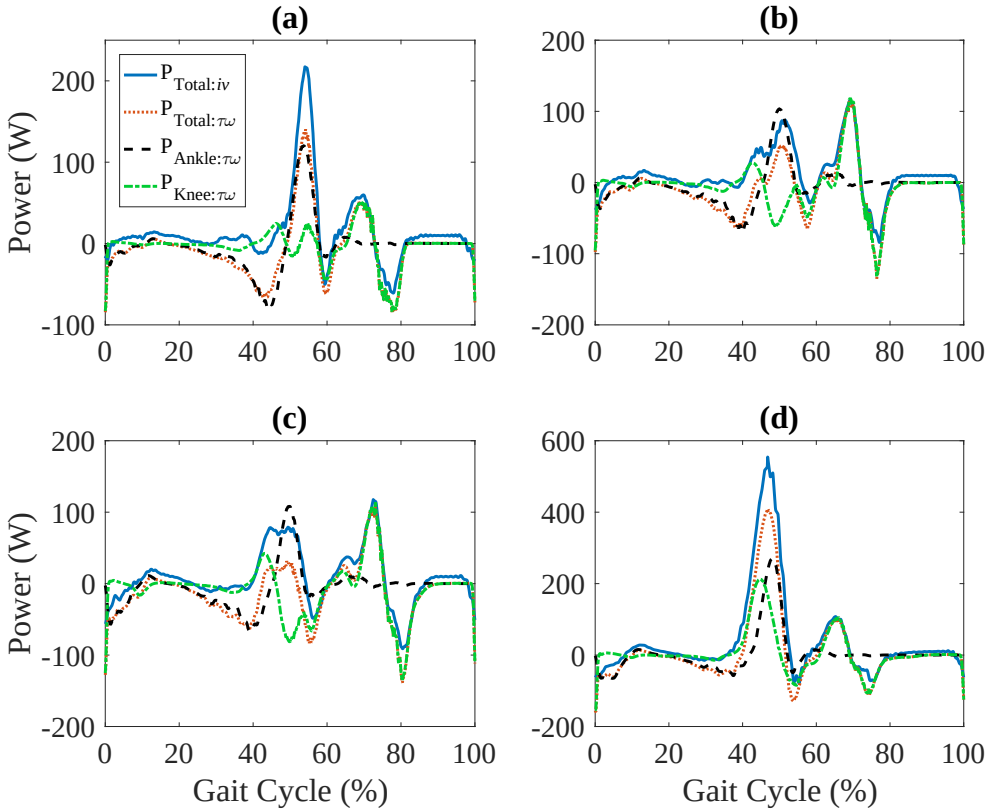

Figure 2.24: Average power per gait cycle of the prosthetic leg at different walking speeds for the amputee subject at a) 0.9 m/s, b) 1.1 m/s, c) 1.3 m/s, and d) 1.6 m/s. Solid blue lines indicate power calculated from measured current and voltage to and from the batteries. Dotted red lines indicate power calculated from measured torque and velocity. Dashed gray and dash-dotted green lines indicate joint power from measured torque and velocity for the ankle and knee, respectively.

Similar to the AB case, the TF subject shows regions where rapid deceleration of joints cause power regeneration. This is most evident in Fig. 2.24, between approximately 75% and 80% of the gait cycle. We also see regions where power was being shared between the joints, such as Figs. 2.24 (a)-(c) between approximately 35% and 45% of the gait cycle, where the ankle mechanical power was negative while knee power was positive. Interestingly, this is also seen in Figs. 2.24 (a) and (b) at approximately 50% of the gait cycle, which allowed for an ankle mechanical power that was larger than the electrical power to the entire leg.

This was caused by the large regenerative power of the knee during the same instance, which reduced the power demand from the batteries.

Both energy sharing and regeneration aid in reducing the average energy consumed per gait cycle. Our new prosthetic leg has an average specific power of 0.14, 0.11, 0.08, and 0.40 W/kg (normalized by the subject's mass) for 0.9, 1.1, 1.3, and 1.6 m/s, respectively. With the selected batteries, the prosthetic leg can currently operate for 2.82, 3.74, 4.92, and 0.99 hours of continuous walking, or 7301, 10514, 14875, and 3263 prosthetic steps at each respective speed. Note that the total step count for the user would double when considering the intact limb.

2.7 Discussion

2.7.1 Advantages of Design

The main objective of this work was to achieve low-impedance actuation in a powered prosthetic leg and to analyze its performance. Initial benchtop tests concluded that with the motors off, the actuators have sufficiently low impedance, with a backdrive torque of ~1-3 Nm and free swing capability. Other tests demonstrated that even with low-impedance actuators, the prosthesis was still able to provide very large torque (>180 Nm), thus satisfying our torque design goals. Furthermore, by measuring the actuator's open-loop frequency response, we found the actuator's inertia to be $I = 0.0696$ km·m^2, which is very close to the estimated inertia from the CAD model, $I = 0.0625$ km·m^2, and is less than the state-of-art leg in [59].

For context and comparison, Table 2.7 presents the estimated reflected inertias of the actuators in several other powered prostheses. Note that in this table, values for reflected inertia only consider the motor rotor inertia and transmission ratio, omitting the inertias of the transmission components (hence the presented actuator's inertia is reported as 0.0557).

Table 2.7: Comparison of inertias, transmission ratios, and joint torque of prosthestic leg actuators.

	Motor	Motor Inertia 10^{-4} (kg·m^2)	Gear Ratio	**Rotor Reflected Inertia at the Joint (kg·m^2)**	**Continuous Joint Torque (N·m)**	ρ (N·m/kg·m^2)
Low-Impedance Leg - Knee and Ankle	Robodrive ILM 85x26	1.1500	22:1	0.0557	57.2	1027
UTD Leg 1 - Knee[a] **[87]**	Maxon EC-4 pole 30	0.0333	360:1	0.4316	34	80
UTD Leg 1 - Ankle[a] **[87]**	Maxon EC-4 pole 30	0.0333	720:1	1.7263	69	40
Vanderbilt Leg Gen. 3 - Knee [59]	Maxon EC-4pole 30	0.0333	176:1	0.1032	17	165
Vanderbilt Leg Gen. 3 - Ankle [59]	Maxon EC-60	1.1950	115:1	1.5804	46	29
Open-Source Leg - Knee [7]	T-Motor U8	1.3000	49.4:1	0.3172	47	148
Open-Source Leg - Ankle[a] **[7]**	T-Motor U8	1.3000	58.4:1	0.4434	55	125
Ampro [133]	Moog BN34	0.0510	80:1	0.3264	34	104
CMU Leg [118]	Robodrive ILM 85x13HS	0.6100	50:1	0.1525	71.5	469
Utah AVT Knee [a] **[119]**	Maxon EC-4pole 22	0.0089	25-375:1	0.0006-0.1252	1-20	1667-0.01
Utah Polycentric Ankle [a] **[16]**	Maxon EC-4pole 30	0.0333	120-800:1	0.0479-2.1312	11-76	229-36

[a]Based on estimated average transmission ratios since actual ratios can vary based on joint kinematics

This was done for consistency when comparing across actuators, since we do not have access to the CAD models or system identification data for these prostheses. Moreover, when comparing actuators, it is also important to compare torque capabilities since an actuator's reflected inertia can easily be reduced at the cost of torque. Therefore, Table 2.7 also presents the ratio of continuous (nominal) joint torque to joint reflected inertia, ρ. Larger values of ρ indicate an actuator's ability to achieve large continuous torques with respect to its reflected inertia.

Note that the Utah AVT knee [119] is the only prosthesis which has a larger ρ than that of the presented prosthesis. This is achieved when its actively variable transmission minimizes its reduction ratio, therefore minimizing the reflected inertia of the actuator. However, to do this, the subject must stop and unload the prosthesis for a short period of time while the transmission adjusts, which does not allow for quick switching between low-impedance and high-torque. This is most important during the push-off phase of gait when the leg requires large torques immediately followed by low impedance, which allows for knee free swing and rapid ankle dorsiflexion for toe clearance. Similarly, the Utah Polycentric Ankle prosthesis [16] has a variable transmission with a minimum reflected inertia (0.0479) at approximately 20° of dorsiflexion, but it has a larger reflected inertia than the presented prosthesis throughout the majority of its range of motion. On the other hand, the presented prosthesis inherently has low impedance, and can switch to high stiffness/torque very quickly, which makes it desirable for push-off and very suitable for other highly dynamic or extreme tasks. Although it is unrealistic to reduce the joint reflected inertia to that of a human joint, which is considered negligible [128], we were able to achieve a compromise between low reflected inertia and high torque to increase ρ compared to other prostheses. In addition to having the largest constant ρ, and to the best of our knowledge, the presented actuators can produce the largest torque of any self-contained powered prosthesis throughout the literature. The tradeoff in terms of weight is discussed in Section 2.7.2.

Open-loop impedance control tests demonstrated that the effects of unmodeled actuator dynamics are negligible for torques over ~10 Nm. The strong agreement of commanded and measured joint torques during AB walking confirmed this hypothesis during gait. Moreover, the compliant nature of the actuators, coupled with the implementation of human joint impedances, allowed the joints to naturally favor biological reference trajectories during the stance phase of gait. These trends are evident in both the AB and TF walking experiments, indicating the potential for simplifying the tuning process compared to traditional actuation schemes. Although further optimization and tuning would be necessary to more closely match normative trajectories, the presented walking experiments demonstrate the possible reduction in tuning time when human joint impedances are directly implemented.

In addition to accurate impedance control, the actuators maintain the ability to accurately control position. This was first demonstrated in benchtop experiments, where the leg successfully tracked positions for frequencies up to 1.3 Hz with negligible error. As the frequency of the trajectory increases, the first visible discrepancy between desired and actual trajectories in Fig. 2.14 appears at knee flexion and extension immediately after the touch-down phase. In this region of gait, active position tracking is not strictly required because the function of the knee is to absorb energy, which was achieved through impedance control in walking experiments.

Across all speeds in the AB walking experiments, the prosthetic leg's knee and ankle angles (PR Knee and PR Ankle) were similar to that of the normative knee and ankle reference trajectories (Norm Knee and Norm Ankle) in Fig. 2.18. Slight discrepancies were seen at some speeds because the controller utilizes reference trajectories for normal walking speed (1.1 m/s), which explains why joint angles were qualitatively similar to the normative trajectories in Fig. 2.18 (b). Furthermore, AB walking experiments demonstrated increased peak power capabilities compared to previous design approaches [60, 82, 93]. Specifically, during AB walking experiments, the prosthesis displayed peak joint powers of ~380 W, which

is greater than the original design goal and the ~200 W and ~250 W peak power reported in [60] and [115], respectively. Furthermore, the peak power available to each actuator is more than 1 kW, which makes the leg suitable for more extreme tasks. Although the amputee subject exhibited similar push-off powers at the fastest speed, a different walking style was adopted at slower speeds that resulted in lower push-off powers than normal (Fig. 2.24). It is likely that the TF subject's lack of experience with a powered leg contributed to consistently early transitions into swing when walking at slower speeds (Fig. 2.23). Additional training and experience may be needed for the TF subject to leave the prosthetic foot on the ground longer, therefore better utilizing the push-off capabilities.

An interesting ancillary benefit of low-impedance actuators is similar to that of series elastic actuators (SEAs). Although the actuators implemented in the presented leg do not have an elastic element, they do have the ability to store energy. During phases of negative joint work, the generated energy can either be used within the leg's electrical system, to power the other joint, or to recharge the leg's batteries. This reduces power consumption and increases the efficiency of the prosthetic leg for an extended battery life. Moreover, the low gear ratio reduces the amount of friction and reflected inertia that the motors have to overcome, thus further increasing the efficiency of the leg. To quantify this, a power analysis of the prosthetic leg was conducted, which revealed a practical design advantage through a reduction in the average required power, compared to previous design approaches [60, 82]. During the TF walking trial, the prosthesis demonstrated an average specific power of 0.4 W/kg per gait cycle at very fast walking speeds (1.6 m/s), which is lower than the 0.98 W/kg and 0.88 W/kg average seen in [60] and [115], respectively. Although we observed even lower specific powers at slower speeds, those cases are not used for comparison because of the lower push-off powers observed. Nevertheless, the decreased power consumption allows the leg to take between 3263 and 14875 prosthetic steps on a single charge of the selected batteries. These values are more than sufficient for the daily use of an average transfemoral amputee,

who takes ~1540 prosthetic steps per day [35]. Moreover, energy analysis shows that the total mechanical energy is close to net-zero, similar to able-bodied walking [128].

Very little is presented throughout the literature on the acoustic sound level of assistive devices [28] and powered prosthetic legs [117]. The acoustic sound level becomes important to consider when attempting to translate this emerging technology to the consumer. Upon investigation, the prosthetic leg with low-impedance actuators was on average 6 dB to 7 dB quieter than a prosthetic leg with conventional actuation (see Fig. 2.22). In fact, peaks seen in the new actuator's sound level at the beginning of the gait cycle actually originate from impact with the ground, instead of the leg's actuators. Since control of foot planting was reduced when walking with a prosthetic leg, which continues to decrease as speeds increase, the jump in sound is likely to be a result of the controller managing the leg at impacts. In comparison to typical household items, the sound level of the high-impedance prosthetic leg is akin to a vacuum cleaner (60 dB to 70 dB at ~1.5 m), which is similar to the 70 dB (at ~1 m) presented in [117]. However, the low-impedance prosthetic leg is akin to a refrigerator or an electric tooth brush (50 dB to 60 dB at ~1.5 m)[88]. Efforts can be made to further reduce the sound level of the prosthesis by enclosing or insulating the actuators, similar to commercial products.

2.7.2 Limitations

Concerning the design of the presented prosthetic leg, its weight is the top limiting factor for clinical acceptance. A large portion of the leg's weight comes from the leg's structure and electric motors in the actuators. There is a tradeoff between an actuator's mass and its available power. For example, series elasticity could be used to lower the motor's power, therefore lowering the motor's mass. However, the addition of an elastic element (such as a spring) and other structural complexities would likely increase the total mass of the actuator. Low-impedance actuators avoid these components and will continue to get lighter as the torque and power density of motor technology improves over time.

An additional tradeoff is between the motor's mass and the actuator's backdrivability. Assuming the length of the motor is constant (which is typically determined by geometrical constraints), the following properties for scaling the motor in the radial direction hold [104]: motor torque $\tau_m \propto r_{gap}^2$, motor inertia $I_m \propto r_{gap}^3$, and motor mass $m_m \propto r_{gap}$, where r_{gap} is the distance from the axis of rotation to the center of the gap between the stator and rotor, or gap radius. Based on these relations, the gear ratio for a fixed joint torque $\tau_j = n\tau_m$ scales with $n \propto 1/r_{gap}^2$. Then the reflected inertia at the joint will scale as $I_j = n^2 I_m \propto 1/r_{gap}$. Furthermore, increasing r_{gap} to achieve a lower reflected inertia typically results in a larger motor mass. On the other hand, the gear ratio is proportional to $1/r_{gap}^2$, which results in a smaller/lighter transmission with reduced friction [104].

Achieving low-impedance actuation resulted in a knee-ankle prosthesis with a mass of 6 kg, which is 1-2 kg heavier than some state-of-art knee-ankle prostheses [59, 7, 95]. Other recent works, such as the lightweight powered prosthetic joints in [63, 119, 64], have achieved a mass of 1-2 kg for a single actuated joint. Although the low-impedance actuation scheme tends to be heavier than other powered prostheses, we believe the added mass is justified through the increased power and torque available to both joints, which produces larger pushoff and ground reaction forces. At the same time, the presented mass of 6 kg is much lighter than the 8.1 kg [39] and 11 kg [118] of other prostheses with similar power/torque ratings. Moreover, exploiting the proprioceptive characteristics of the actuator for detecting ground contact [126] could allow the removal of the load cell at the ankle, thus reducing the leg's mass by another 0.2 kg.

With the design of the leg now validated, additional amputee trials can conducted to investigate clinical outcomes, such as the actuators' effect on gait compensations. Specifically, we expect that the increased torque-bandwidth of the actuators will provide greater propulsion and toe clearance, thus reducing hip-hiking, vaulting, and circumduction. Optimizing these outcomes may require additional tuning to reduce the deviation of joint kinematics

from normative patterns, which was larger than that reported with some other powered prostheses [114]. Tuning could also improve the push-off output power at the cost of energy consumption. However, the various scenarios tested in this study suggest the leg will remain efficient as gait properties change.

2.8 Conclusion

This paper presented the design and experimental validation of a powered prosthetic leg with high-torque, low-impedance actuators. The system implements high-torque motors coupled with low-reduction transmissions. Low mechanical impedance is an inherent feature of the actuators' design, resulting in low backdrive torques to move the motors.

Benchtop tests showed that the low-impedance actuators have negligible unmodeled actuator dynamics. This was further confirmed through the implementation of human walking impedances into an impedance-based walking controller, which demonstrated that accurate torque control is achievable without torque feedback. The low-impedance actuators were also able to maintain precise position tracking in both benchtop and walking experiments. The compliant nature of the prosthesis allowed for smooth transitions between the impedance- and position-based portions of the walking controller, such as the transition from high output torques at push-off to high speeds at toe off. Furthermore, the low-impedance actuators presented practical advantages through reduced power consumption and acoustic sound levels.

Future work will include clinical testing with additional amputees to assess the effect the prosthesis has on gait compensations. Additional design revisions may be made to further simplify and reduce the weight and volume of the leg using light-weight materials, fewer sensors, and smaller electronics. Lastly, this prosthetic leg will be further used as a platform for control prototyping to advance the field of prosthetic leg control.

CHAPTER 3

REDUCING TRANSFEMORAL AMPUTEE HIP COMPENSATIONS WITH A POWERED PROSTHESIS: A CASE SERIES[1]

Authors – Toby Elery, Siavash Rezazadeh, Emma Reznick, Leslie Gray, and Robert D. Gregg

The Department of Mechanical Engineering, ECSW 3.1

The University of Texas at Dallas

800 West Campbell Road

Richardson, Texas 75080-3021

Corresponding author: Toby Elery

3.1 Author Contributions

T. Elery and R. Gregg devised the project and main conceptual ideas. T. Elery conceived and planned experiments. T. Elery, E. Reznick, and S. Rezazaheh and conducted experiments with support from L. Gray. T. Elery and E. Reznick collected experimental data, and conduced post processing and data analysis. T. Elery wrote the first draft of the manuscript. All authors contributed to the interpretation of the results and discussion, and provided critical feedback and helped shape the final manuscript. R. Gregg supervised the project.

3.2 Abstract

Gait with passive prostheses is often burdened with compensations due to the lack of push-off power at the ankle. Powered prostheses can restore some functionality, but there is little evidence that shows their effect on compensatory behaviors, specifically at the residual hip. Therefore, this chapter is aimed at investigating how powered prostheses can be leveraged to mitigate residual hip compensations. Walking experiments were conducted with amputees using a low-impedance powered prosthesis compared to their day-to-day passive prosthesis. A walking controller was implemented on the powered prosthesis to exploit the low-impedance actuators' power density during push-off, impedance control abilities in stance, and trajectory tracking abilities to ensure toe-clearance during swing. Experiments show that when large push-off power is provided, less power is demanded from the residual hip to progress the limb forward. Moreover, all subjects displayed increased step length and propulsive impulses for the prosthetic side, compared to their passive prostheses. These results reduce demand on the hip to accelerate the body forward and display the ability to improve gait symmetries. Hip circumduction improved for subjects who had previously exhibited this compensation on their passive prosthesis. The improvements made to these compensations lead to reduced residual hip power and work, which can reduce fatigue and overuse injuries.

3.3 Introduction

Passive or semi-active prostheses are commonly used to restore gait after a lower-limb amputation, however the resulting gait is often asymmetric and compensatory in nature [129, 75, 44, 47, 49]. Semi-active prostheses, such as the Ottobock C-Leg, aim to reduce these compensations by utilizing microprocessors to control the damping of joints via small actuators that manipulate hydraulic valves during the user's gait [9]. This design approach allows for a single product to be easily adaptable to a variety of subjects, environments, and tasks. However, semi-active devices can only dissipate energy from the user, and therefore cannot fully restore gait to that of an able-bodied individual. This is mainly due to the lack of push-off power from the ankle during late stance and locked knee flexion during early stance [8, 36]. This results in a gait burdened with compensations, such as increased joint work at the hip to accommodate for missing work at the knee and ankle[31, 110], and asymmetric kinematic deviations from normative gait, such as increased hip circumduction or decreased hip flexion[8, 72, 31]. Prolonged repetition of these compensations can have detrimental effects on a person's health, comfort, and pain levels [31, 89, 43]. For instance, asymmetries in gait can lead to knee osteoarthritis [76], muscle atrophy [54], and chronic back pain [54]. Mitigating compensatory behaviors and asymmetries should be a driving factor when designing a prosthesis to aid those with limb loss.

In the last decade, a great amount of research has gone into the design of powered prosthetic limbs [84, 82]; some of these devices were shown to increase symmetry in joint kinematics [94, 85] and load distribution[74], and reduce muscle activity in the lower back [45]. Although great progress has been made with these devices, there is still a lack of evidence that powered prostheses can decrease amputee hip compensations. Rezazadeh et al. displayed that a powered prosthesis reduced vaulting and circumduction in one transfemoral amputee [94]. Although these compensations were reduced, the rigid actuation scheme of

the prosthesis resulted in toe-stubbing, which can lead to other hip compensations like hip-hiking or increased hip work. Most powered prostheses implement similar stiff actuation styles, which have high mechanical impedance. This means that they require large load torques to backdrive the motor; also described as having low backdrivability [87, 64]. This design philosophy limits the actuator's force and position bandwidth, limiting highly dynamic portions of gait [59, 94, 119]. Push-off, for example, involves a rapid change from high-torque at low-speed to low-torque at high-speed, which requires very high bandwidth. Therefore, designs that limit this bandwidth risk stubbing the toe during the swing phase and reducing push-off power, which is critical in returning normative functionality to persons with limb loss, and is a leading factor in gait asymmetry and compensations [105]. Furthermore, these limitations have shown to be crucial in how persons with limb loss load their intact limb, which can have long term detrimental effects on their joints [31, 74].

As a starting point to address these challenges, we recently designed a powered knee-ankle prosthesis with low mechanical impedance, or high-backdrivability, see Chapter 2. This prosthesis displays several practical benefits, such as reduced overall energy consumption and acoustic noise levels, but also has benefits related to control and power density. Preliminary tests proved that the intrinsic impedance and unmodeled dynamics of the actuators were sufficiently small to control joint impedance without torque feedback. Similarly, the actuators demonstrated precise position tracking capabilities throughout benchtop and walking experiments. Testing demonstrated increased actuator torque, power, and position bandwidth compared to high-impedance actuators. The increased capabilities of this prosthesis, coupled with the range of applicable control schemes available, suggest that this device may be uniquely suited to meet the varying needs of gait.

To further exploit the capabilities and flexibility of this style of actuation, this paper introduces a control scheme that utilized both its impedance and trajectory tracking abilities. Impedance control is utilized during the stance phase to provide biomimetic forceful interac-

tion with the ground, as shown in [59]. Time-based kinematic control is used during push-off, when the foot is still on the ground, to promote large plantarflexion power and forward propulsion. Lastly, a time-invariant kinematic control method, based on a phase variable derived from thigh motion [87], is utilized to provide user synchronization across walking speeds and kinematic variations. Although previous implementations of time-invariant kinematic control have been limited to stiff actuation styles, this method has demonstrated promising results with both rhythmic and nonrhythmic activities, including more symmetric gait and reduced compensations in one user [94].

We expect that the combination of this actuation and control scheme will lead to reductions in residual limb compensations. Specifically, we predict the increased force bandwidth inherent to this style of actuation, coupled with time-based kinematic control during push-off can be leveraged to provide more push-off (or plantarflexion) power at the ankle. Since increased push-off power is correlated to an increase in propulsive impulse, it is possible to see improved symmetry between the braking and propulsive impulses of the prosthesis [136, 99]. This can lead to improved symmetry between the prosthesis's propulsive impulse and the intact limb's braking impulse, which has been linked to increased power at the residual hip [40, 105]. With reductions in these compensations, we expect to see smoother joint power and reduced mechanical work at the residual hip, which can mitigate fatigue and long term injuries [100, 89, 43]. We also expect that the increased position bandwidth should allow quick ankle and knee flexion between terminal stance and mid-swing for increased toe-clearance [94], reducing the need for compensations such as circumduction. The phase-based swing controller can ensure that essential joint kinematics that provide toe-clearance are correctly timed for each step, further diminishing the need for circumduction.

Methodologies relating to the hardware, experimental protocol, and powered prosthetic control are discussed in Section 3.4. The effects on symmetries and compensations are presented in Section 3.5 and discussed in Section 3.6.

(a) (b)

Figure 3.1: (a) The powered prosthesis with high-torque, low-impedance actuators used in experimentation. (b) Experimental setup, including a subject wearing the powered prosthesis while standing on the instrumented treadmill and wearing reflective markers on their lower body.

3.4 Methods

3.4.1 Hardware

This study uses a powered transfemoral prosthesis (Fig. 3.1(a)), whose detailed design is described in [25], with two high-torque, low-impedance actuators at the knee and ankle. Each actuator has an ILM 85x26, frameless, brushless, DC motor kit (Robodrive, Seefeld, Germany), and custom a 22:1 single-stage stepped-planet compound planetary gear transmission. A R80/80 Solo Gold Twitter motor driver (Elmo Motion Control, Petah Tikva, Israel) is used in low-level current control. Optical quadrature encoders, E5 (US Digital, Washington, USA), is used for motor position feedback to the motor drivers and to the con-

Table 3.1: Subject information and measurements

	TF1	TF2	TF3
Height (m)	1.746	1.716	1.798
Weight (kg)	77.3	74.9	104.0
Age (yrs)	33	39	62
Amputated Side	Left	Left	Left
Number Years Post Amputation	13	10	15
Day-to-day Knee Prosthesis	Ottobock 3R60	LegWorks All-Terrain	Ossur Rheo XC
Day-to-day Ankle/ Foot Prosthesis	Ottobock Axtion 1E56	Ottobock Axtion 1E56	Ossur Proflex XC w/ Torsion

troller. To measure thigh angle, a 3DM-CX5-25 Inertial Measurement Unit, or IMU (Lord Microstrain, Williston, VT, USA), is attached to the thigh portion of the knee actuator. A M3564F 6-axis load cell (Sunrise Instruments, Nanning, China) is located below the ankle joint axis to detect ground contact, measure ankle torque, and monitor ground reaction forces/moments. Mounted below the 6-axis load cell is a size 28 (cm) Pacifica LP prosthetic foot (Freedom Innovations, Irvine, CA, USA). All sensors interface with the system's microcontroller, a myRIO (National Instruments, Austin, TX, USA). The controller presented in Section 3.4.3 is implemented in the LabVIEW software environment and then imported onto the myRIO. The leg is powered through four onboard LiPo batteries, TP870-3SR70 (Thunder Power, Las Vegas, NV, USA), connected in series. The overall mass of the leg is 6.09 kg, not including the cosmetic foot shell or shoe.

3.4.2 Experimental Protocol

The following experimental protocol was approved by the Institutional Review Boards of the University of Texas at Dallas, the University of Texas Southwestern Medical Center, and

Table 3.2: Subject self-selected walking speeds

	TF1	TF2	TF3
Slow (m/s)	0.9	0.8	0.8
Normal (m/s)	1.1	1.0	1.0
Fast (m/s)	1.3	1.2	1.2

the University of Michigan. A clinical researcher, who is a practicing, certified, and licensed prosthetist, was present during all experimentation. Three subjects were recruited through the clinical researcher, with written informed consent and without bias of race or gender. Each subject had been independently ambulating for at least two months, with amputations at the transfemoral (above-knee) level.

The clinical researcher fit the powered prosthesis to each subject, ensuring the knee height, knee rotation, and foot progression angle were properly aligned. Anatomical and subject-specific information is presented in Table 3.1. A training session was conducted with each subject before experimentation with the powered prosthesis, which lasted less than 30 minutes. The training sessions were kept short to keep the focus on how the device acutely altered their typical gait. The subjects began their training/acclimation session by walking overground and through handrails. Once the subject felt comfortable with the powered prosthesis, they began walking on the treadmill to allow more consecutive steps. Once the prosthesis was tuned for the individual and the subject could consistently walk without the use of handrails, the training session was concluded and recording trials began. During the treadmill walking trials, the subjects were encouraged to walk without the use of handrails, unless they felt unstable. Each subject walked on the treadmill for approximately 60 seconds with their day-to-day passive prosthesis and the powered prosthesis at their self-selected slow, normal, and fast walking speeds (Table 3.2), resulting in a total of 6 walking trials.

While walking on the treadmill, the subjects wore a ceiling-mounted safety harness in case of trips or falls. Additionally, the subjects were given emergency stop buttons for both

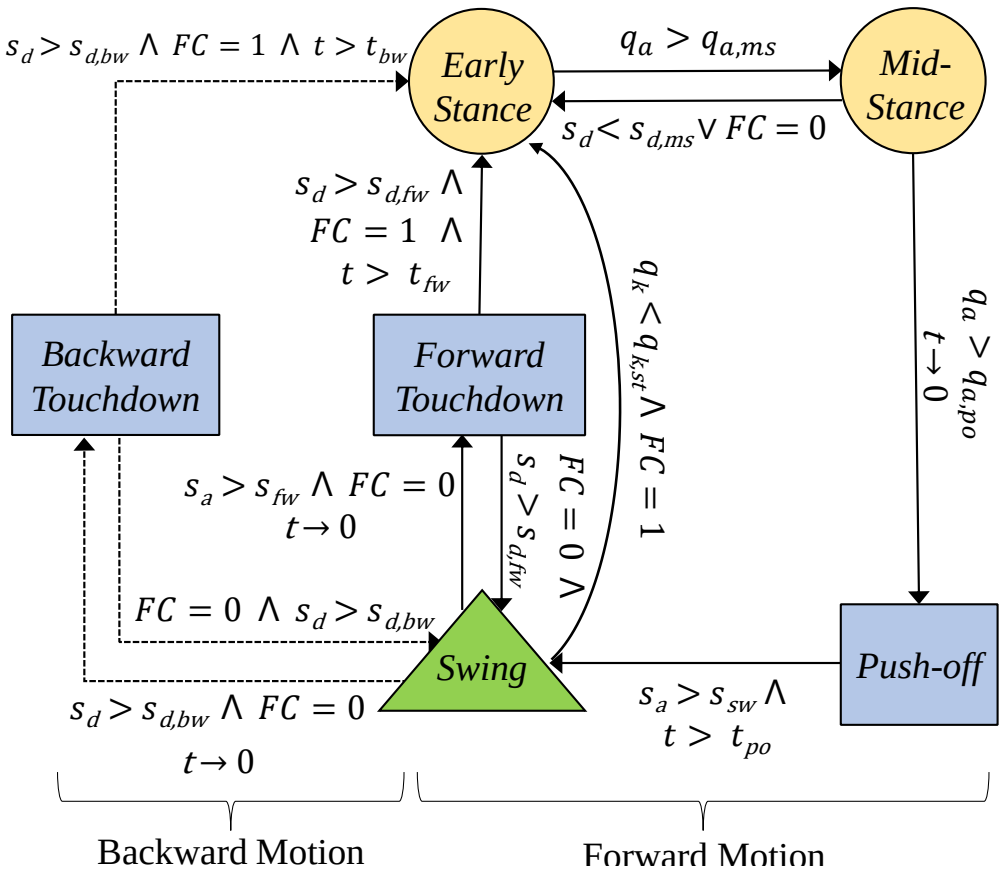

Figure 3.2: Finite state machine representation of the proposed controller. The yellow circles correspond to impedance controlled states; the blue rectangles to time-based position controlled states; and the green triangle to the position control based on a holonomic phase variable.

the treadmill and powered prosthesis, which they were instructed to press at any point if they felt the need to stop. Furthermore, the subjects were informed that they were allowed to opt-out of the experiment if at any point they felt uncomfortable.

3.4.3 Control

The presented controller is based on a Finite State Machine (FSM), depicted in Fig. 3.2. The general structure of the FSM has been taken from [94], where a holonomic controller was designed to manage different rhythmic and non-rhythmic tasks. Although the presented controller is similar in structure to previous works, the control in each FSM state and the

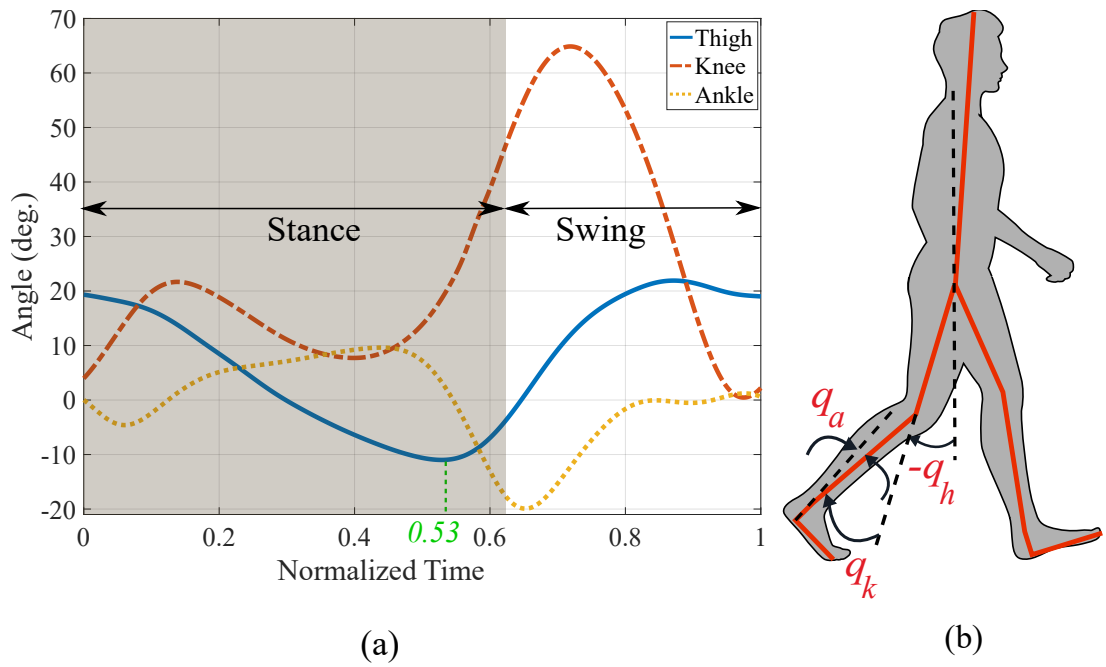

Figure 3.3: (a) Human leg's joint angle trajectories during one stride of walking with normal speed and stride period T [128]. (b) Definition of the joint angles. Figure was adopted from [94].

transition conditions between these states have changed. These changes are implemented as a result of the mathematical singularities in the structure of the controller [94], which prevents a holonomic phase variable to perform optimally in the push-off and touchdown phases. To resolve this problem, similar to [59], we prescribe time-based reference trajectories for joint angles (from normative able-bodied data [128]). Note that in [59], push-off, swing, and touchdown are all time-based. Whereas, in our work, the swing phase is based on the holonomic phase variable presented in [94]. As shown in [94], this provides the ability to manage volitional tasks such as walking backward and over obstacles.

Another difference with the controller presented in [94] is the two states corresponding to the stance phase. We use an open-loop impedance controller for these states to take advantage of the low-impedance of the designed actuator. As we showed in [24], due to its negligible unmodeled dynamics and frictions, the designed actuator is capable of performing open-loop impedance control with small errors. This means that the human joints'

Table 3.3: Speed-independent control parameters. Parameters K_p and K_d are in $N{\cdot}m/rad$ and $N{\cdot}m{\cdot}s/rad$, respectively. θ_d is in rad and is nonconstant when noted as time- or phase-based, TB and PB, respectively. Parameters in parentheses are specific to TF3.

	Ankle			Knee		
	K_p	K_d	θ_d	K_p	K_d	θ_d
Early Stance	202 (246)	9 (11)	0	235 (286)	9 (11)	286
Midstance	812 (991)	9 (11)	229	235 (286)	9 (11)	286
push-off	563 (688)	14 (17)	TB	469 (573)	19 (23)	TB
Swing	563 (688)	14 (17)	PB	469 (573)	19 (23)	PB
Touchdown	202 (246)	9 (11)	TB	235 (286)	9 (11)	TB

Table 3.4: Speed-dependent control parameters

Subject	Speed	$q_h^{min}(rad)$	$q_{a,po}(rad)$	$t_{po}(s)$
TF1	Slow	-0.192	0.108	0.400
	Normal	-0.192	0.113	0.400
	Fast	-0.192	0.105	0.360
TF2	Slow	-0.192	0.108	0.400
	Normal	-0.192	0.106	0.400
	Fast	-0.192	0.105	0.360
TF3	Slow	-0.192	0.108	0.400
	Normal	-0.192	0.100	0.400
	Fast	-0.244	0.092	0.360

quasi-stiffness values, reported in [107] and [106], can be applied without requiring torque feedback. This can greatly shorten the long parameter tuning sessions associated with open-loop impedance controllers [112]. Note that these biological values were directly implemented for the experiments outlined in this paper, and slightly reduced for the acclimation session. TF1 and TF2 kept the reduced values during the experimental trials, whereas TF3 preferred the original biological values (see Table 3.3).

The transitions among the states of the FSM is performed based on foot contact ($FC = 1$) for stance states, time in time-based states, ankle angle for impedance-controlled states, and two phase variables for phase-controlled states, which are defined similarly to [94]:

$$s_d = \frac{q_h^0 - q_h}{q_h^0 - q_h^{min}} \cdot c, \tag{3.1}$$

$$s_a = 1 + \frac{1 - s_d}{q_h^0 - q_h^{min}} \cdot (q_h - q_h^0), \tag{3.2}$$

where q_h^0 and q_h^{min} are constant values defined by touchdown thigh angle and the minimum of the reference thigh angle trajectory, respectively. These two parameters can be tuned to the individual's preference. The constant c is also tunable and is related to the ratio of the stance phase to the entire gait cycle. The default value of c is the normalized time at which q_h reaches its minimum, which is 0.53 in Fig. 3.3(a). The transitions are prescribed as follows:

1. *Transition between early and mid-stance*: When the ankle angle becomes greater than $q_{a,ms}$, the system will transition from early stance to mid-stance to accommodate more joint stiffness to prepare for push-off. Conversely, if the foot contact is lost or the thigh angle rises above s_d, the system goes back to early-stance, as the conditions for push-off preparation are not met.

2. *Transition from mid-stance to push-off*: When the ankle angle becomes greater than $q_{a,po}$, the transition to push-off occurs and time is set to zero. This is a one-way transition, such that the system cannot return to stance from the push-off state.

3. *Transition from push-off to swing*: As mentioned, push-off is a time-based state and as such, the instant of transition to swing is determined by the preset push-off duration (t_{po}). To avoid premature transitions, the controller starts the swing phase only if, in addition to the duration condition, the thigh moves sufficiently forward and its angle reaches s_{sw}.

4. *Transition from swing to forward and backward touchdown*: These transitions happen when the foot has not touched the ground yet, but a pre-specified forward (corresponding to $s_{d,fw}$) or backward (corresponding to $s_{d,bw}$) thigh angle is reached. As mentioned, by transition to forward or backward touchdown states, the controller prepares the leg for a smooth touchdown.

5. *Transition from forward and backward touchdown to (early) stance*: Both touchdown states are time-based and thus the primary conditions for these transitions are the preset durations (t_{fw} and t_{bw}). The stance phase will start when the foot touches the ground ($FC = 1$), however, only if the thigh angle has stayed above the previous limits (corresponding to $s_{d,fw}$ and $s_{d,bw}$).

6. *Transition from forward and backward touchdown to swing*: If the foot has not touched the ground and the absolute thigh angle becomes smaller than the values corresponding to $s_{d,fw}$ and $s_{d,bw}$, the FSM moves back to the swing phase. This will enable the user to perform volitional maneuvers while their leg is in the air, as we have previously shown in [94].

7. *Direct transition from swing to early stance*: This transition happens if the foot touches the ground during swing and the knee angle is smaller than some specified value.

Speed-independent control parameters that remained constant across subjects had the following values: $q_h^0 = 0.367$ radians, $q_{k,st} = 0.524$ radians, s_{fw} =0.999, $s_{d,fw} = 0.1$, $s_{d,ms} = 0.2$, $s_{d,bw} = 0.53$, $s_{sw} = 0.65$, $t_{fw} = 0.2$ seconds, $t_{bw} = 0.2$ seconds, and $c = 0.53$. Other parameters that required slight tuning or vary with speed are shown in Tables 3.3 and 3.4, respectively.

3.4.4 Data Acquisition and Analysis

During walking trials, the subjects walked on an instrumented split-belt treadmill (Burtec, Columbus, OH, USA), seen in Fig. 3.1(b), which collected ground reaction forces at 1000 Hz. The subjects were outfitted with reflective markers, also in Fig. 3.1(b), for lower body kinematics to be collected from our ten-camera motion capture system (Vicon, Oxford, UK) at 100 Hz. The conjunction of the instrumented treadmill and the motion capture system also allowed for lower limb joint powers (W) to be collected (100 Hz). Total joint work (J) is determined for the residual hip and is found by the sum of positive work (integral of positive power) and a fraction of absolute negative work (integral of negative power). Taking a fraction of negative work is based on the fact that although some mechanical energy can be stored within the body, a portion still contributes to the subject's metabolic energy consumption. We moderately estimate that 50% of negative work is expended by the user [21]. Information relating to the powered prosthesis was saved on the myRIO at 500 Hz and used to determine the prosthetic joint power (W).

To measure circumduction, we begin by estimating each foot's center. This is done by averaging the location of all the markers on each foot. Circumduction is then defined by the lateral deviation of the foot center in mid-swing compared to stance, similar to [108]. Mid-swing is determined by the instant when the swing leg's foot center and crosses the stance leg's foot center during anterior-posterior motion. The lateral foot deviation is calculated for each step, then averaged for each subject, foot, and trial. Braking and propulsive impulses ($N \cdot s/kg$) are found by integrating the positive and negative posterior-anterior ground reaction forces, respectively.

We use the symmetry index (SI),

$$SI = \left| \frac{A - B}{\frac{1}{2}(A + B)} \right| \tag{3.3}$$

similar to [94, 80, 99], to quantify symmetry between two variables. Variables A and B represent different values throughout the paper. Specifically, A and B represent propulsive

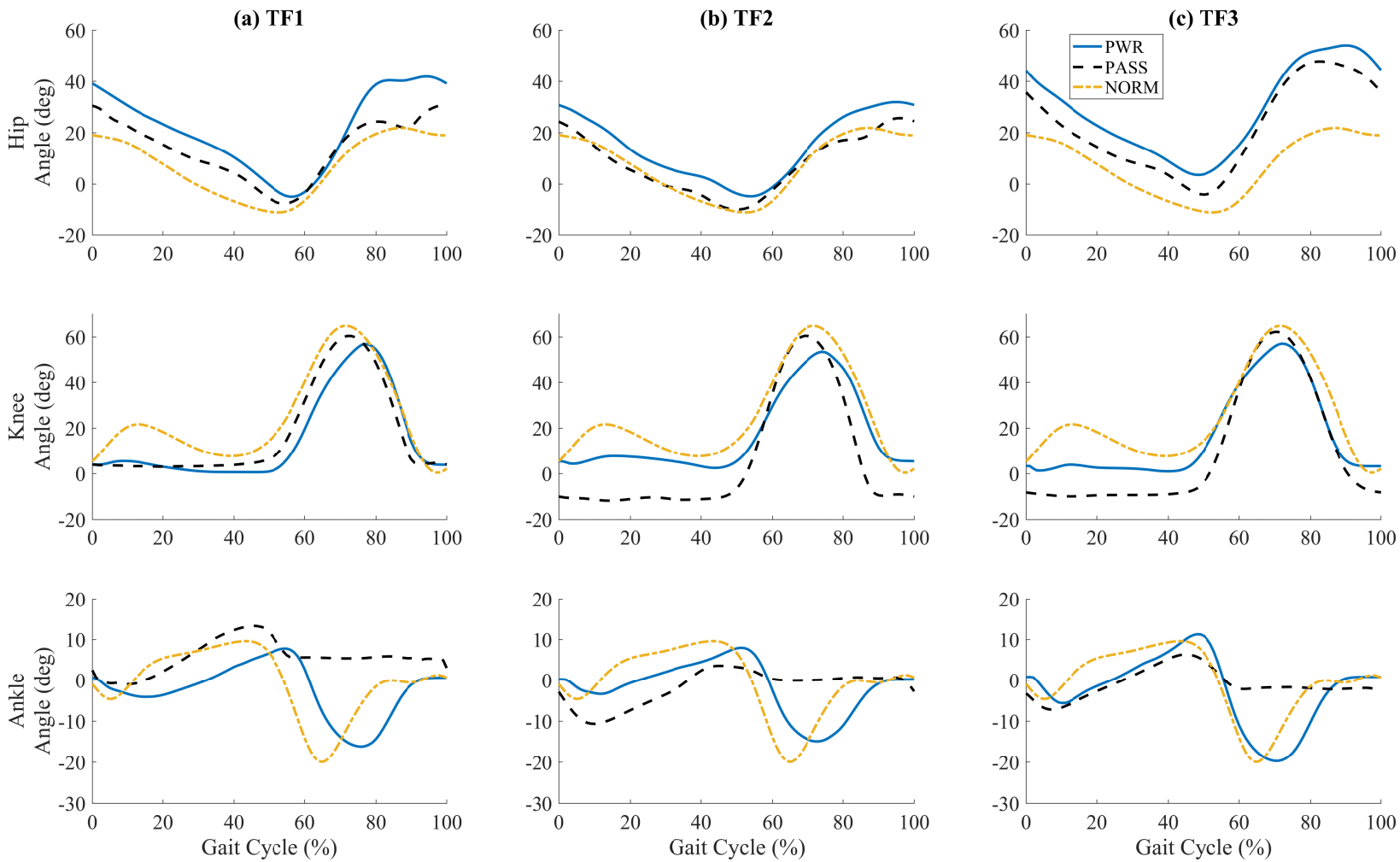

Figure 3.4: Average prosthetic side joint kinematics at normal speeds throughout the gait cycle (normalized by time). Columns (a), (b), and (c) correspond to subjects TF1, TF2, and TF3, respectively. Top, middle, and bottom rows correspond to hip, knee, and ankle joint angles respectively. Solid blue lines indicate average angles for trials where the subject wore with the powered prosthesis (PWR), black dashed lines indicate trials where the subject wore their personal passive prosthesis (PASS), and dash-dotted yellow lines indicate healthy normative values (NORM) [128].

and braking impulses, respectively, in Fig. 3.6 and Table 3.5. Alternately, A and B represent values on the left and right legs, respectively, in Tables 3.8 and 3.7. When $SI = 0$, A and B are perfectly symmetric, whereas deviation from zero indicates increasing asymmetry. Lastly, tabular results that appear in bold indicate an improvement in the powered prosthesis's values compared to the passive prosthesis.

3.5 Results

3.5.1 Transfemoral Amputee Subject 1

Maximum ankle plantarflexion was returned to normative levels during powered trials, most notably at the push-off phase of gait (∼50-70% GC), see Fig. 3.4(a). Ankle push-off power was increased for TF1 during slow speeds when walking with the powered prosthesis (Fig. 3.5(a)), but was similar in magnitude to the passive trials at normal and fast speeds. Although prosthetic ankle power did not increase for higher speeds when wearing the powered prosthesis, TF1 did exhibit increased prosthetic propulsive impulse across all speeds. This resulted in improved symmetry between braking and propulsive impulses for the powered prosthesis at fast speeds, and for the intact side at all speeds (Fig. 3.6(a)). Furthermore, the increase in prosthetic propulsive impulse resulted in improved symmetry between the prosthetic propulsive impulse and intact braking impulse, see Table 3.5.

Beginning at early stance (∼0-10% GC) of the passive trials, TF1 exhibits a large spike in positive prosthetic-side hip power, see Fig. 3.7(a). This behavior is mitigated when walking with the powered prosthesis. Furthermore, a large reduction in prosthetic-side hip negative power is evident at late stance (∼45% GC) for all speeds of the powered trials. Across speeds, the residual hip displays an increased concentric pull-off power when wearing the powered prosthesis, which can be seen in Fig. 3.7(a) at ∼65-70% GC. Note that this increase is less noticeable at slow speeds when prosthetic ankle power is large. During passive trials,

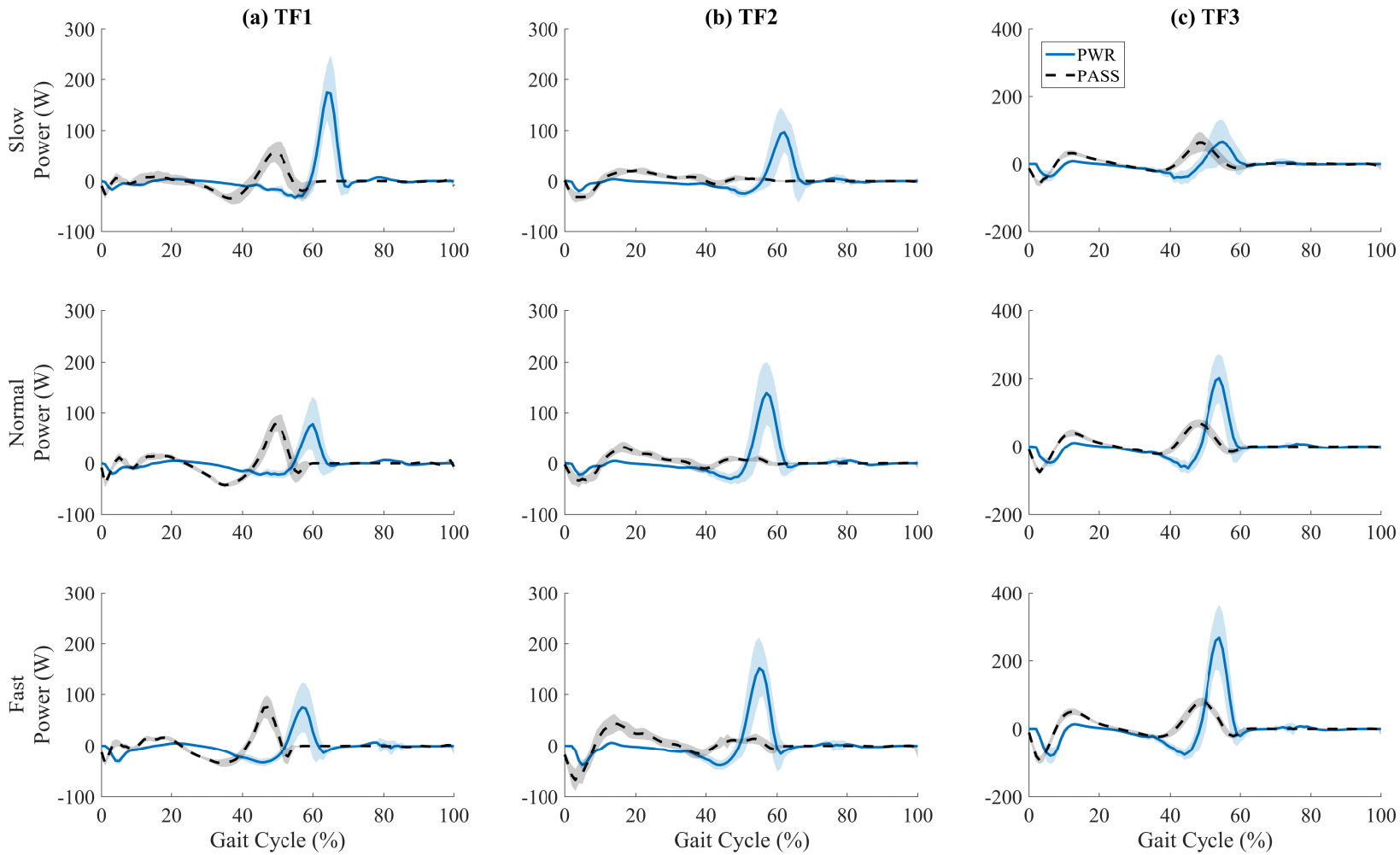

Figure 3.5: Average prosthetic ankle power throughout the gait cycle (normalized by time). Columns (a), (b), and (c) correspond to subjects TF1, TF2, and TF3, respectively. Top, middle, and bottom rows correspond to slow, normal, and fast speeds, respectively. Solid blue lines indicate average power for trials where the subject wore with the powered prosthesis (PWR), and black dashed lines indicate trials where the subject wore their personal passive prosthesis (PASS). Shaded areas around the averages indicate ± 1 standard deviation.

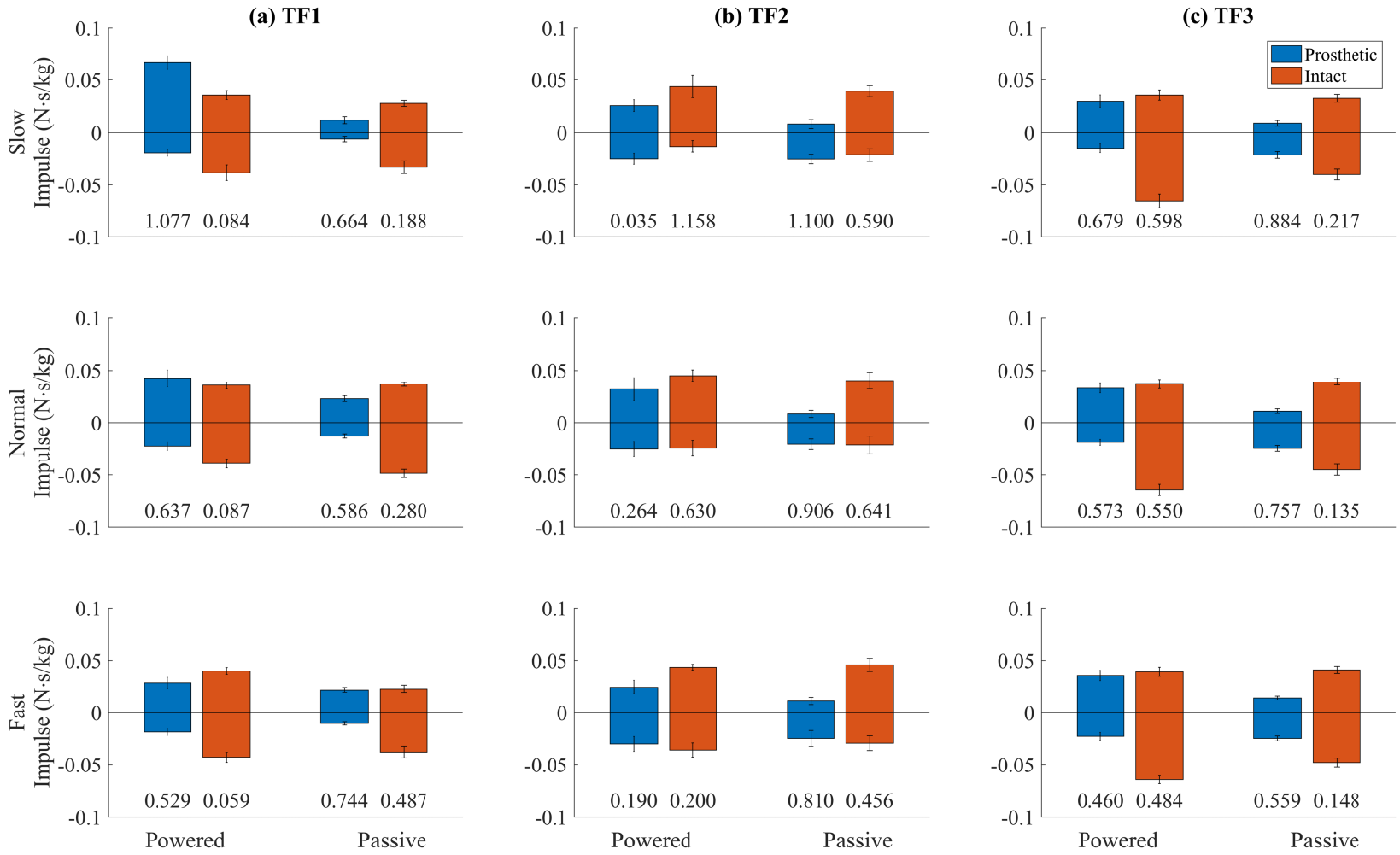

Figure 3.6: Average propulsive (positive) and braking (negative) impulses when walking with the powered and passive prostheses. Columns (a), (b), and (c) correspond to subjects TF1, TF2, and TF3, respectively. Top, middle, and bottom rows correspond to slow, normal, and fast speeds, respectively. Within each sub-figure, the bars are paired depending on the prosthesis worn. Corresponding symmetry indices between average propulsive and braking impulses for each individual side are shown below each set of bars. Black error bars centered at the positive and negative extremes indicate ± 1 standard deviation.

Table 3.5: Symmetry index between prosthetic propulsive impulse and intact braking impulse.

Subject	Speed	Powered	Passive
TF1	Slow	**0.522**	0.981
	Normal	**0.080**	0.730
	Fast	**0.403**	0.526
TF2	Slow	**0.704**	0.981
	Normal	**0.311**	0.953
	Fast	**0.368**	0.966
TF3	Slow	**0.841**	1.319
	Normal	**0.648**	1.122
	Fast	**0.567**	1.100

TF1 displays a large magnitude oscillation between positive and negative power at the end of prosthetic swing (∼90% GC), resulting in rapid hip flexion/extension at the same time (see Fig 3.4(a)). This behavior was not seen in powered trials, in fact, greater hip flexion is was displayed in this phase of gait compared to passive trials. Lastly, when integrating hip power, we see a 16% average decrease in the residual hip work when wearing the powered prosthesis (Table 3.6).

Aside from joint powers and impulses, we also examined how the powered prosthesis affects other compensatory behaviors, such as reduced step length and hip circumduction. When wearing the powered prosthesis, TF1 displayed an increased step length on both the prosthetic and intact side, at all speeds (Table 3.7). Furthermore, symmetry between the left and right leg step length was improved for normal speeds. Although symmetry decreased for slow and fast speeds, the difference in SI was very small (∼0.01 and 0.04, respectively). TF1 also displayed reduced hip circumduction at all speeds, for both the right and left leg (Table 3.8). Despite the fact that circumduction was reduced for both hips, the SI between the two sides was increased for all speeds.

Table 3.6: Average hip work per stride in joules for the residual limb.

Subject	Speed	Powered	Passive
TF1	Slow	**17.7**	23.4
	Normal	**25.5**	29.0
	Fast	**21.4**	24.0
TF2	Slow	**13.8**	17.7
	Normal	**17.5**	22.1
	Fast	**25.0**	26.9
TF3	Slow	**62.1**	62.6
	Normal	**64.0**	71.1
	Fast	**71.1**	75.7

3.5.2 Transfemoral Amputee Subject 2

During walking with their passive prosthesis, TF2 displayed very little prosthetic ankle push-off power and plantarflexion. However, it can be seen in Fig. 3.5(b) and Fig. 3.4(b) that the powered prosthesis provided a drastic increase in ankle push-off power and plantarflexion across all speeds. TF2's gait also showed an increased prosthetic propulsive impulse across all speeds when wearing the powered prosthesis, see Fig. 3.6(b). This resulted in improved symmetry between braking and propulsive impulses for both the prosthetic and intact leg, except for the intact leg at slow speeds. Furthermore, the increase in prosthetic propulsive impulse resulted in improved symmetry between the prosthetic propulsive impulse and the intact braking impulse.

Across all speeds, the prosthetic-side hip peak-to-peak power is reduced for TF2, see Fig. 3.7(b). TF2 exhibits a decrease in peak negative prosthetic-side hip power during powered trials at ∼30-50% GC. Concentric pull-off power, occurring ∼50-65% GC, was also reduced in powered trials. Similar to TF1, TF2 displays oscillation between positive and negative hip power at the end of prosthetic swing (∼90% GC) during passive trials, resulting in rapid hip flexion/extension (see Fig 3.4(b)). This behavior was mitigated when walking with the

Table 3.7: Average step length in mm, and Symmetry Index (SI) comparing the left and right foot during powered and passive trials.

Subject	Speed	Powered			Passive		
		Left	Right	SI	Left	Right	SI
TF1	Slow	**823.6**	**743.8**	0.102	530.9	582.2	0.092
	Normal	**843.3**	**797.6**	**0.056**	672.2	721.3	0.070
	Fast	**776.5**	**839.0**	0.077	756.1	783.5	0.036
TF2	Slow	**671.7**	**666.7**	**0.008**	599.5	656.3	0.091
	Normal	**693.8**	**715.0**	**0.030**	636.0	702.4	0.099
	Fast	**715.5**	**756.1**	**0.055**	674.9	749.3	0.104
TF3	Slow	**651.5**	**706.6**	**0.081**	608.1	669.1	0.096
	Normal	**695.8**	744.9	**0.068**	683.2	748.3	0.091
	Fast	**746.8**	**800.1**	**0.069**	718.0	790.9	0.097

powered prosthesis. The combination of these reduced hip powers results in a 17% average reduction of residual hip work when wearing the powered prosthesis, see Table 3.6.

In powered trials, TF2 displayed an increased step length for both the prosthetic and intact side, for all speeds (Table 3.7). Furthermore, the symmetry between left and right step lengths were increased for all speeds. During passive trials, TF2 displayed little hip circumduction for both the prosthetic and intact side, see Table 3.8. They did, however, present abnormal behavior during slow and fast trials, where the foot measured a negative circumduction during the swing phase. This may be caused by excessive lateral sway of the trunk or abnormal swing leg kinematics. When wearing the powered prosthesis, these trends were mitigated for the prosthetic side but resulted in an increased circumduction that was larger than healthy averages [108]. Furthermore, this increase in circumduction resulted in an increased SI.

3.5.3 Transfemoral Amputee Subject 3

Similar to the other subjects, TF3's prosthetic ankle plantarflexion returned to normative levels when wearing the powered prosthesis (Fig. 3.4(c)). Prosthetic push-off power was also

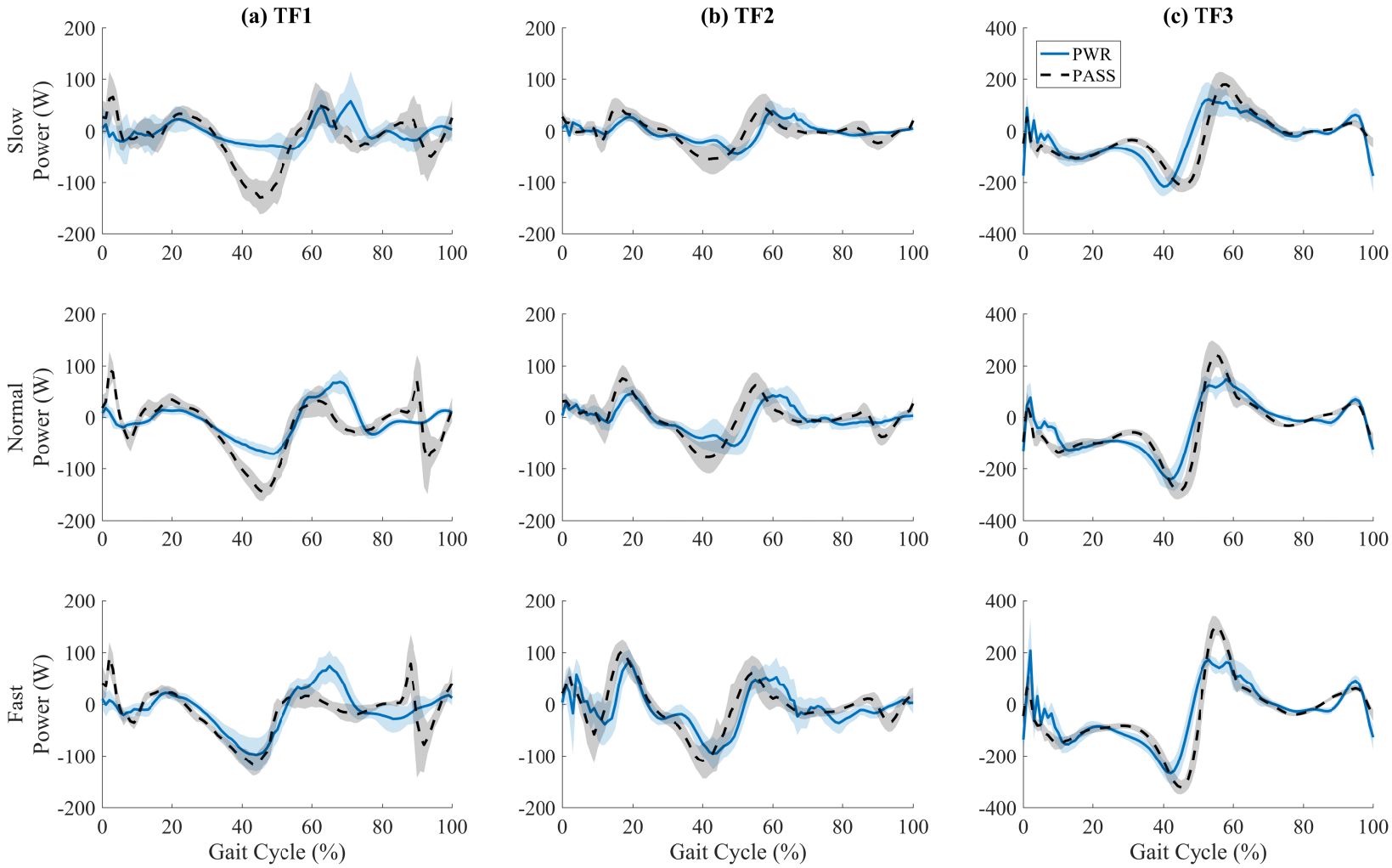

Figure 3.7: Average prosthetic side hip power throughout the gait cycle (normalized by time). Columns (a), (b), and (c) correspond to subjects TF1, TF2, and TF3, respectively. Top, middle, and bottom rows correspond to slow, normal, and fast speeds, respectively. Solid blue lines indicate average power for trials where the subject wore with the powered prosthesis (PWR), and black dashed lines indicate trials where the subject wore their personal passive prosthesis (PASS). Shaded areas around the averages indicate ±1 standard deviation.

Table 3.8: Hip circumduction defined by average lateral foot deviation in *mm*. Symmetry Index (SI) comparing the left and right foot during powered and passive trials.

Subject	Speed	Powered			Passive		
		Left	Right	*SI*	Left	Right	*SI*
TF1	Slow	**54.0**	**15.4**	1.115	68.1	27.9	0.839
	Normal	**74.1**	**8.8**	1.577	87.2	14.6	1.427
	Fast	**80.0**	**3.0**	1.857	85.0	12.6	1.484
TF2	Slow	42.8	12.7	1.086	-4.3	-2.4	0.556
	Normal	52.2	-4.3	2.357	13.0	3.1	1.238
	Fast	49.8	-9.1	2.892	-5.8	-4.6	0.222
TF3	Slow	**-9.0**	18.6	**5.776**	-20.4	16.5	18.908
	Normal	**-6.2**	22.4	**3.542**	-36.3	18.5	6.150
	Fast	**8.2**	24.5	**0.997**	-36.5	21.3	7.607

drastically increased for normal and fast speeds when wearing the powered prosthesis, see Fig. 3.5(c). At slow speeds, peak push-off power was similar to that of the passive device. TF3 displayed an increase in prosthetic propulsive impulse when wearing the powered prosthesis (Fig. 3.6(c)). This resulted in improved symmetry between propulsive and braking impulses of the prosthetic leg. Although TF3 exhibited an increased braking impulse on their intact leg, the increased prosthetic leg propulsive impulse led to improved symmetry between the two, compared to the passive trials (Table 3.5).

Similar to TF2, TF3 had a reduced peak-to-peak prosthetic-side hip power when walking with the powered prosthesis, see Fig. 3.7(c). Negative peaks at ∼45% GC were reduced at normal and fast speeds. Positive concentric pull-off powers, located at ∼50-60% GC, were drastically reduced during powered trials. The reductions in residual hip power led to a 6% average decrease in residual hip work (Table 3.6).

During powered trials, TF3 displayed an increased step length for both the prosthetic and intact side, for all speeds (Table 3.7). The only exception is at normal speed, where the intact leg had a decreased step length. However this decrease was on average only 4mm, which is negligible. Nevertheless, the step length's *SI* was decreased for all speeds,

indicating improved symmetry. During passive trials, TF3 displayed a similar abnormality to TF2, which resulted in a negative circumduction for the prosthetic leg (Table 3.8). Although this was not completely mitigated when walking on the powered prosthesis, it was greatly reduced, and even averaged positive and normative values at their fast speed [108]. The intact leg's circumduction increased, but only slightly, which resulted in improved symmetry across all speeds.

3.6 Discussion

The purpose of this case study is to determine how a powered prosthetic leg can help mitigate residual hip compensations in transfemoral amputees. A powered prosthesis with low-impedance actuators was utilized for its ability to achieve large amounts of power in phases like push-off, quickly followed by rapid dorsiflexion to provide sufficient toe clearance. Although the powered prosthesis can generate large amounts of joint power, the amount of power produced is dependent on several factors, such as control scheme, controller gains, and how the subject walks on the prosthesis. We see how this may vary when looking at the push-off ankle power produced by the powered prosthesis for our three subjects. For instance, TF1 typically preferred shorter steps, which led to premature removal of the prosthetic foot from the ground when entering the swing phase. This resulted in a push-off power similar to their passive prosthesis. TF2 and TF3, however, exploit the capabilities of the powered prosthesis to dramatically increase their prosthetic ankle push-off. Interestingly, when ankle push-off power is low, like we see in TF1's normal and fast trials, the hip compensates by increasing its concentric pull-off power ($\sim$70% GC) to accelerate the body forward. These patterns align with previous studies where this compensation is seen in transfemoral amputees when walking with passive prostheses [96, 105]. Alternatively, for trials with increased prosthetic ankle push-off power, clear reductions in concentric hip pull-off powers are evident, confirming that this hip compensation is a result of the lack of

prosthetic ankle push-off power [105]. These results imply that a powered prosthesis that can produce large ankle push-off power, followed by fast ankle dorsiflexion, can be exploited to reduce compensatory power production at the residual hip. We believe that with more extensive tuning and training trials, larger push-off power values can be provided to further minimize hip compensations.

Joint kinematics, specifically at the ankle and knee, were returned to normative levels [128]. Similar to other powered prostheses, the prosthetic ankle was able to achieve much more plantarflexion compared to the passive ankles. Powered prosthetic knee angles maintained normative levels of flexion during swing, but reduced knee hyperextension for TF2 and TF3, which is common in amputee gait to ensure knee stability. Hip range-of-motion is similar between passive and powered trials for each subject. However, deviations from normative trends are evident in TF1 and TF2 passive trials, namely in the rapid flexion and extension of the residual hip during late swing. This motion is coupled with rapid oscillation between positive and negative hip power, which is most likely caused by the lack of knee control during swing. Results with the powered prosthesis show that this compensation and power production are greatly mitigated, implying greater control of the knee during swing.

Circumduction is another compensation commonly seen in amputee gait that is deployed as a method to provide toe-clearance for the prosthetic foot. For example, when circumducting the amputee laterally deviates the prosthetic foot to prevent stubbing the toe in mid-swing. This can be caused by the lack of dorsiflexion in passive prosthetic ankles and swing control in passive knees. Powered prostheses, which can actively control the position of each joint, can help reduce this compensation. However, powered prostheses with high-impedance actuators have difficulty transitioning between large plantarflexion push-off power at the ankle and high-speed dorsiflexion to provide sufficient toe-clearance [94]. We hypothesized that the increased position and force bandwidth that is inherent to this style of actuation could reduce this compensation [25, 103]. Experimental results demonstrate that

circumduction was reduced for both the prosthetic and intact limbs for TF1 when wearing the powered prosthesis. Although circumduction was only reduced on the prosthetic side for TF3 when wearing the powered prosthesis, symmetry was drastically improved between the prosthetic and intact limb. TF2, on the other hand, displayed an increase in prosthetic circumduction when wearing the powered prosthesis. Since we see both increased and decreased circumduction and symmetry between the subjects, the results regarding circumduction show potential benefits but are somewhat inconclusive.

It is well known that stride length is commonly reduced in transfemoral amputees [125], and is described as a method of compensation for less precise leg function [99]. However, powered prostheses can aid in reducing this compensation [61]. Results with the presented powered prosthesis follow this trend: the step length of the prosthetic and intact leg were increased for almost every trial. In many cases, step length returned to normative levels (∼740-820mm) [108], improving symmetry between the prosthetic and intact side.

Across all speeds and subjects, propulsive impulses were increased when walking with the powered prosthesis. This can be attributed to two main reasons; active injection of power by the powered prosthesis and increased step length. An increased step length allows greater posterior travel of the prosthetic foot during the stance phase, which results in larger push-off power to contribute to forward propulsion. In addition to increased propulsive impulses with the powered prosthesis, all subjects displayed improved symmetry between the propulsive impulse of the prosthesis and the braking impulse of the intact leg. This is particularly important because asymmetry between these two impulses often force the hip to implement a more costly strategy to compensate for missing ankle push-off work [40], thus requiring more concentric hip work [105]. This asymmetry also indicates that the hip is compensating for the lack of propulsive impulse, but not enough to fully replace the missing ankle push-off work [110]. Therefore, we suggest that the increased impulse produced by our powered prosthesis can be a contributing factor to reduced residual hip power.

This study focuses on the effect of the powered prosthesis on prosthetic-side kinematics and kinetics. Therefore, compensations on the intact limb, such as vaulting were not heavily analyzed. It should be noted that one subject (TF1) exhibited this compensation when walking with their passive prosthesis. Preliminary analysis suggests that this compensation became worse when walking with the powered prosthesis, although this was not necessary to facilitate toe clearance. An additional investigation would be necessary to determine if this results from the amputee withdrawing to a familiar compensatory mechanism when wearing an unfamiliar device, or if the powered prosthesis exacerbates this compensation.

3.7 Conclusion

The increased power and bandwidth available with low-impedance actuators in a powered prosthesis have the potential to reduce amputee compensations at the residual hip compared to use of conventional passive prostheses. Results show that the amount of push-off power a subject receives depends on how the subject walks on the prosthesis. When correctly utilized, the powered prosthesis provided a drastic increase in ankle push-off power which resulted in reduced residual hip pull-off power. Increased push-off power, coupled with an increase in step length, resulted in an increased propulsive impulse on the prosthetic side for all subjects. All subjects displayed improved symmetry between the prosthetic propulsive impulse and the intact braking impulse, which has been linked to compensatory work at the residual hip. The combination of the reduced compensations at the hip resulted in a $\sim$13% average reduction in residual hip work per stride. By decreasing work at the residual hip, the amputee can perform the same task but at a reduced cost, which could allow for extended periods of daily ambulation and lead to improved quality of life.

Other results relating to circumduction indicate decreased values for subjects who exhibit large circumduction on their passive prosthesis, but also increased values for a subject who

typically does not circumduct. Therefore, comprehensive conclusions could not be made, but the improvements we see point to the prosthesis's potential to reduce circumduction.

Overall the prosthesis with low-impedance actuators has shown the potential to reduce several compensations for transfemoral amputee gait, particularly in residual hip power and work. Additional investigation is needed to determine whether hip circumduction can be more consistently reduced with this prosthesis when given additional training.

CHAPTER 4

DISCUSSION

4.1 Implications on the Field

The initial focus of this work is concentrated on shifting prosthetic design from high-impedance to low-impedance actuation schemes, and the impact this has on the design of lower-limb prosthetic systems. The low-impedance actuators presented in this work were designed to increase torque and power available at the prosthetic joint level, in fact, peak powers were approximately 50% greater than other state-of-art prostheses. With increased kinetic capabilities, this actuation style is adaptable and uniquely suited for a range of highly dynamic tasks. The compliant nature of the device also helps absorb abrupt interactions with the environment, which can reduce impact forces to the residual limb, prevent damage to the hardware, and simplify the design.

The low-impedance actuation scheme also demonstrated flexibility in control, facilitating a broad range of control strategies and controllable tasks. Typical torque control methods require torque feedback or lengthy tuning trials to account for unmodeled actuator dynamics. However, preliminary benchtop experiments established that the unmodeled dynamics for the presented low-impedance actuators are negligible for torques over ~10 Nm. This was also experimentally demonstrated through walking trials, where biological joint impedances were directly implemented into an impedance controller (without tuning) and achieved biologically similar kinematics and kinetics, indicating the ability to simplify torque control. The low reflected inertia and impedance of these actuators also allow a wide range of achievable joint stiffnesses, opening opportunities toward control that were previously hindered by high-impedance actuators. For instance, passive actuator dynamics can be leveraged to allow free swinging knee motion, which can lead to a more natural and efficient gait. Alternatively, high stiffness can still be implemented to facilitate precise position tracking control, as seen

in Chapter 2, which is common in prosthetic control. Moreover, this actuation scheme can quickly alternate between low and high stiffness states, another feature typically limited in other state-of-art prostheses, except those using a clutch or variable transmission. Lastly, increased power capabilities of the actuators allow for control design to focus on powerful kinetics based methods [132, 59], previously restricted by power saturation in prosthetic actuators.

Most importantly, this prosthetic design demonstrates benefits to the underlying goal and fundamental application of prosthetics, improving the quality of life of those living with a lower-limb amputation. While being capable of achieving very large joint powers, the low-impedance actuators can be characterized as highly-backdrivable. This facilitates the absorption of negative energy applied to the device by the user, and thus allowing the redistribution of regenerated energy to power other joints or to be stored in the leg's batteries. Combining this design feature with reduced friction and reflected inertia from the minimized reduction ratio, resulted in a reduced average power and energy consumption compared to other state-of-art prostheses. Reducing the energy consumption is important on the system-level, but is particularly important when considering the day-to-day use of such devices. Reducing energy consumption can lead to extended periods between charging, which can aid in clinical acceptance. Since fewer meshing components are required in the actuator's transmission, the acoustic noise is greatly reduced compared to traditional high-impedance actuation. Since loud devices bring unwanted attention to the wearer, reduced noise is specifically important in returning amputee's to normal quality of life, gaining clinical acceptance, and transferring this technology to the public. Preliminary biomechanics results demonstrate the potential for this style of actuation to reduce compensations at the residual hip. Specifically, increased ankle push-off power, combined with increased step length, reduced pull-off power at the amputee's residual hip. Through knee swing control, similar to microprocessor prosthetic knees, the presented prosthesis reduced compensatory

hip work to decelerate the shank's forward momentum. The combination of these results displayed the prosthsis's ability to reduce overall mechanical work at the residual hip, which can help reduce fatigue and increase the time an amputee ambulates daily.

4.2 Limitations and Future Work

Throughout this dissertation, limitations toward clinical acceptance of typical actuation styles have been mentioned. One of the main factors limiting clinical acceptance of the low-impedance style of actuation is its mass. Because the presented prosthesis is ∼1-2 kg heavier than state-of-art prostheses [59, 7, 95], it most likely too heavy for clinical acceptance in its current form. However, the increase in joint power available to this style of actuation can aid in offsetting the increase in prosthetic mass. Moreover, although this style of actuation requires very powerful motors, with ongoing advances in motor technology, this style of low-impedance actuation will continue to become more compact and torque dense, therefore allowing consumer devices to leverage the benefits of low-impedance actuation. As the torque density of such motors increase, the required transmission ratios will continue to decrease as well, thus simplifying or even allowing the removal of the transmission. The simplified (or removed) transmission, along with more energy-dense batteries, will aid the decrease of prosthetic mass and actuator volume. Moreover, this will most likely increase efficiency since there will be fewer losses to friction and reflected inertia. A simplified (or removed) transmission also has the potential benefit of increased bandwidth and control precision (through reduced or zero backlash). Moreover, as a result from reduced passive backdrive torque and reflected inertia of the actuators, the lower range of achievable stiffness and damping values will expand.

Although future iterations of this prosthesis will benefit from advances of motor and battery technology, it may also benefit from other design changes. For instance, as this

actuation style approaches direct drive (no transmission), a clutching mechanism may become more desirable to increase system efficiency during tasks such as standing, and prevent the knee from collapsing when the batteries are depleted. Additional design changes can further exploit the backdrivability of the actuators by implementing "force proprioception" to determine when the foot is in contact with the ground. Thus allowing the removal of the 6-axis load cell, simplifying the system's design and reducing mass.

The presented work has preliminarily shown the ability of low-impedance actuation to improve compensations at the residual hip. However, investigations on additional subjects is necessary to prove statistical significance. Furthermore, additional testing could provide insight into other compensations that may benefit from a prosthesis with low-impedance actuation.

CHAPTER 5

CONCLUSION

This dissertation began in Chapter 1 by introducing the current state of prosthetic leg design as is presented throughout the literature. Benefits and limitations were then described for each type of actuation scheme used in these devices. Motivation deriving from recent works in legged robots suggest that low-impedance actuation schemes have benefits toward legged locomotion. It was then proposed that this actuation style may have additional benefits relating specifically to prosthetic leg design.

Chapter 2 began by describing the design of custom a transfemoral prosthesis with high-torque, low-impedance actuators. Initial benchtop experiments were then conducted to characterize, test, and validate the proposed benefits to design. Simple backdrive tests confirm that the designed actuators have low mechanical impedance, which resulted in low backdrive torques required to move the motors. The open-loop impedance control test showed that the reduced reflected inertia and friction within the low-impedance actuators allows for the actuator's unmodeled dynamics to be neglected. This was further confirmed through the implementation of human walking impedances into an impedance-based walking controller, which demonstrated that accurate torque control is achievable without torque feedback or lengthy tuning trials. In addition to accurate torque control, the low-impedance actuators demonstrated the ability to accurately and precisely control joint position. In preliminary walking experiments, the low-impedance actuators also present practical design advantages through increased peak power, and reduced energy consumption and acoustic sound levels, which can aid in clinical acceptance of fully powered devices.

Although the literature suggested that the lack of prosthetic push-off power and knee control lead to compensations at the residual hip, it was not established if a powered prosthetic can aid in reducing them. After identifying this gap in the literature, the work presented in Chapter 3 focuses on investigating the effects of a powered prosthesis on compensations at

the residual hip. We proposed that a powered prosthesis with low-impedance actuators is uniquely suited to facilitate reductions in these compensations. To investigate these claims, we implemented a walking controller that exploits the impedance, time-based position, and phase-based position control abilities of the low-impedance style of actuation. This controller extends the work from Chapter 2 by combining the compliant actuation scheme with an impedance controller that uses biological joint impedances during stance to provide forceful biomimetic interactions with the ground. Time-based trajectory control harnesses the increased position bandwidth to achieve large push-off powers at the ankle during terminal stance. Phase-based trajectory control during swing synchronized the prosthesis with the user, aiding toe clearance to reduce the need for compensatory behaviors such as circumduction. This walking controller was implemented experimentally with three amputee subjects. Experimental results show that the amount of push-off power a subject receives depends on how the subject walks on the prosthesis. When correctly utilized, the powered prosthesis provided a drastic increase in ankle push-off power which resulted in reduced residual hip pull-off power. Although prosthetic push-off power at the ankle was not drastically increased for all subjects and speeds, the prosthetic propulsive impulse was. This led to an improved symmetry between the prosthetic propulsive impulse and the intact braking impulse, which is linked to compensatory work at the residual hip. Kinematic results, such as increased hip range-of-motion and step length, indicate that the powered prosthesis facilitated greater trust in the prosthesis when ambulating, compared to the passive prosthesis. The powered prosthesis also improved circumduction for subjects who typically circumduct on their passive prosthesis. The culmination of these results presents consistent improvements to average work at the residual hip when compared to walking with a passive prosthesis.

APPENDIX A

LOW-IMPEDANCE ACTUATION LEG BILL OF MATERIALS

The table below presents the Bill of Materials for the hardware dedicated to the powered prosthesis with low-impedance actuators. The table itemized each component on the prosthesis, gives a brief description of its use, its material, its mass, how it was acquired. Note that the "Part Number and Name" column lists the internal naming convention used in the CAD assembly, other manufacturer-specific information can be found in the "Material", "MPN" (Manufacturer Part Number), or "Website" columns.

Table A.1: Bill of Materials

Part Number and Name	Description	Material	Qty.	Mass (g)	MPN	Notes	Website
001-Ankle Adapter	Output of ankle 4-bar linkage	7075-T6 (SN)	1	88.00	N/A	Custom Machined	N/A
002-M3564F-SRI	Six Axis Load Cell, Extra Thin, D65mm F2500N	AISI 316	1	226.76	M3564F	Purchased	srisensor.com/188
004-Evaluation Board	Load cell evaluation board	-	1	15.00	M8122	Purchased	srisensor.com/39
005-Pacifica LP	Prosthetic foot	Carbon Fiber	1	265.03	Pacifica LP	Purchased	tinyurl.com/truen6d
006-Foot Connector-Pacifica LP and Load cell	Connects the prosthetic foot and the Ankle adpter	7075-T6 (SN)	1	28.97	N/A	Custom Machined	N/A
007-85-26 STR	Ankle Motor Stator	-	1	300.00	ILM 86x26	Purchased	tinyurl.com/we6w9rm
008-85-23 RTR	Ankle Motor Rotor	-	1	290.00	ILM 86x26	Purchased	tinyurl.com/we6w9rm
014-Ring Gear	Ankle Ring Gear	AISI 304	1	136.34	S1E10ZM10S084	Purchased	tinyurl.com/rrt2w8h
015-Sun Gear90 degAnkle	Ankle Sun Gear	AISI 304	1	4.66	S10T10M012S0508	Purchased	tinyurl.com/v5dlbgd
016-Planet Gear	Ankle Planet Gear	AISI 304	3	148.50	S10T10M054S0508	Purchased	tinyurl.com/usz8pp8
017-Transitional Gear	Ankle Transitional Gear	AISI 304	3	44.34	S10T10M018S1008	Purchased	tinyurl.com/v6bjj9f
018-Shaft	Ankle planet gear shaft	Hardened Steel	3	37.11	N/A	Custom Machined	N/A
019-ProtoCarrier_Ankle	Ankle planetary carrier	7075-T6 (SN)	1	36.63	N/A	Custom Machined	N/A
020-ProtoCarrierOut-Ankle	Ankle planetary carrier (output)	7075-T6 (SN)	1	79.36	N/A	Custom Machined	N/A
021-Carrier_Shaft_Bearing_7804K118	-	Chrome Stainless Steel	6	32.64	7804K118	Purchased	mcmaster.com/7804k118

Table A.1, continued: Bill of Materials

022-JA035XP0	Large transmission bearing	AISI 316	1	76.94	JA035XP0	Purchased	tinyurl.com/rajqyrw
023-JA040XP0	Large transmission bearing	AISI 316	1	87.20	JA040XP0	Purchased	tinyurl.com/txw3uoo
024-60355K450-BALL BEARING	-	Chrome Stainless Steel	2	30.72	60355K450	Purchased	mcmaster.com/60355k45
025-Transmission_ Standoff_95947A017	Transmission stand-offs	6061 Alloy	3	3.27	95947A017	Purchased	mcmaster.com/95947a017
026-StandoffScrew-M2.5x0.45 (5mm)-91294A012	Transmission stand-off screws	Black-Oxide Alloy Steel	6	1.44	91294A012	Purchased	mcmaster.com/91294a012
027-Shaft Key	Transmission shaft key	AISI 304	3	3.99	N/A	Custom Machined	N/A
028-Linkage	Linkages in ankle 4-bar linkage	7075-T6 (SN)	2	48.46	N/A	Custom Machined	N/A
029-Transmission Out Plate-Ankle	Holds ankle planetary carrier and bearing	7075-T6 (SN)	1	22.42	N/A	Custom Machined	N/A
030-Motor Housing	Housing that the motor stator is glued into	7075-T6 (SN)	1	114.49	N/A	Custom Machined	N/A
031-Linkage Top Spacer	-	ABS M30	2	0.09	N/A	3D Printed	N/A
032-HN 0808	Top bearing for ankle linkages	-	2	12.00	HN 0808	Purchased	tinyurl.com/smucuso
033-linkage shaft	Top shaft for linkages	7075-T6 (SN)	2	4.30	N/A	Custom Machined	N/A
034-Ankle Shaft	Shaft resembling ankle axis of rotation	7075-T6 (SN)	1	9.68	N/A	Custom Machined	N/A

Table A.1, continued: Bill of Materials

035-Shoulder_Bolt_Ankle_91259A174	-	7075-T6 (SN)	1	9.68	91259A174	Purchased	mcmaster.com/91259a174
036-Ankle_Linkage_Bearing_5972K225	-	Chrome Stainless Steel	4	41.44	5972K225	Purchased	mcmaster.com/5972k225
037-Lower Linkage Shaft	Lower shaft for linkages in 4-bar linkage	7075-T6 (SN)	2	4.51	N/A	Custom Machined	N/A
038-LinkageSetScrew-M4x0.7 (6mm)-92775A116	-	-	2	0.70	92775A116	Purchased	mcmaster.com/92775a116
041-Linkage Spacer 1	-	ABS M30	1	0.02	N/A	3D Printed	N/A
042-Linkage Spacer 2	-	ABS M30	1	0.02	N/A	3D Printed	N/A
043-Rotor Shaft Connection	Ankle rotor shaft. Motor rotor magnets and sun gear are glued to this	7075-T6 (SN)	1	55.96	N/A	Custom Machined	N/A
044-AnkleMotorHousing Screw-M4x0.7 (12mm)-93070A103	-	Alloy Steel	3	4.95	93070A103	Purchased	mcmaster.com/93070a103
045-M4x0.7 (8mm)-93070A098	-	Alloy Steel	15	20.10	93070A098	Purchased	mcmaster.com/93070a098
046-SOCKET HEAD CAP SCREW-93070A121	-	Alloy Steel	5	12.95	93070A121	Purchased	mcmaster.com/93070a121
047-Ankle Shaft Spacer	-	ABS M30	2	0.14	N/A	3D Printed	N/A
048-Upper_Hinge_Pins_91595A155	-	Alloy Steel	6	6.24	91595A155	Purchased	mcmaster.com/91595a155
049-Lower Pylon Dowel Pin-91595A150	-	Alloy Steel	2	1.34	91595A150	Purchased	mcmaster.com/91595a155

Table A.1, continued: Bill of Materials

050-Load Cell Pins-91595A104	-	Alloy Steel	4	1.56	91595A104	Purchased	mcmaster.com/91595a104
051-Foot_Adapter_Screw_93070A125	-	Alloy Steel	6	18.72	93070A125	Purchased	mcmaster.com/93070a125
053-Ball Bearing Wide-60355K450	-	Alloy Steel	2	30.72	60355K450	Purchased	mcmaster.com/60355k45
054-Backbone ankle Left	Ankle structure	7075-T6 (SN)	1	97.22	N/A	Custom Machined	N/A
055-Twitter Solo	Motor driver, R80A/80VDC CAN232 ENC 5VL Wires	-	2	112.00	G-SOLTWIR 80/80SE2	Purchased	tinyurl.com/sft46df
056-Foot Adapter Screw-93070A105	-	Alloy Steel	1	1.96	93070A105	Purchased	mcmaster.com/93070a105
057-HingeLowerRight	Knee structure	7075-T6 (SN)	1	42.12	N/A	Custom Machined	N/A
058-HingeLowerBack	Knee structure	7075-T6 (SN)	1	15.72	N/A	Custom Machined	N/A
059-HingeLowerFront	Knee structure	7075-T6 (SN)	1	23.72	N/A	Custom Machined	N/A
060-HingeLowerBottom	Knee structure	7075-T6 (SN)	1	76.96	N/A	Custom Machined	N/A
061-HingeLowerLeft	Knee structure	7075-T6 (SN)	1	43.63	N/A	Custom Machined	N/A
062-M3Dowel (16mm)_91595A116	-	7075-T6 (SN)	2	1.70	91595A116	Purchased	mcmaster.com/91595a116
063-M4Dowel (12mm)_91595A155	-	Chrome Stainless Steel	8	8.88	91595A155	Purchased	mcmaster.com/91595a155

Table A.1, continued: Bill of Materials

064-M4 x0.7 (16mm)-93070A105	-	Chrome Stainless Steel	13	25.48	93070A105	Purchased	mcmaster.com/93070a105
065-M5Dowel (12mm)-91595A344	-	Chrome Stainless Steel	8	13.68	91595A344	Purchased	mcmaster.com/91595a344
066-EncoderSpacer	-	ABS M30	1	1.88	N/A	3D Printed	N/A
067-Bearing-60355K450	-	Alloy Steel	5	76.80	60355K450	Purchased	mcmaster.com/60355k45
068-M3PressInNuts-94100a110	-	Chrome Stainless Steel	2	0.64	94100a110	Purchased	mcmaster.com/94100a110
069-HingeUpperRight	Knee structure	7075-T6 (SN)	1	64.99	N/A	Custom Machined	N/A
070-HingeUpperTop	Knee structure	7075-T6 (SN)	1	66.38	N/A	Custom Machined	N/A
071-HingUpperFront	Knee structure	7075-T6 (SN)	1	22.23	N/A	Custom Machined	N/A
072-HingeUpperBack	Knee structure	7075-T6 (SN)	1	14.47	N/A	Custom Machined	N/A
073-HingeUpperLeft	Knee structure	7075-T6 (SN)	1	50.72	N/A	Custom Machined	N/A
074-M3Dowel (16mm)-91595A116	-	Alloy Steel	2	1.70	91595A116	Purchased	mcmaster.com/91595a116
075-RingGear	Knee Ring Gear	AISI 304	1	129.04	S1E10ZM10S084	Purchased	tinyurl.com/rrt2w8h
076-SunGear(90deg)	Knee Sun Gear	AISI 304	1	4.66	S10T10M012S0508	Purchased	tinyurl.com/v5dlbg
077-PlanetGear	Knee Planet Gear	AISI 304	3	148.50	S10T10M054S0508	Purchased	tinyurl.com/usz8pp8
078-TransitionalGear	Knee Transitional Gear	AISI 304	3	44.13	S10T10M018S1008	Purchased	tinyurl.com/v6bjj9f
079-Shaft	Knee planet gear shaft	Hardened 17-4 PH Stainless Steel	3	37.11	N/A	Custom Machined	N/A

Table A.1, continued: Bill of Materials

080-ProtoCarrier	Knee planetary carrier	7075-T6 (SN)	1	46.62	N/A	Custom Machined	N/A
081-CarrierShaft Bearing-7804K118	-	Chrome Stainless Steel	6	32.64	7804K118	Purchased	mcmaster.com/7804k118
082-JA035XP0	Large transmission bearing	AISI 316	1	76.94	JA035XP0	Purchased	tinyurl.com/rajqyrw
083-JA040XP0	Large transmission bearing	AISI 316	1	87.20	JA040XP0	Purchased	tinyurl.com/txw3uoo
084-MotorOutputShaft	Knee rotor shaft. Motor rotor magnets and sun gear are glued to this	7075-T6 (SN)	1	19.42	N/A	Custom Machined	N/A
085-Transmission Standoff-95947A017	Transmission stand-offs	6061 Alloy	3	3.27	95947A017	Purchased	mcmaster.com/95947a017
086-M2.5x0.45 (5mm)-91294a012	-	Black-Oxide Alloy Steel	6	1.44	91294a012	Purchased	mcmaster.com/91294a012
087-Shaft Key	Transmission shaft key	AISI 304	3	3.99	N/A	Custom Machined	N/A
088-ProtoCarrierOut	Knee planetary carrier (output)	7075-T6 (SN)	1	75.52	N/A	Custom Machined	N/A
089-Encoder	Motor encoders, 4096CPR, fits 0.25" shaft diameter	-	2	30.00	E5-4096-250-IE-D-D-D-B	Purchased	tinyurl.com/sw37f5k
090-Backbone Standoff	-	ABS M30	2	0.70	N/A	3D Printed	N/A
091-Ankle Hard Stop Outer (Flexible)	Bumper to prevent loud impacts with hardstop	TPU 95A	1	2.29	N/A	3D Printed	N/A

Table A.1, continued: Bill of Materials

092-Ankle Hard Stop Inner (Rigid)	Bbumper to prevent loud impacts with hardstop	ABS M30	1	0.03	N/A	3D Printed	N/A
093-Ring Gear Mount Plate	Ankle structure. Holds planetary carrier and ring gear	7075-T6 (SN)	1	105.69	N/A	Custom Machined	N/A
094-Ankle Pylon Lower	Ankle structure, attachted pylon to ankle	7075-T6 (SN)	1	57.17	N/A	Custom Machined	N/A
095-Ankle Protocarrier Washer	-	ABS M30	2	0.14	N/A	3D Printed	N/A
096-Ankle Linkage washer	-	ABS M30	2	0.18	N/A	3D Printed	N/A
097-Ankle Rotor Brace	Holds ankle motor rotor bearing	7075-T6 (SN)	1	23.03	N/A	Custom Machined	N/A
098-Shoulder Bolt-92981A141	-	Alloy Steel	2	2.62	92981A141	Purchased	mcmaster.com/92981a141
099-PyramidAdapter	-	Titanium	1	105.38	4R23	Purchased	tinyurl.com/vczeqfq
100-(85-26 STR_1)	Knee Motor Stator	-	1	300.00	ILM 86x26	Purchased	tinyurl.com/we6w9rm
101-(85-23 RTR)	Knee Motor Rotor	-	1	290.00	ILM 86x26	Purchased	tinyurl.com/we6w9rm
104-Knee Motor Output Shaft	Knee motor rotor shaft	7075-T6 (SN)	1	18.16	N/A	Custom Machined	N/A
105-Rotor Shaft Connection	Knee motor rotor shaft	7075-T6 (SN)	1	37.18	N/A	Custom Machined	N/A
106-Knee Motor Housing	Housing that the motor stator is glued into	7075-T6 (SN)	1	95.37	N/A	Custom Machined	N/A
107-Knee Motor Bearing Housing	Holds knee motor rotor bearing	6061 Alloy	1	62.20	N/A	Custom Machined	N/A

Table A.1, continued: Bill of Materials

108-Bearing (.5 in Shaft)-2342K186	-	Chrome Stainless Steel	1	26.93	2342K186	Purchased	mcmaster.com/2342k186
109-Knee Motor Bearing Housing Bearing Spacer	-	6061 Alloy	1	0.70	N/A	Custom Machined	N/A
110-Housing_Spacer_91877A121	Rename to remove mcmaster number	ABS M30	2	0.22	N/A	3D Printed	N/A
111-Motor Shaft Spacer Out	-	ABS M30	1	0.08	N/A	3D Printed	N/A
112-Motor Front Plate	Knee structure	7075-T6 (SN)	1	23.80	N/A	Custom Machined	N/A
121-Ring Gear Mount Plate	Knee structure	7075-T6 (SN)	1	60.49	N/A	Custom Machined	N/A
122-UpperBumper-SoftTop	Knee bumper to prevent loud impacts with hardstop	TPU 95A	1	0.79	N/A	3D Printed	N/A
123-UpperBumper-RigidBase	Knee bumper to prevent loud impacts with hardstop	TPU 95A	1	0.89	N/A	3D Printed	N/A
124-LowerBumper-SoftTop	Knee bumper to prevent loud impacts with hardstop	TPU 95A	1	0.80	N/A	3D Printed	N/A
125-LowerBumper-RigidBase	Knee bumper to prevent loud impacts with hardstop	TPU 95A	1	0.89	N/A	3D Printed	N/A
126-BackLowerBumper	Knee bumper to prevent loud impacts with hardstop	TPU 95A	1	2.99	N/A	3D Printed	N/A

Table A.1, continued: Bill of Materials

127-BackUpperBumper	Knee bumper to prevent loud impacts with hardstop	TPU 95A	1	3.08	N/A	3D Printed	N/A
131-M3x0.5 (5mm)_ 93395A197	-	Chrome Stainless Steel	4	1.40	93395A197	Purchased	mcmaster.com/93395a197
133-Knee Output Shaft Spacer	-	ABS M30	1	0.34	N/A	3D Printed	N/A
134-M3x0.5 (14mm)- 91294A133	-	Chrome Stainless Steel	2	1.50	91294A133	Purchased	mcmaster.com/91294a133
135-Encoder Cover	Cover to protect optical encoders	ABS M30	1	5.18	N/A	3D Printed	N/A
136-Pylon	Pylon connecting the knee and ankle actuators	Carbon Fiber	1	22.24	-	Purchased	
137-Shoulder Screw-92012A572	-	Chrome Stainless Steel	2	9.76	92012A572	Purchased	mcmaster.com/92012a572
138-Sholder Bolt- 94035A125	-	Chrome Stainless Steel	1	1.34	94035A125	Purchased	mcmaster.com/94035a125
139-Ankle Rotor Brace Cover	Protects motor and routes wires	ABS M30	1	27.64	N/A	3D Printed	N/A
140-M2 Press in Nuts- 94100A150	-	Chrome Stainless Steel	3	1.08	94100A150	Purchased	mcmaster.com/94100a150
141-Wire Cover left	Encloses wire routing	ABS M30	1	1.63	N/A	3D Printed	N/A
142-Wire Cover Right	Encloses wire routing	ABS M30	1	1.63	N/A	3D Printed	N/A
143-Backbone Spacer	-	ABS M30	1	2.34	N/A	3D Printed	N/A
145-IMU Nest	Holds IMU on thigh	ABS M30	1	20.72	N/A	3D Printed	N/A
146-IMU Nest Lid	Encloses IMU Nest	ABS M30	1	4.55	N/A	3D Printed	N/A

Table A.1, continued: Bill of Materials

147-Lord Microstrain IMU	IMU for measuring thigh angle	-	1	13.00	3DM-CX5-25	Purchased	tinyurl.com/rojb2yq
148-Thigh IMU PCB	Used to mount thigh IMU	-	1	7.00	N/A	Custom PCB	oshpark.com
149-myRIO 1900	Microcontroller/Computer	-	1	103.00	1900	Purchased	tinyurl.com/qq628y9
150-Battey Alarm	Battery alarms to prevent excess battery drainage	-	4	40.00	1655	Purchased	tinyurl.com/sfesmw3
151-Battery PCB	Connects batteries in series	-	1	25.00	N/A	Custom PCB	oshpark.com
152-LiPo Battery	Batteries used	-	4	316.00	TP870-3SR70	Purchased	tinyurl.com/thexatb
153-Battery Case	Holds the leg's batteries	ABS M30	1	75.65	N/A	3D Printed	N/A
154-myRIO mount	Holds the leg's computer	ABS M30	1	58.01	N/A	3D Printed	N/A
155-Knee Consolidation PCB	Consolidates knee electronic signals and sends to the Main PCB	-	1	12.00	N/A	Custom PCB	oshpark.com
156-Ankle Consolidation PCB	Consolidates knee electronic signals and sends to the Main PCB	-	1	12.00	N/A	Custom PCB	oshpark.com
157-PCBNestBase-Left	Holds knee motor driver and consolidation PCB	ABS M30	1	9.86	N/A	3D Printed	N/A
158-PCBNestBase-Right	Holds knee motor driver and consolidation PCB	ABS M30	1	9.61	N/A	3D Printed	N/A
159-Main PCB (PCB Prototype)	Performs signal processing before sending to myRIO	-	2	66.00	N/A	Custom PCB	oshpark.com
160-Inner Clamp	Holds the leg's computer	ABS M30	1	4.55	N/A	3D Printed	N/A

Table A.1, continued: Bill of Materials

161-Battery Alarm Cover	Covers battery alarms	ABS M30	2	18.06	N/A	3D Printed	N/A
162-Twitter Solo Heatsink	Heatsink for knee motor driver	7075-T6 (SN)	1	24.60	N/A	Custom Machined	N/A

APPENDIX B

OVERVIEW OF LABVIEW CODE

The code that runs the powered prosthesis is written in the LabVIEW environment. The file format that LabVIEW uses is called a "Virtual Instrument" or "VI". Each VI can contain sub-VIs that act as sub-functions. The powered prosthesis's highest level VI is called the "Main", seen in Figures B.1 and B.2. As you can see in Figure B.2, the Main VI uses a "Flat Sequence Structure" and breakes the code into 7 frames; Load, Initialize, Acquire and process data, Write data to files, Save Current Values, Close, and Stop. "Load" and "Initialize" frames execute commands and sub-VIs needed at startup, which only need to execute once per run. The "Acquire and Process Data" contains the bulk of the code, including the two main loops ("Serial Loop" and "Main Loop") that run the prosthesis in real-time. The "Serial Loop" executes tasks relating to serial communication (IMUs and load cell). The "Main Loop" contains all other required tasks for the real-time operation of the prosthesis. The "Write Data to File" frame contains VIs to save prosthetic data to .dat files. The "Save Current Values" frame houses code to save front panel parameters for subsequent executions of the "Load" frame. Lastly, the "Close" and "Stop" frames complete and end the execution of the LabVIEW code. Additional details relating to specific sub-VIs and LabVIEW elements are presented in Tables B.1 and B.2, respectively.

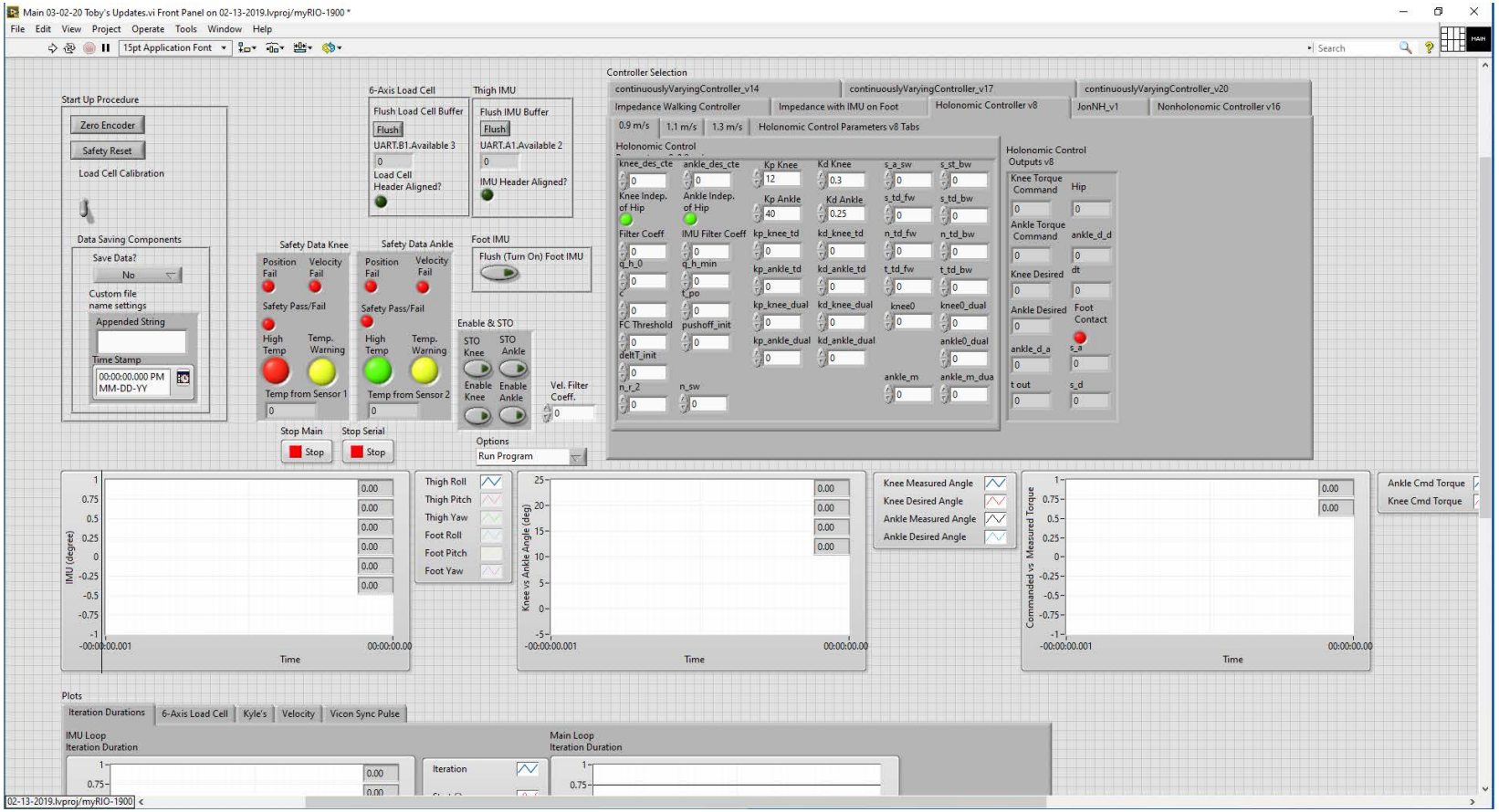

Figure B.1: Screenshot of the Main VI's front panel, acting at the user interface. This is where you can update parameters and monitor sensor measurements in real-time.

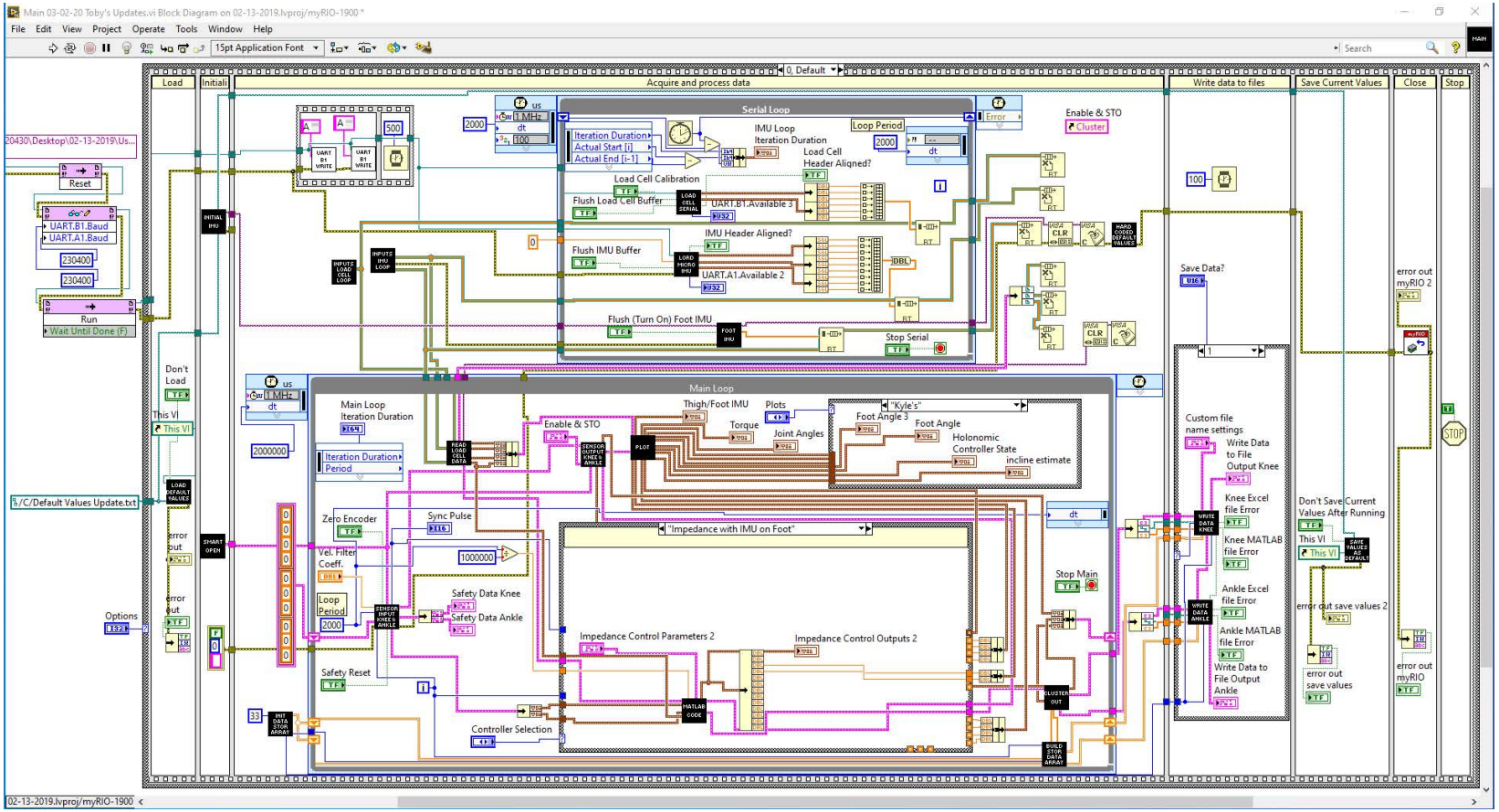

Figure B.2: Screenshot of the Main VI's block diagram, which contains the actual code running the prosthesis.

Table B.1: Information on specific sub-VIs within the Main VI

sub-VI	Location	Description
LOAD DEFAULT VALUES	Main	Loads the front panel values from the .txt file saved from the "Save Values as Default" VI.
SMART OPEN	Main	Initializes and opens the built-in LabVIEW drivers used to read the IO pins. Only needs to run once per start-up of the "Main".
SENSOR INPUT KNEE & ANKLE	Main	Contains knee and ankle subVIs that read/call sensor IOs.
SENSOR OUTPUT KNEE & ANKLE	Main	Consolidates data from the controllers. Converts torque commands to voltage levels. Sends torque commands (volts), STO, and Enable signals to knee and ankle motor drivers.
LOAD CELL SERIAL	Main	Reads and assembles data packets from the 6-axis load cell.
LORD MICRO IMU	Main	Reads and assembles data packets from the thigh's interial measurement unit (IMU).
FOOT IMU	Main	Reads and assembles data packets from the foot's interial measurement unit (IMU).
INIT DATA STOR ARRAY	Main	Initializes an array of a fixed size for subsequent loop iterations to fill with data.
BUILD STOR DATA ARRAY	Main	Stores controller variables within the pre-defined array initialized by "Init Data Stor Array".
WRITE DATA KNEE	Main	Takes the populated array exported from "Build Stor Data Array" and writes to a .dat file.
WRITE DATA ANKLE	Main	Takes the populated array exported from "Build Stor Data Array" and writes to a .dat file.
KNEE SENSOR INPUT	Sensor Input Knee & Ankle	Contains VIs that read the knee actuator's temperature sensors and encoders, and calculates motor velocities .
ANKLE SENSOR INPUT	Sensor Input Knee & Ankle	Contains VIs that read the ankle actuator's temperature sensors and encoders, and calculates motor velocities.
KNEE SAFETY	Sensor Input Knee	Sets safety limits for joint angle and velocity. When safety limits are exceeded, the motor are disabled.

Table B.1, continued: Information on specific sub-VIs within the Main VI

ANKLE SAFETY	Sensor Input Ankle	Sets safety limits for joint angle and velocity. When safety limits are exceeded, the motor are disabled.
KNEE JOINT ANGLE VEL	Sensor Input Knee	Reads knee motor encoder and converts counts to degrees. Uses point-by-point derivative to calculate motor velocity.
ANKLE JOINT ANGLE VEL	Sensor Input Ankle	Reads ankle motor encoder and converts counts to degrees. Uses point-by-point derivative to calculate motor velocity.
TEMP SENSOR	Ankle (Knee) Sensor Input	Reads motor thermistor and calculates corresponding temperature.
MATLAB CODE	Main	Contains all code for executing an individual's matlab controller, including inputs, outputs, and shared object file (.so).

Table B.2: Information on general LabVIEW elements within the Main VI

Element	Location	Description
Serial Loop	Main VI Block Diagram	Executes tasks relating to serial communication for the thigh IMU, foot IMU, and 6-axis load cell.
Main Loop	Main VI Block Diagram	Contains and executes the majority required tasks for real-time operation of the prosthesis, including defining front panel objects, sensor reading, data collection, and controller implementation.
Controller Case Structure	Main Loop	Contains sub-diagrams that contain the different "Matlab Code" VIs.
Controller Selection Tabs	Main VI Front Panel	Front panel interface for selecting specific cases within the "Controller Case Structure". Provides a compact location to store inputs and outputs for individual controllers.
Zero Encoders	Main VI Front Panel	Button that sets the encoders current value to zero.
Safety Reset	Main VI Front Panel	Button that unlatches the internal switching logic that engages when the prosthesis exceeds a safety limit.

Table B.2, continued:Information on general LabVIEW elements within the Main VI

Plotting Case Structure	Main Loop	Used to house several plotting elements and reduce block diagram space.
Plots Tabs	Main VI Front Panel	Tabs that selects "Plotting Case Structure" cases, and therefore which plots to view.
Data Saving Components	Main VI Front Panel	Contains Logic for saving or non-saving modes, and options for appending custom text or timestamps to file names. Entries to these elements are sent to the "Write Data Knee" and "Write Data Ankle" sub-VIs.
Thigh IMU Front Panel Elements	Main VI Front Panel	Contains number of bytes available in IMU buffer, tells if IMU packet header is aligned, and provides button to flush IMU buffer.
Foot IMU Front Panel Elements	Main VI Front Panel	Provides button to turn on and off the foot IMU.
6-Axis Load Cell Front Panel Elements	Main VI Front Panel	Contains number of bytes available in load cell buffer, tells if load cell packet header is aligned, provides button to flush load cell buffer, and switch to calibrate the load cell.
Enable & STO Elements	Main VI Front Panel	Contains LED buttons to send Enable and STO signals to both the knee and ankle motor drivers. Fora a given actuator, turn on STO first, then Enable.
Safety Data Knee/Ankle Elements	Main VI Front Panel	Contains LEDs that indicate if a safety has been tripped, and which safety limit is currently tripped.
Stop Main	Main VI Front Panel	Button that halts the execution of the "Main Loop".
Stop Serial	Main VI Front Panel	Button that halts the execution of the "Serial Loop".

APPENDIX C

EXECUTING MATLAB SCRIPTS IN THE LABVIEW ENVIRONMENT

C.1 Create the MATLAB code and test bench

Open MATLAB and set the working directory to the folder which contains your controller and test bench (both of which are written in MATLAB as a .m files). Follow the the general structure outlined below when setting up your code.

MATLAB code:

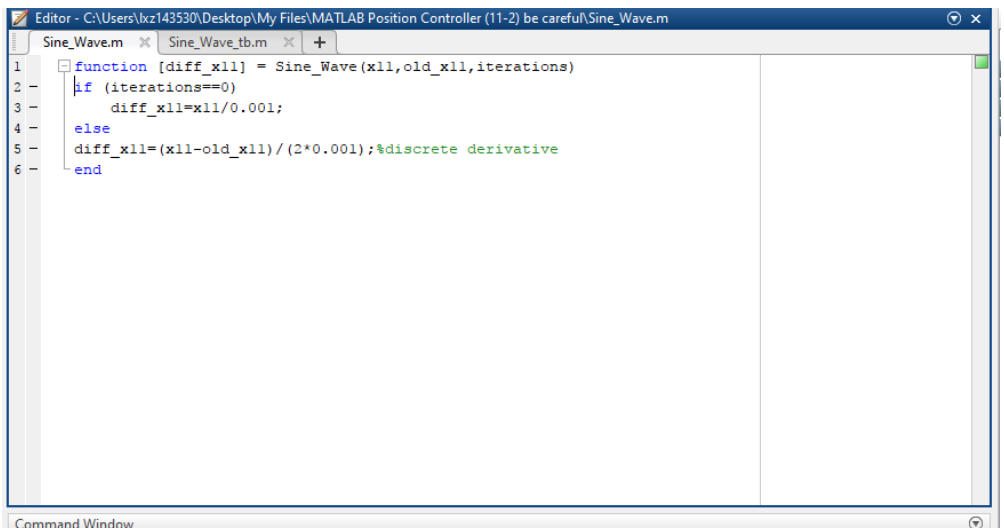

Format for function: function [output 1, output 2, . . .] = name [input1, input2, . . .];

Test bench:

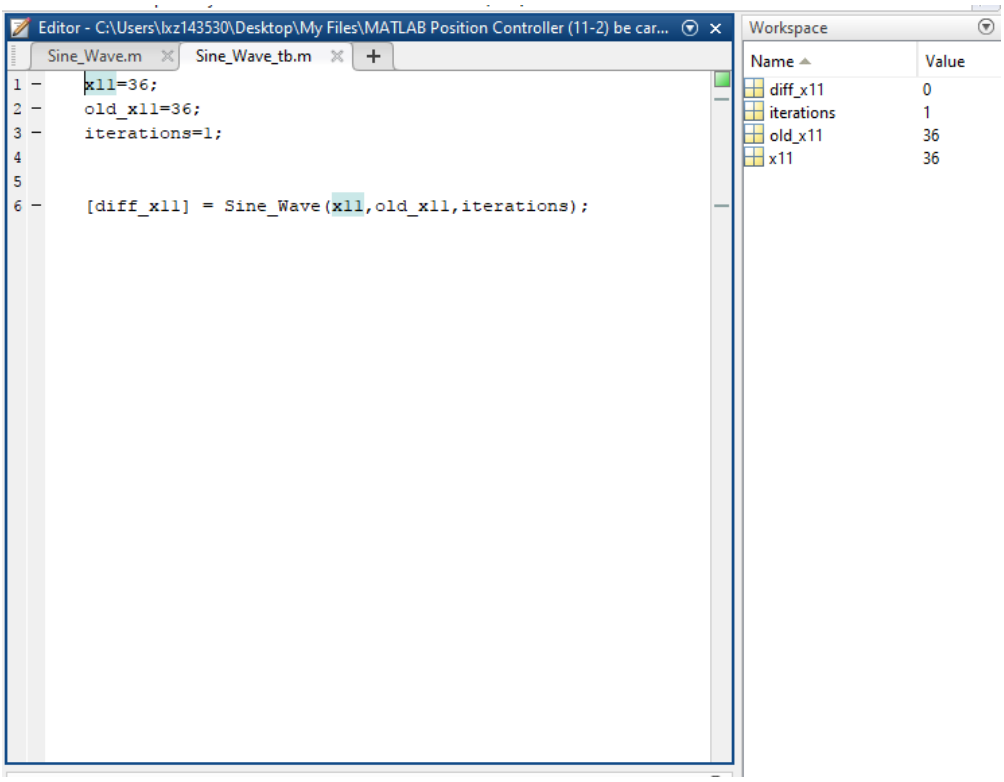

Initialize inputs (these can be chosen arbitrarily as they have no effect on output when this code runs on LabVIEW). After initialization of inputs, call the function.

C.2 Convert MATLAB code to C using MATLAB coder

a) To convert from MATLAB to C open the MATLAB Coder under the APPS tab.

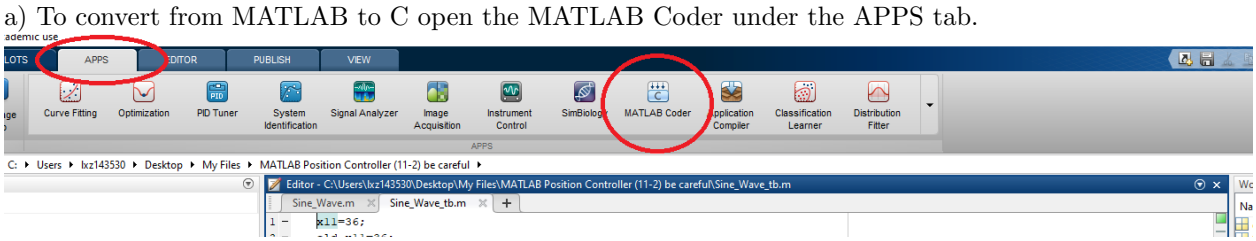

b) Beside “Numeric Conversion” select “Convert to Single Precision” from the drop down menu. Then click “. . .” and find the .m file for MATLAB code (not test bench) then click next.

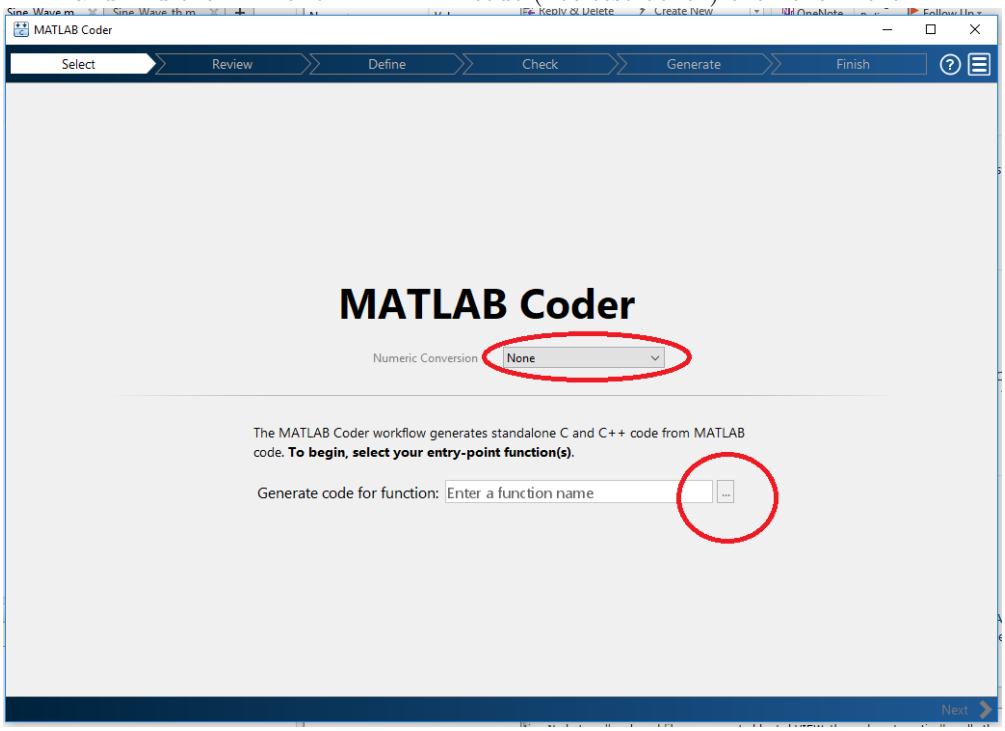

If the notification shown below appears after selecting the desired .m file, click “Overwrite”.

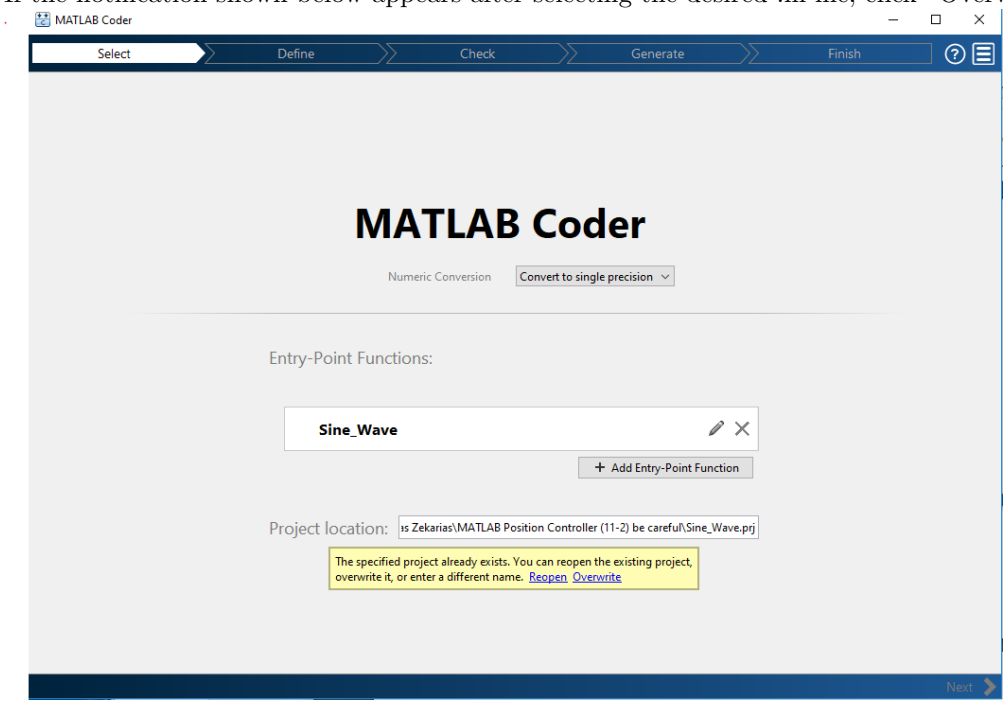

c) Select "..." and find the test bench .m file then, select "Autodefine Input Types". Once the input types are defined, click next.

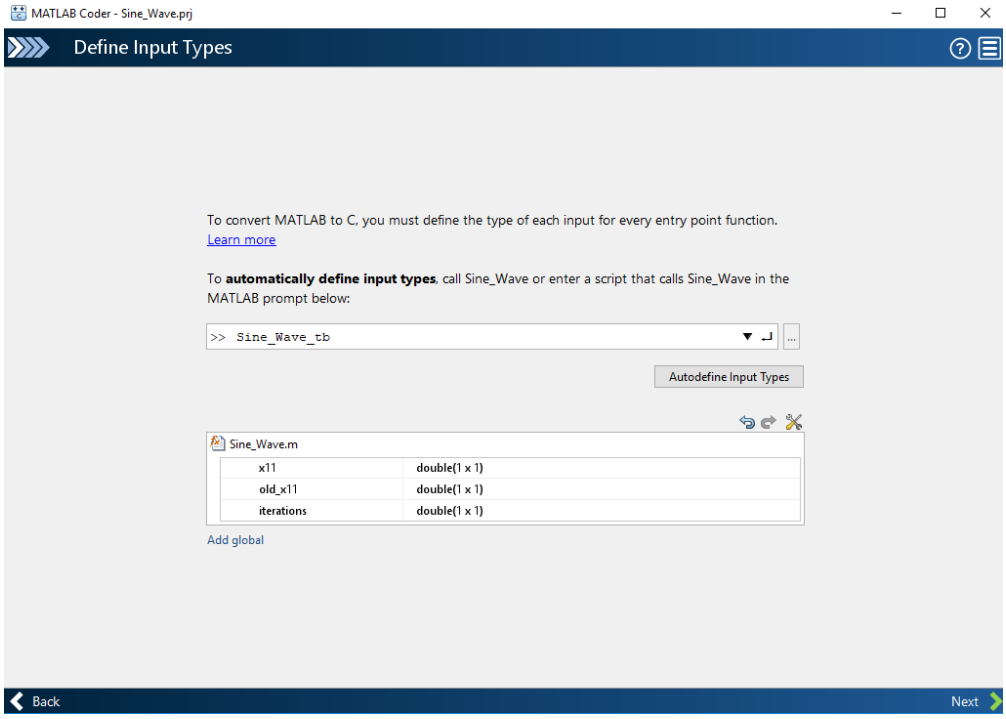

d) Select "Check for Issues", once it is done click next. It should look like this once it is done.

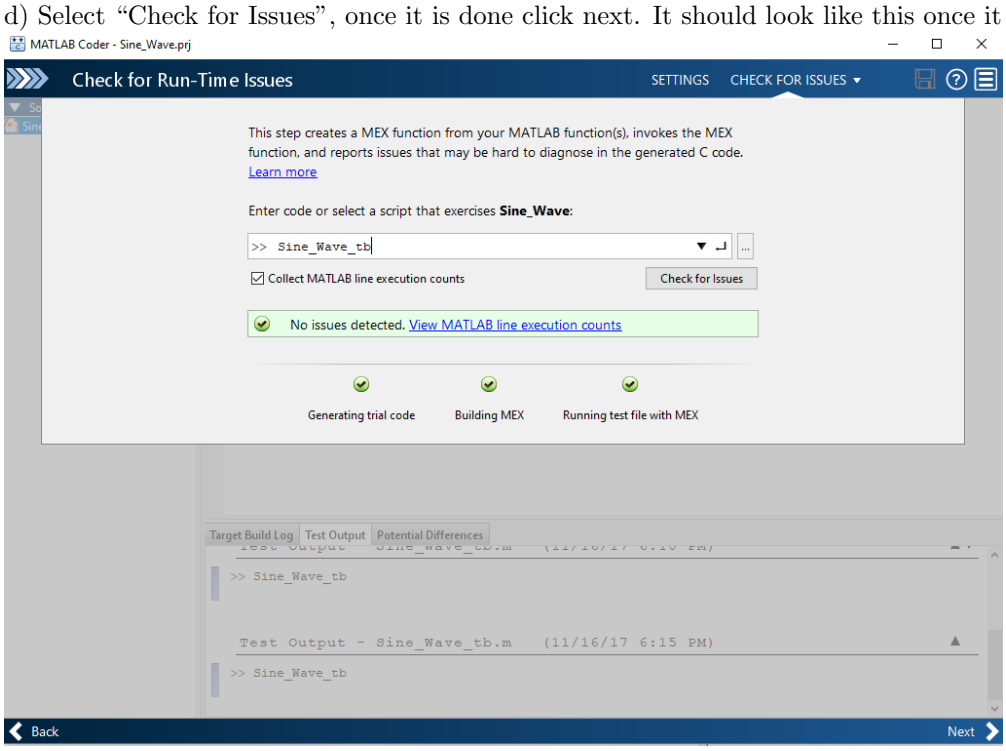

e) Click “Generate”, once the C source code is successfully generated a notification stating “Source Code generation succeeded” on the bottom of the page will appear. After that click next.

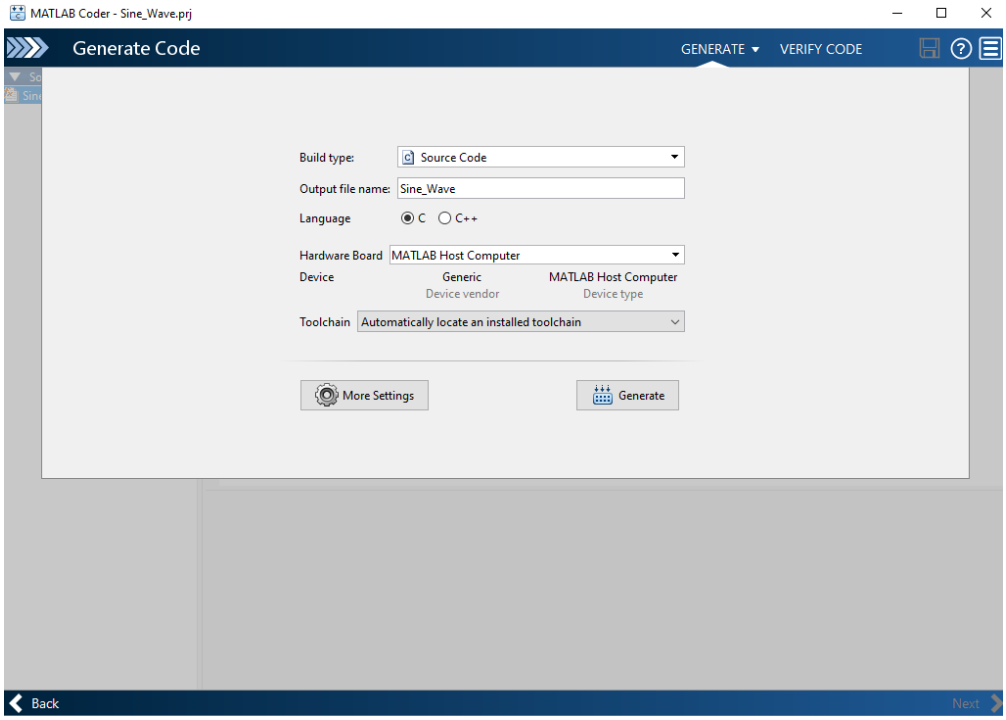

To find where the relevant .c and .h files are located click on the “C Code” folder location. These files are required to build the Shared Object (next step) so, do not close this window.

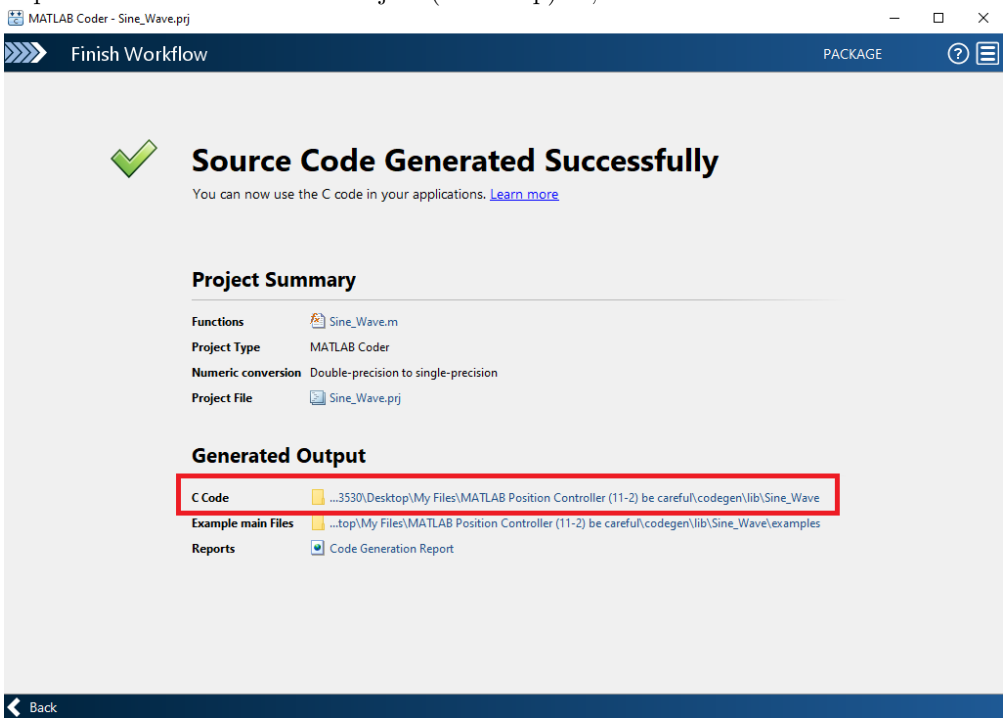

C.3 Building the Shared Object

This step will convert the C code to a Shared Object

a) Launch C & C++ Development Tools for NI Linux Real-Time 2014, Eclipse Edition.

b) Once the program is open, this window will pop up. By default the "Workspace Launcher" will select the workspace folder under the user's netID. Click "OK" once the desired workspace folder is selected.

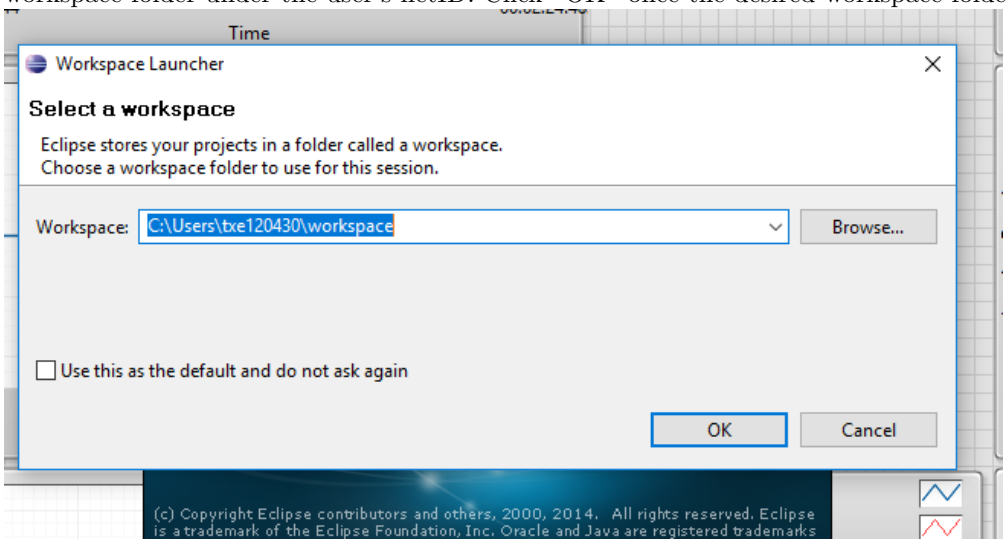

c) Look at the top right and make sure "C/C++" is selected then go to File→ New→ C Project.

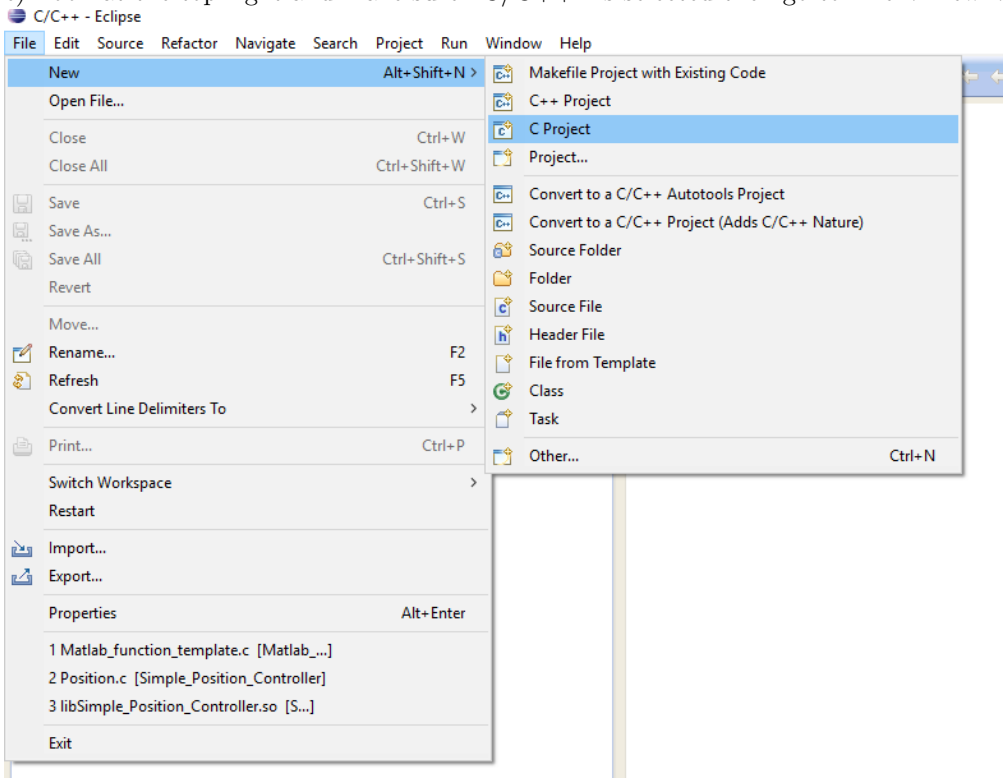

d) Enter the desired Project name and select Shared Library→ Empty Project, then click next.

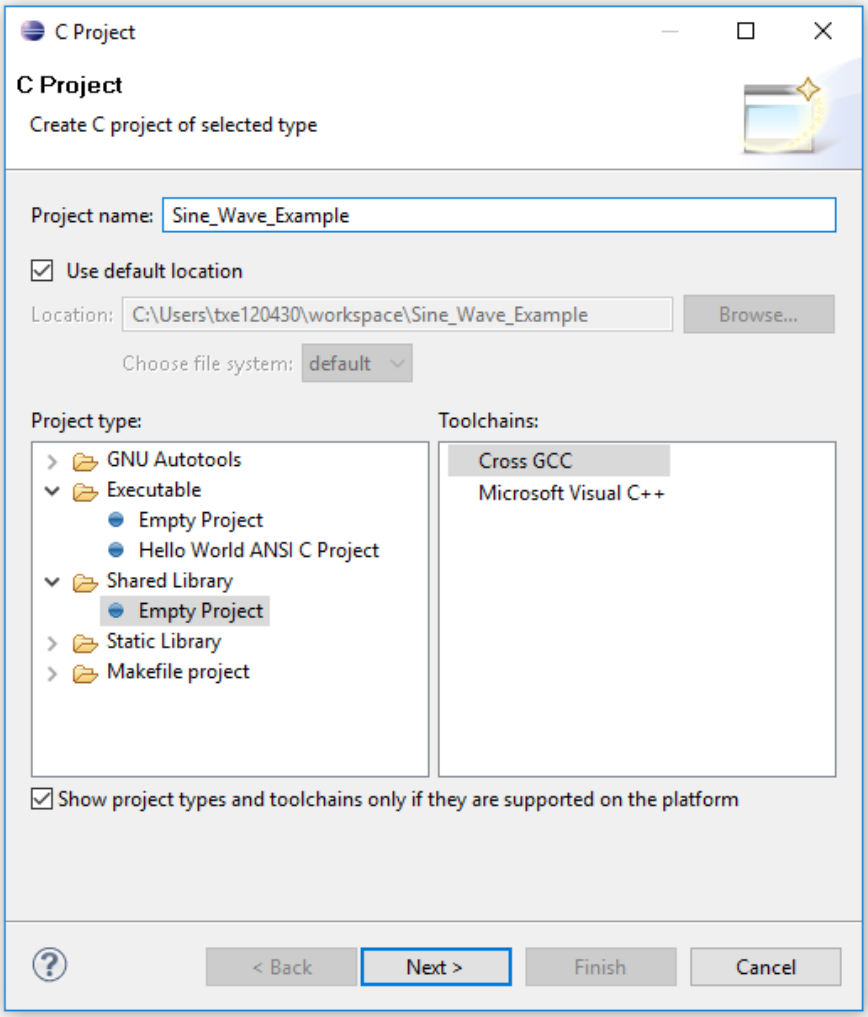

There is nothing that needs to be altered on the "Select Configurations" window so, click next again

e) Under “Cross complier prefix” enter: arm-nilrt-linux-gnueabi- Under “Cross complier path” enter: C:\Program Files (x86)\National Instruments\Eclipse\14.0\arm\sysroots\i686-nilrtsdk-mingw32\usr\bin\armv7a-vfp-neon-nilrt-linux-gnueabi

Note that these should be default.

Then click finish.

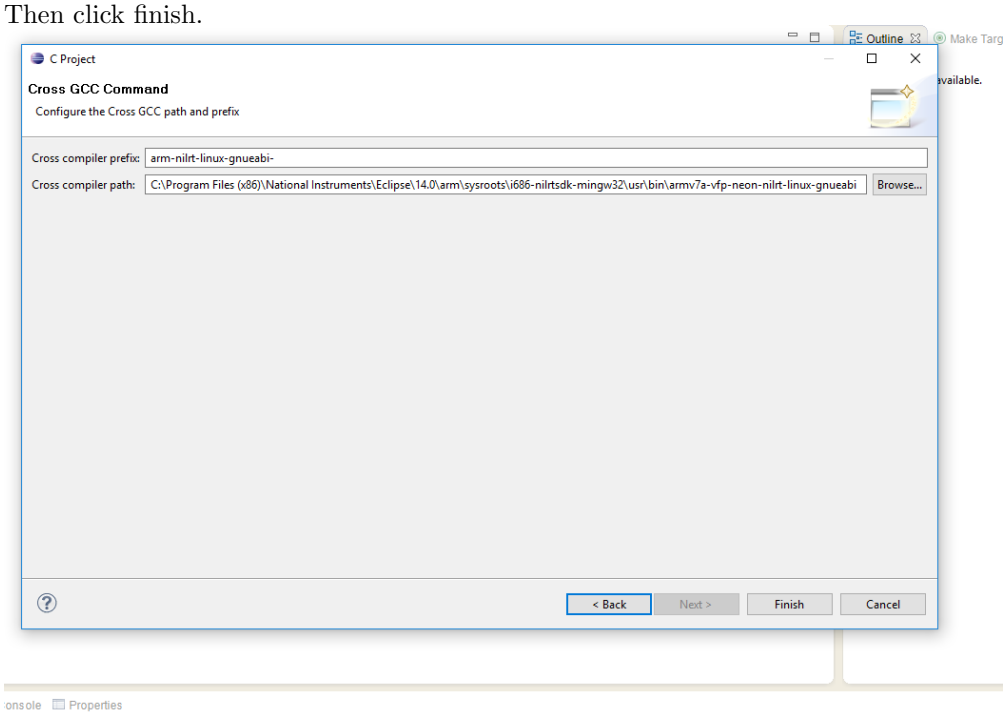

f) Now right click the project folder under “Project Explorer” and click on “Properties”.

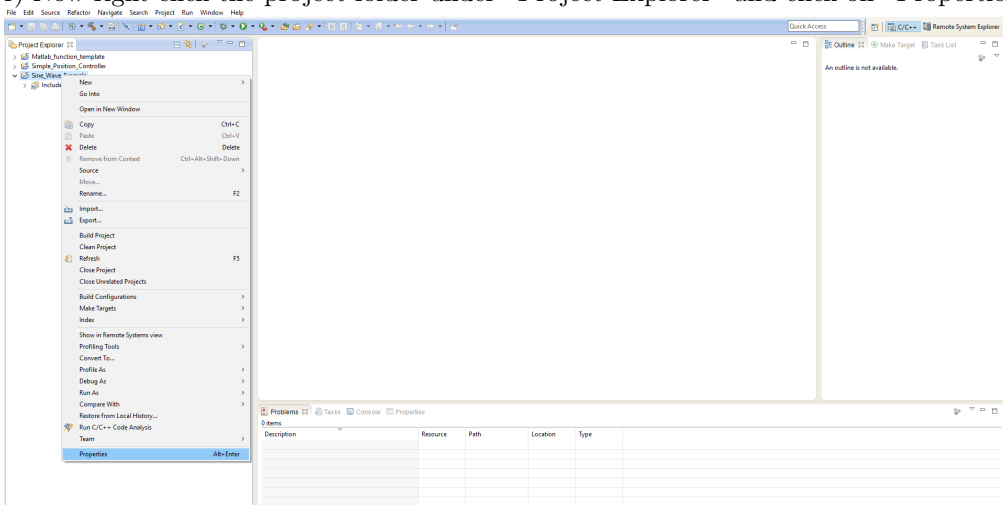

g) Select C/C++ Build, then select the Builder Settings tab and change the “Builder type” to Internal Builder, then click apply.

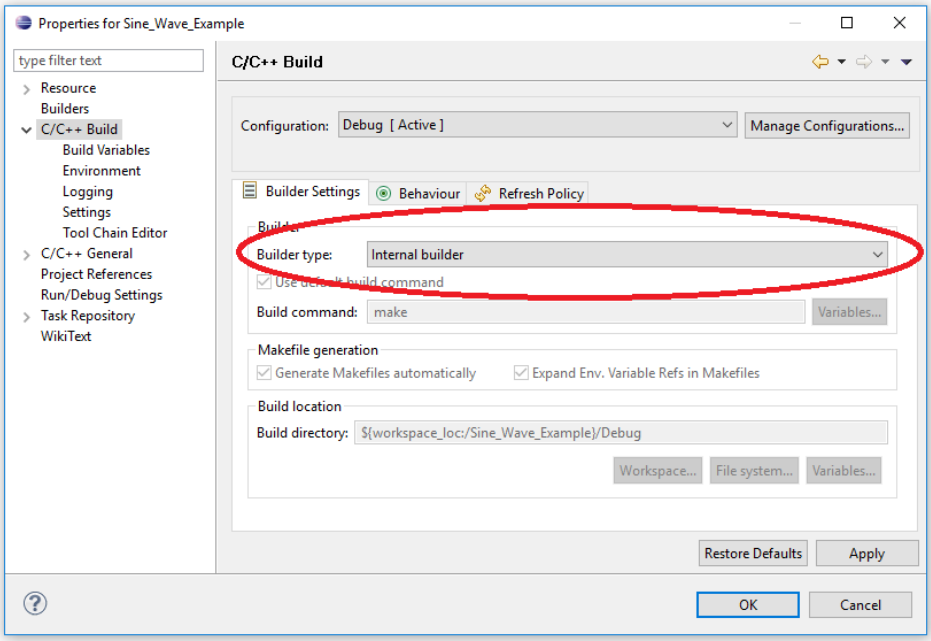

h) Now, under C/C++ Build→Settings select the “Tool Settings” tab and select Cross GCC Compiler→Miscellaneous. In the text box next to “Other flags” after *-c -fmessage-length=0* add a space and enter: *-mfpu=vfpv3 -mfloat-abi=softfp*

Then click OK.

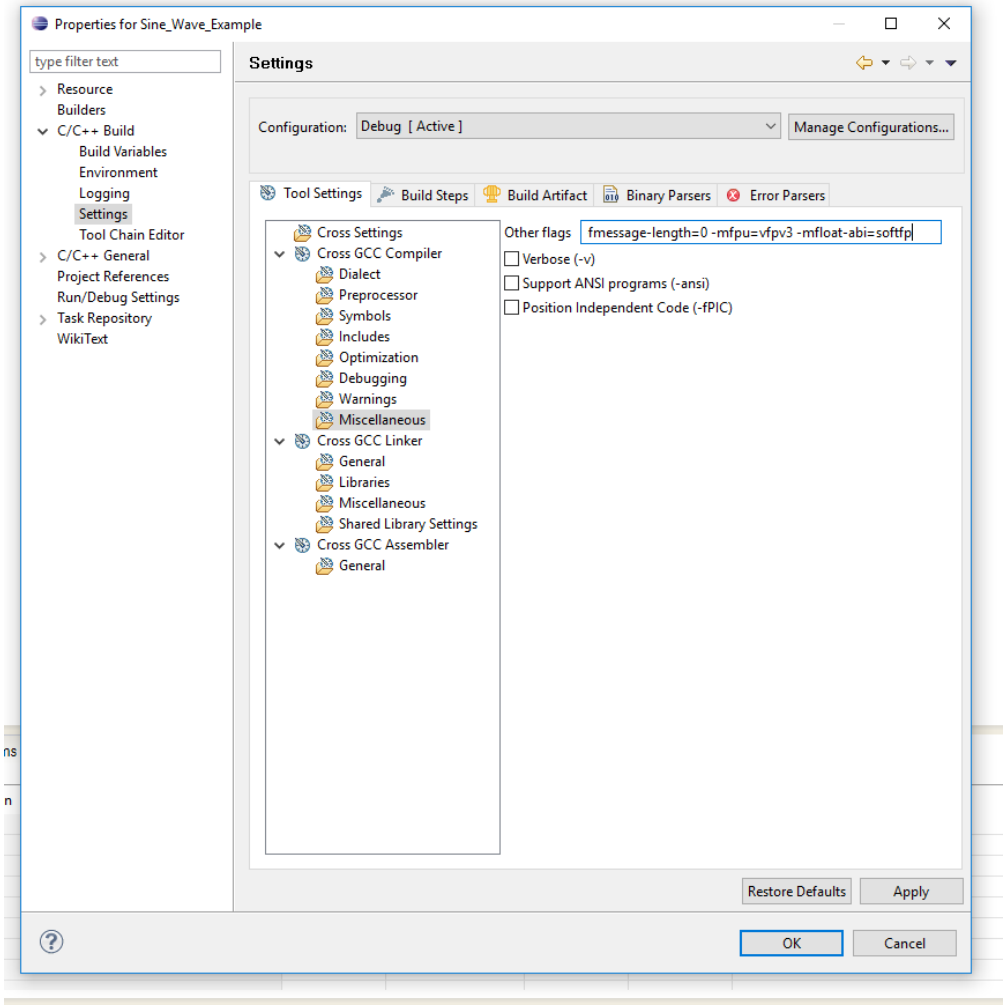

i) Right click on the project folder and click import.

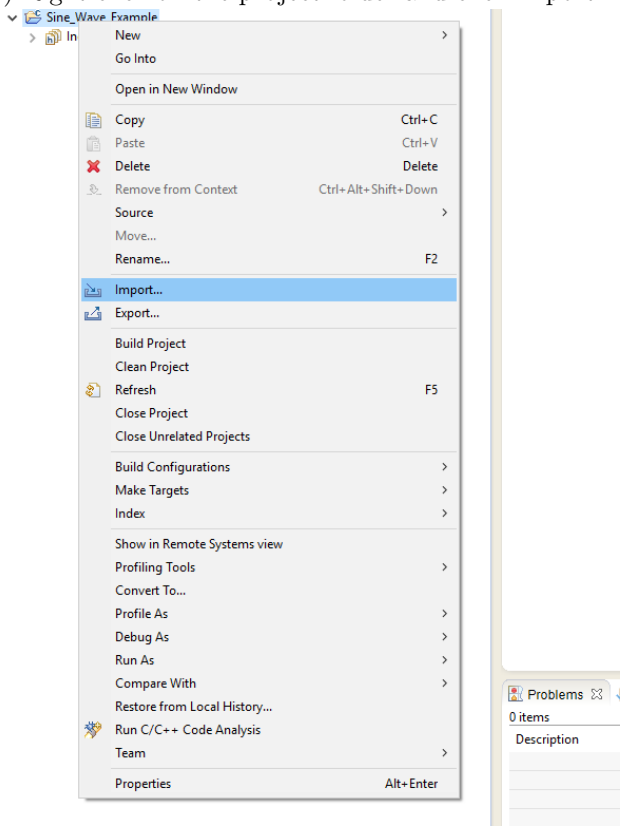

j) Select General→ File System, then click next.

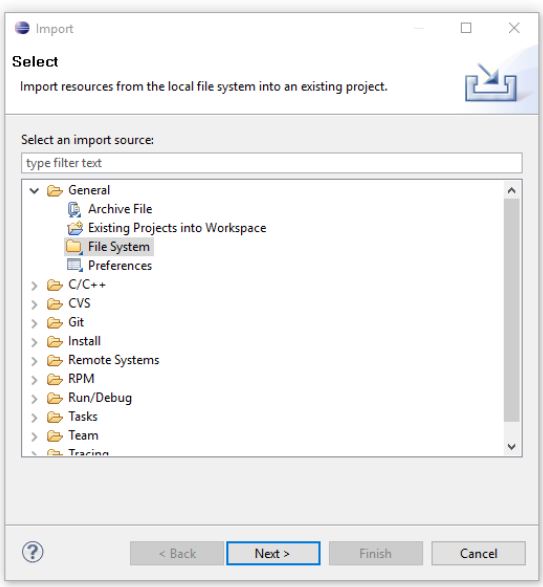

k) Select all the .c and .h files; they should be under . . . codegen/lib/function_name. To find the exact folder location refer to step 2f. Once all the appropriate files are selected, click Finish.

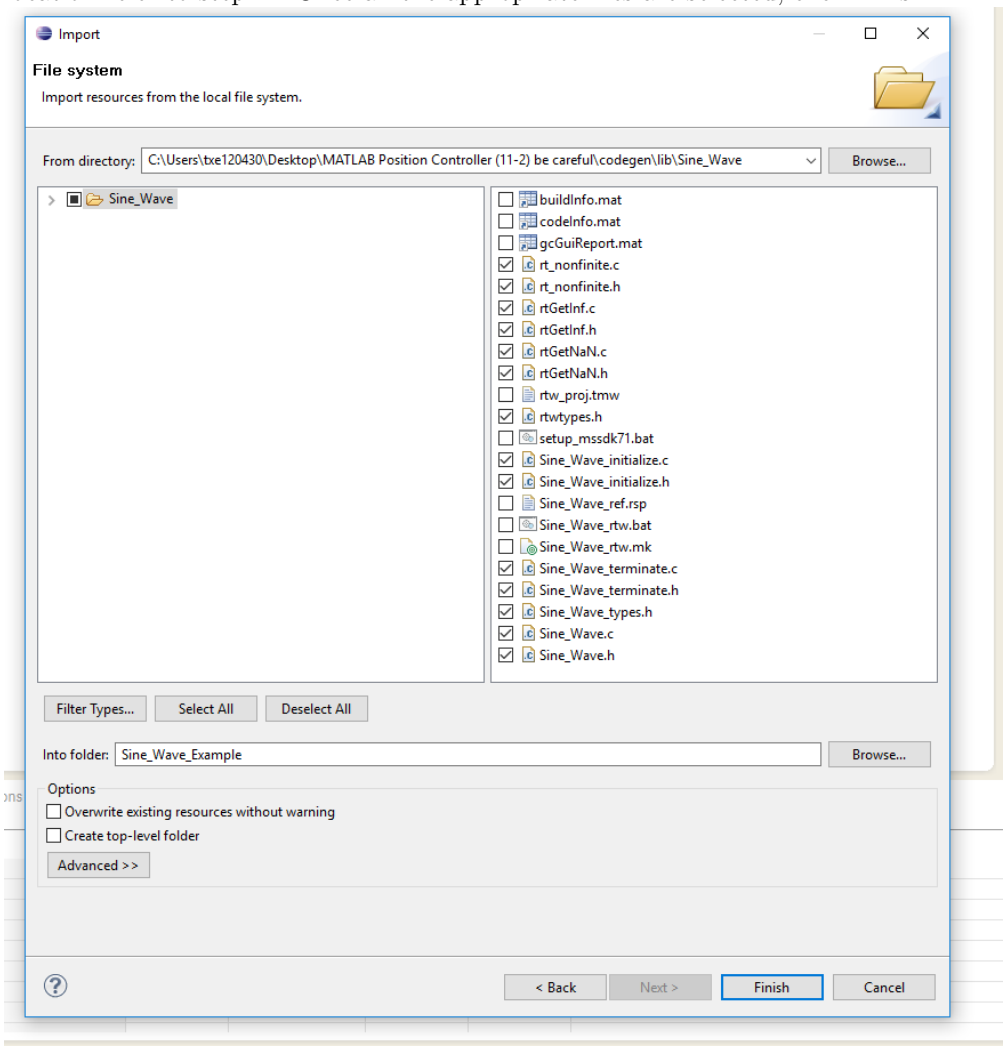

l) Now, build the project.

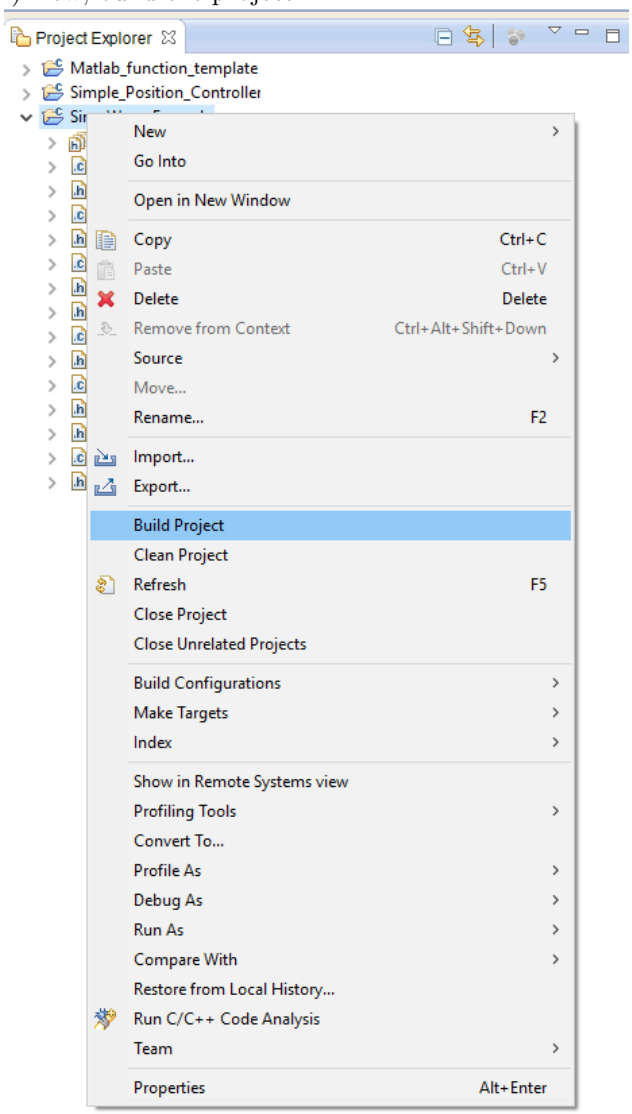

m) Once the project is built successfully, the console should look like this and the .so file should be under the "Binaries" within your project. Copy the .so file so that is can be pasted to the myRIO (next step). Only copy the .so file, do not copy the files contained in the .so file.

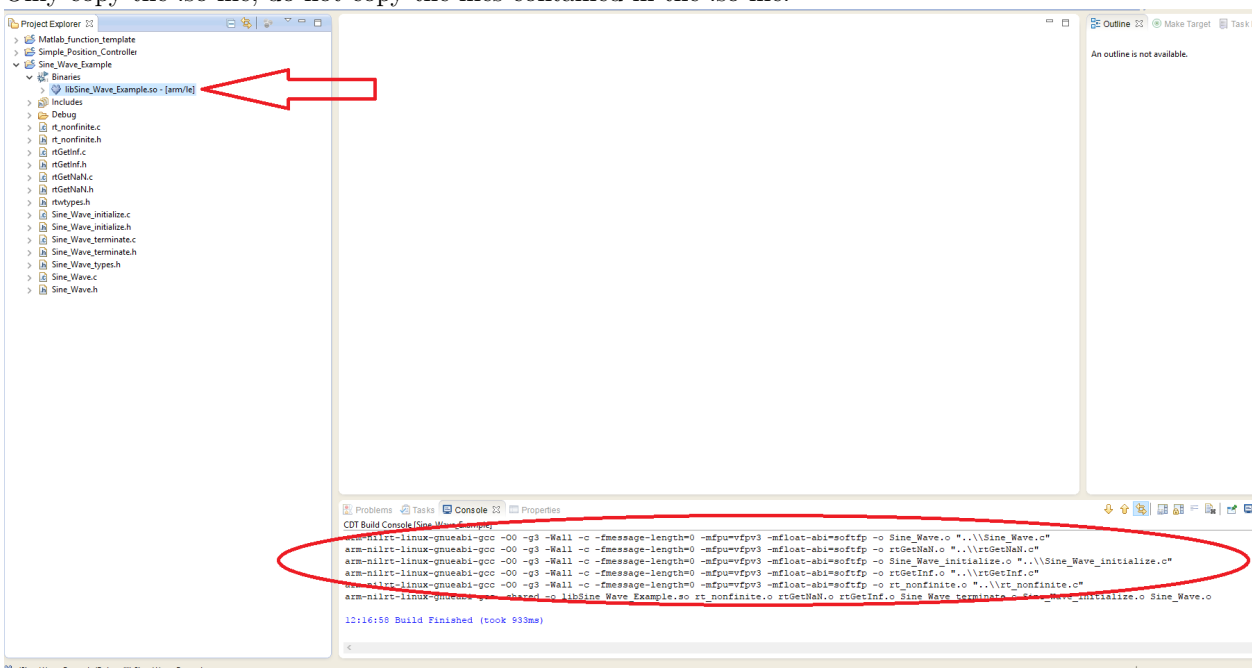

C.4 Copying the Shared Object file to the myRIO

Steps b-d are not needed if the myRIO is located under "Remote Systems" (to see if the myRIO is located under "Remote Systems" and look for the myRIO's IP Address). If the user does not know the myRIO's IP Address, it can be found by launching NI Max desktop application and selecting "Remote Systems" on left side of the window.

a) Click “Remote System Explorer” on the right hand side of the window.

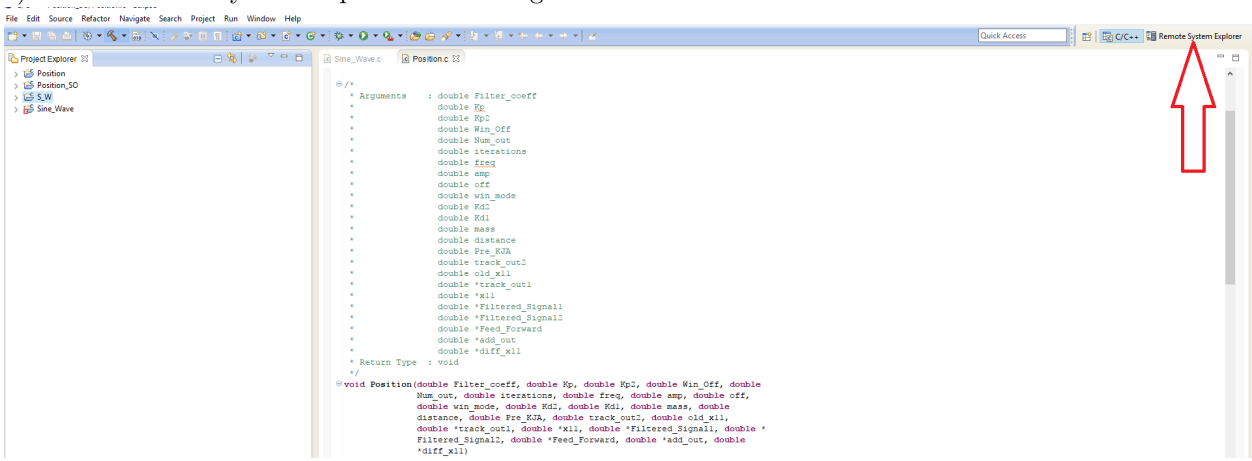

b) Click the “Define a connection to remote system” button (circled in red). Note that the myRIO’s IP address is 172.22.11.2 when connected via USB, and 172.16.0.1 when connected via WiFi.

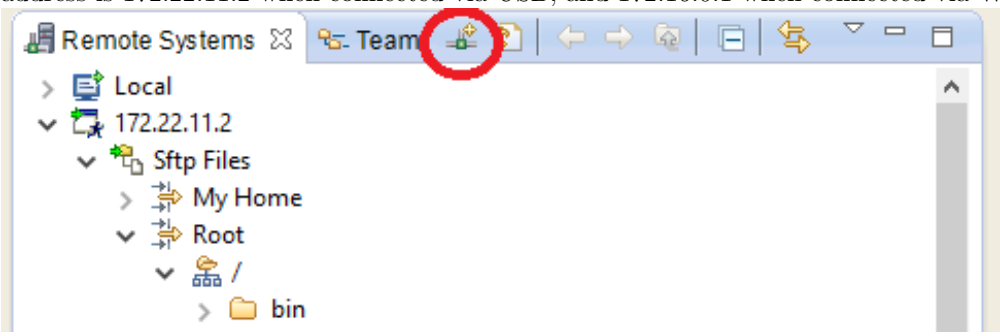

c) Select “SSH Only” then click next

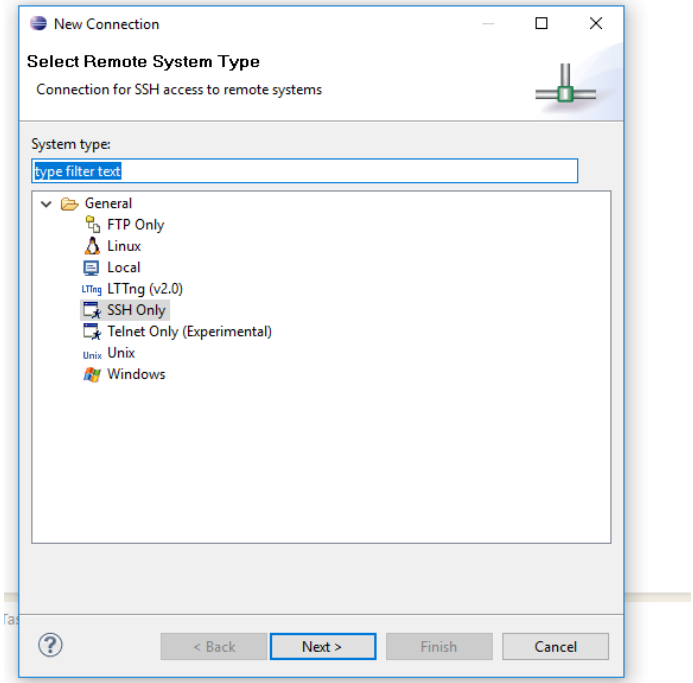

d) Enter the IP Address of the myRIO as the “Host name” and “Connection name”, and then click finish.

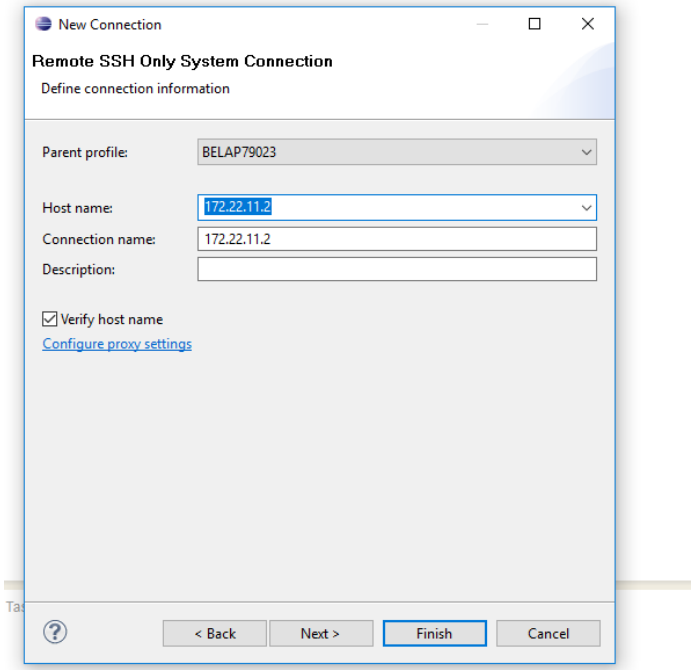

e) Now double click on the myRIO's IP address and go to Sftp Files→ Root, then enter the myRIO's login information (currently the username and password are both "admin"). Then go to /usr/local/lib and paste the .so file to this folder.

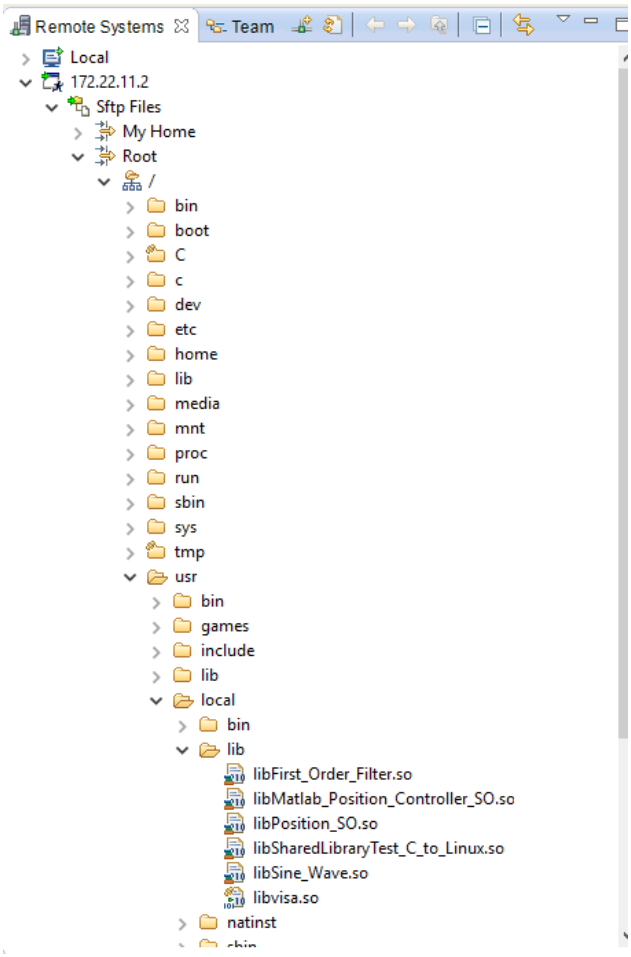

C.5 Creating a Case for your Controller

The easiest and quickest way to get started in labview would be to create a duplicate case, with a unique and new name, within the "Controller Case Structure", described in Table B.2.

a) In the example below, we have created a duplicate of "Holonomic Controller v8" and named it "Duplicate Test".

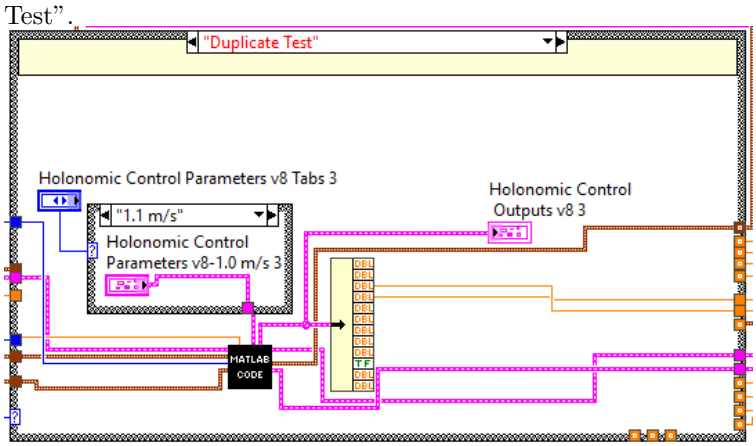

b) Note that this will create duplicate input and output clusters on the front panel. Next add a tab to the "Controller Section" tabs and ensure it has the same name as your case.

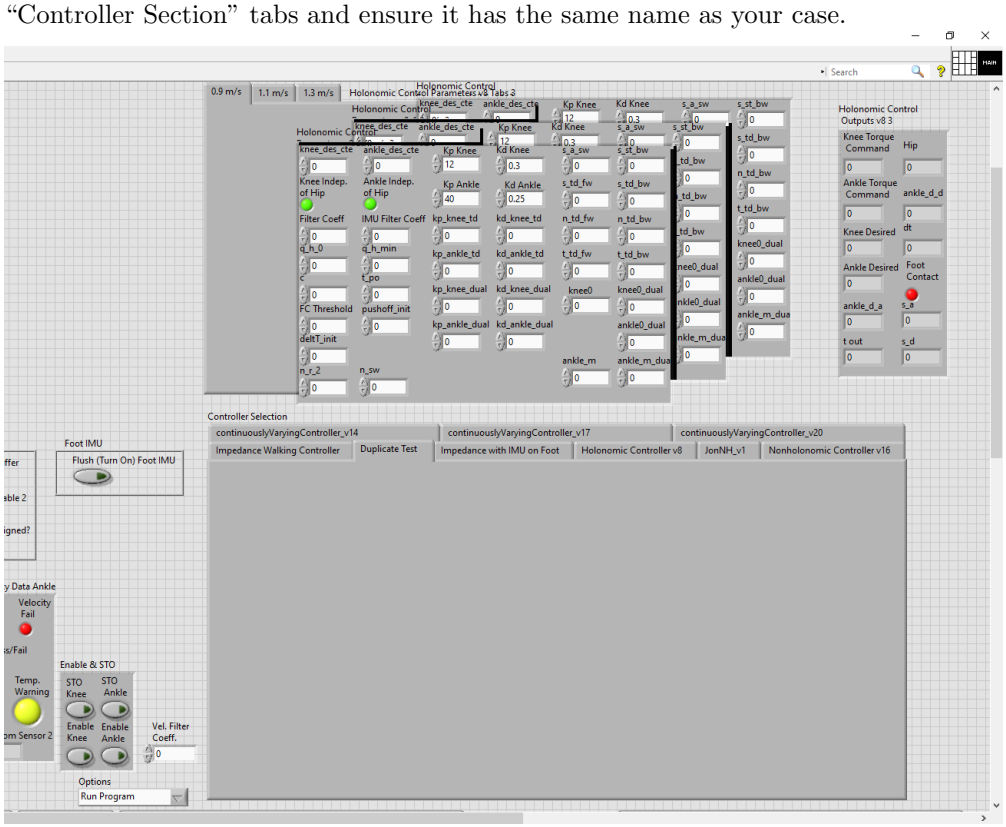

c) Next move the duplicated input/output clusters into your new tab and rename them accordingly.

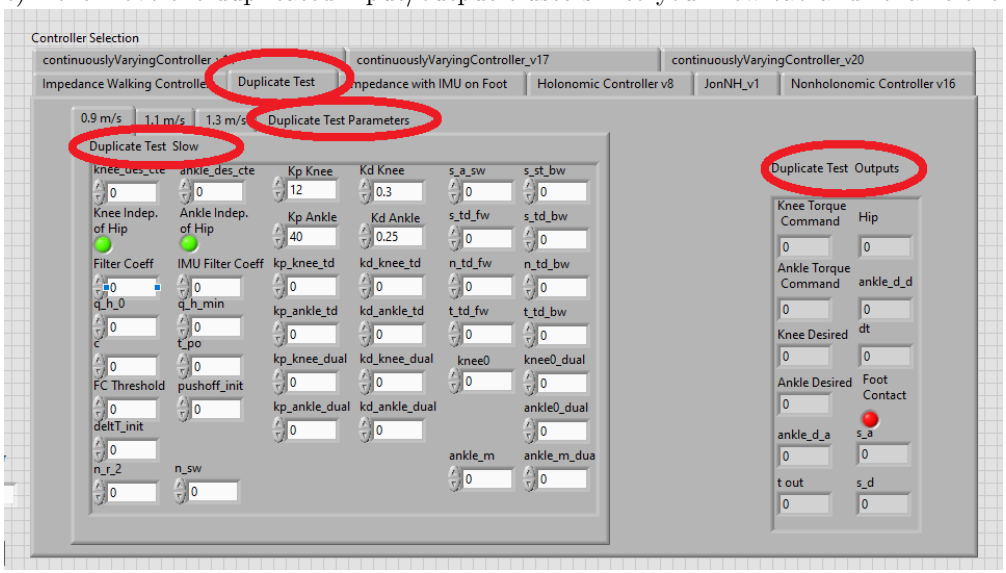

d) Next, save a duplicate of a working "Matlab Code" VI. Use your new "Matlab Code" VI to replace the existing "Matlab Code" VI in your case. Note that when the the tab and case are named correctly, then case structure name will be shown in black text, otherwise it will be shown in red (see below).

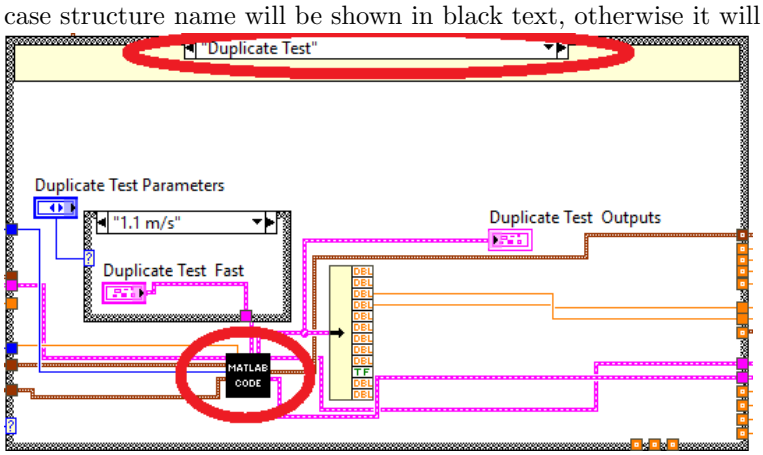

e) Now you can follow the steps in the next section to read your controller's .so file. Below is an example of the "Holonomic Controller v8" which you can edit to meet your specific controller needs.

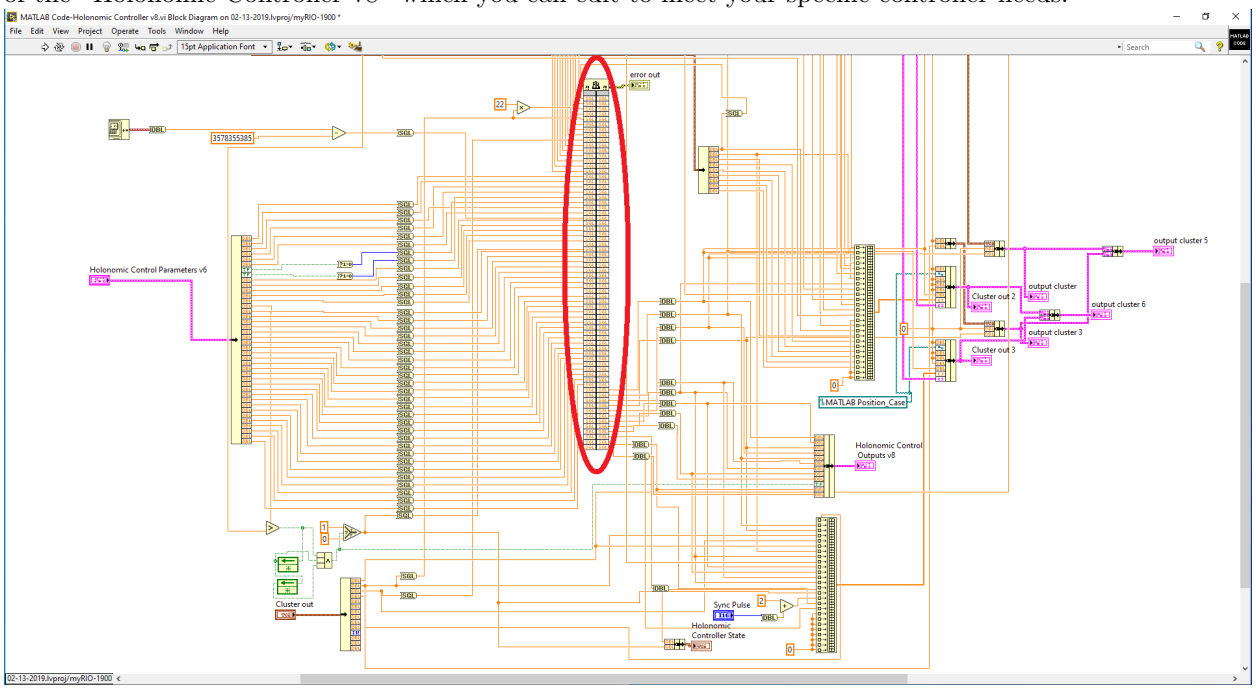

C.6 Implementing Shared Object file onto LabVIEW code

a) Go to LabVIEW and add the Call Library Function Node to the Block Diagram.

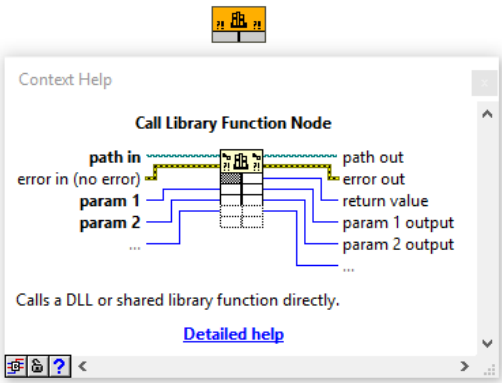

b) Double click on the Call Library Function Node and go to the "Function" tab. Then, under "Thread" select "Run in any thread". The "Function name" should be the same function name that was used in MATLAB. The Library path is where the .so file is located in the myRIO. After filling out the information under the "Function" tab select the "Parameter" tab.

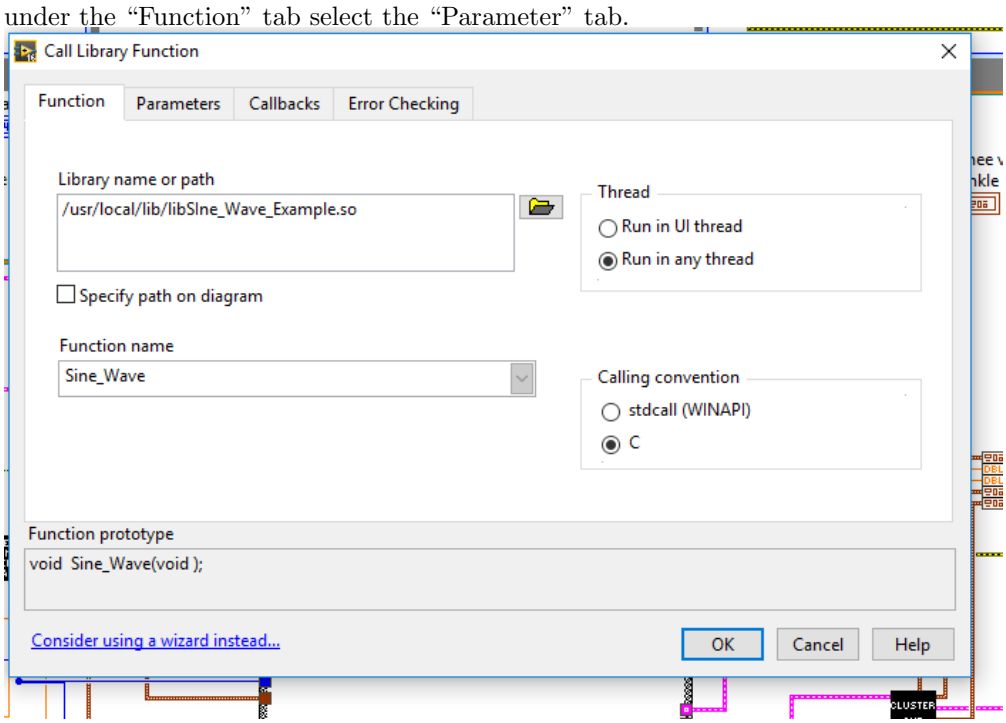

c) Add the inputs and outputs of the MATLAB code. In "Sine_Wave" MATLAB code used in this tutorial, diff_x11 is the only output (return parameter) and x11, old_x11, and iterations are all inputs. Since the "Sine_Wave" MATLAB code only has one output, that output is treated as the return parameter. However, if the MATLAB code had multiple outputs then, the return parameter would have a "Type" of "void" (will not be used). For inputs, "Pass" is "Value" and for outputs (when there is more than one output), "Pass" is "Pointer to Value". In addition, for the return parameter there is not a "Pass" option. Below are examples of the settings for each parameter type (return, input, and output):

Return Parameter Settings

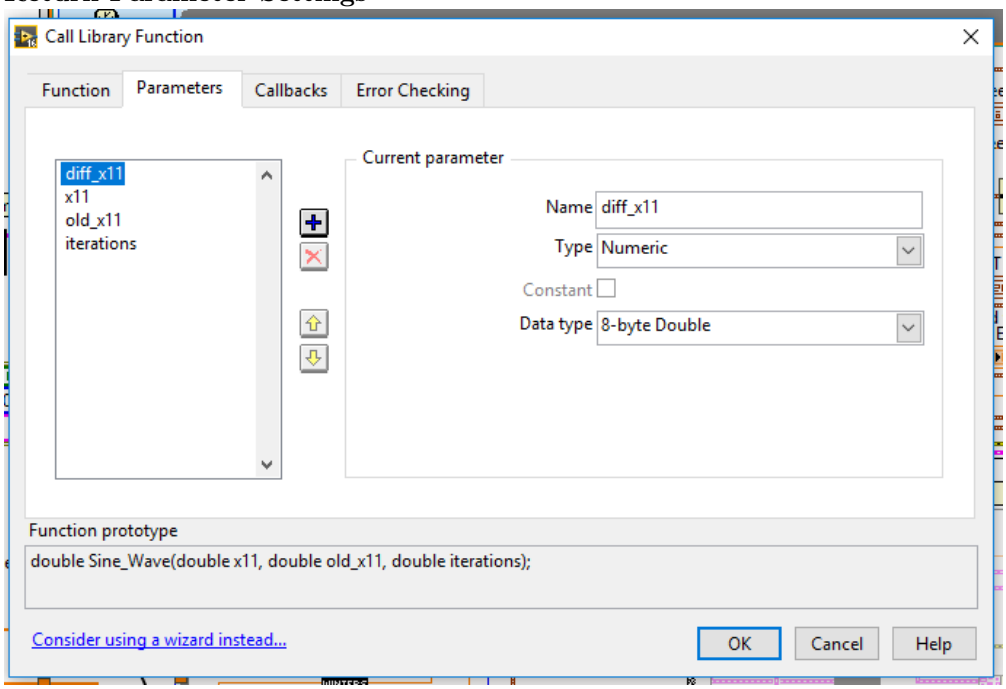

Input Parameter Settings

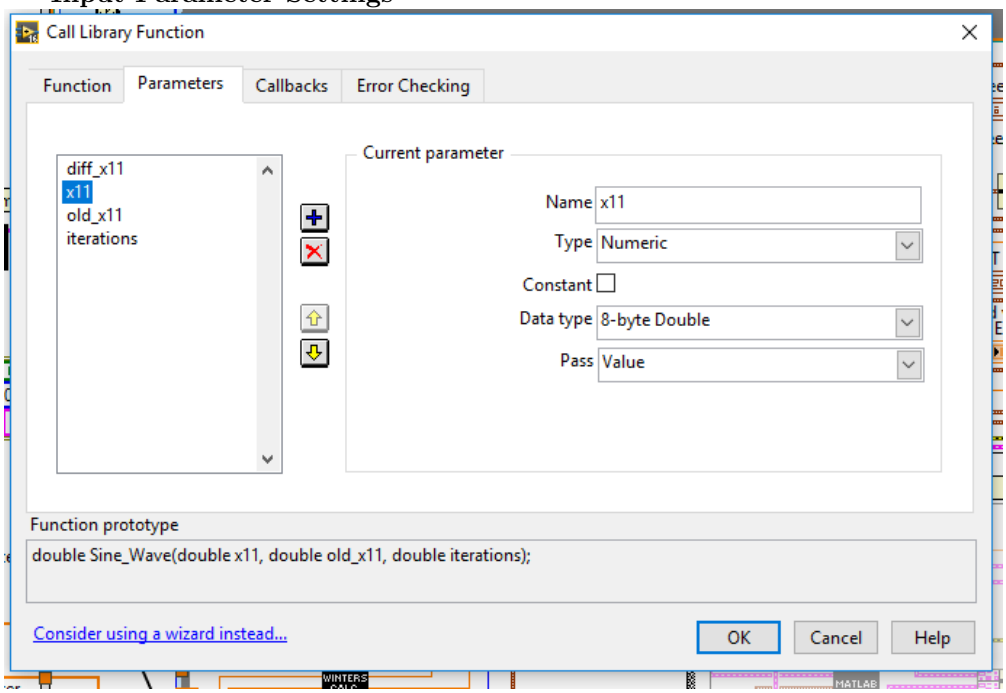

Output Parameter Settings (for Multiple Outputs)

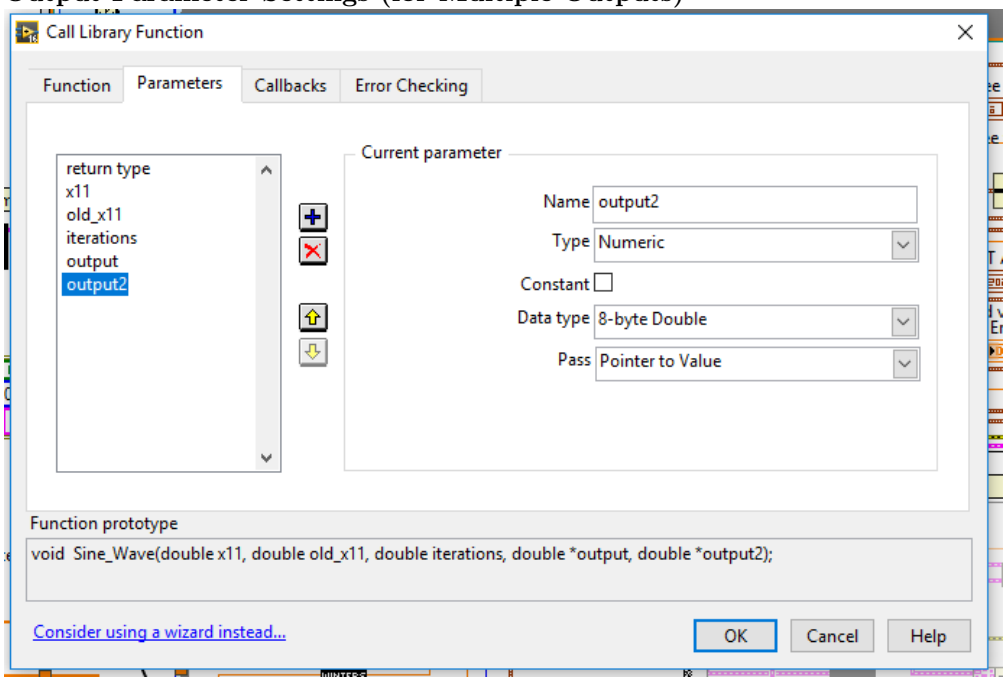

d) Now connect the inputs to the corresponding constants or controls then, connect the outputs to the corresponding indicators like so. The LabVIEW block below has one output (the return parameter) and three inputs.

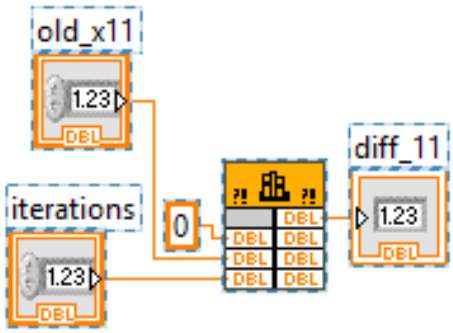

The tutorial is now complete! To test the implementation of the MATLAB code on LabVIEW, click run.

APPENDIX D

PROSTHETIC LINK CHARACTERISTICS

This appendix is dedicated to estimating prosthetic leg link characteristics, such as link lengths, mass, center of mass (CoM), and moment of inertias. Center of mass and moment of inertias are based on a coordinate system (Labeled *Coordinate System1* in Fig. D.1) located at the medial-lateral center of the knee actuator, and along the knee's axis of rotation. Note that the values in Table D.1 are based on CAD model estimates and do not include some items in the final physical version of the prosthesis, such as a cosmetic foot shell, shoe, or wiring.

Link heights are defined as follows. L1: Distance from the most narrow portion of the leg's male pyramid adapter (which is approximately where the lowest point of the amputee's socket will rest) to the knee actuators axis of rotation. L2: Distance from the knee axis of rotation to the ankle axis of rotation. If desirable, this value can increase by adjusting the pylon system that connects the knee and ankle actuators. L3: Distance from the ankle axis of rotation to the bottom of the prosthetic foot. This does not include the cosmetic foot shell or the shoe.

Table D.1: Leg Link Characteristics

Link	Mass (g)	Min. Height (mm)	CoM (mm)	Principal Axes of inertia	Principal Moment of Inertia @ CoM (g*mm^2)
Thigh (L1)	913.47	84.16	X=3.06 Y=8.52 Z=19.21	I_x=(0.03, -0.26, 0.97) I_y=(0.98, -0.16, -0.08) I_z=(0.18, 0.95, 0.25)	P_x=1,078,252.88 P_y=1,686,385.92 P_z=1,929,582.10
Shank (L2)	2891.34	328.56	X=-2.03 Y=0.26 Z=-124.61	I_x=(0.00, -0.02, 1.00) I_y=(1.00, 0.02, 0.00) I_z=(-0.02, 1.00, 0.02)	P_x=5,465,790.28 P_y=23,455,873.22 P_z=24,621,622.88
Foot (L3)	710.96	80.36	X=18.35 Y=1.06 Z=-368.89	I_x=(-0.90, 0.00, 0.43) I_y=(0.43, 0.00, 0.90) I_z=(0.00, 1.00, 0.00)	P_x=416,720.37 P_y=1,763,745.84 P_z=1,822,387.79

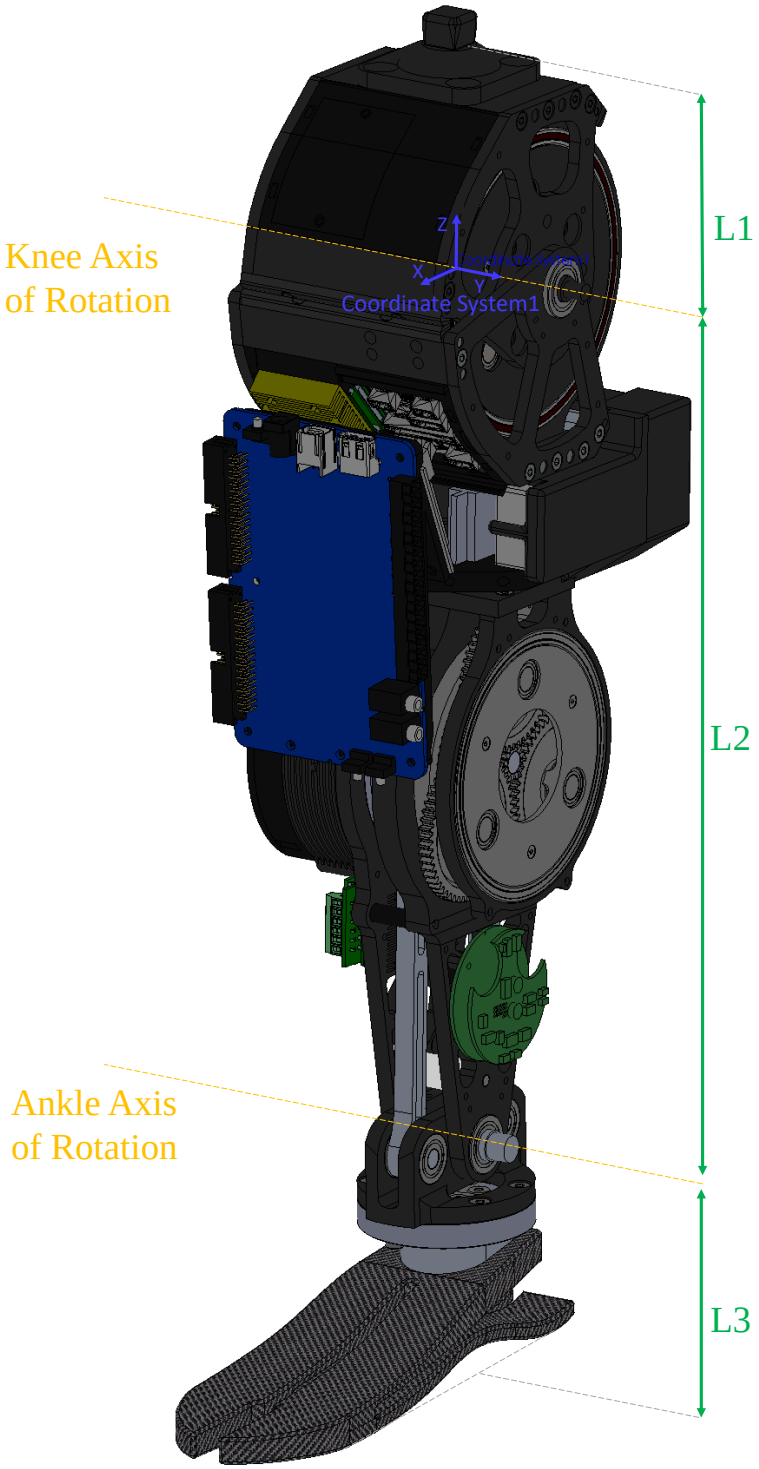

Figure D.1: Visual definitions of coordinate system (blue), axes of rotation (yellow), and link lengths of the prosthesis (green). Note that gray lines are only used to aid visualization.

REFERENCES

[1] Adamczyk, P. G., M. Roland, and M. E. Hahn (2013). Novel method to evaluate angular stiffness of prosthetic feet from linear compression tests. *Journal of Biomechanical Engineering 135*(10), 104502.

[2] Allen, D. P., E. Bolívar, S. Farmer, W. Voit, and R. D. Gregg (2019). Mechanical simplification of variable-stiffness actuators using dielectric elastomer transducers. In *Actuators*, Volume 8, pp. 44. Multidisciplinary Digital Publishing Institute.

[3] American Academy of Orthopaedic Surgeons (1952). *Orthopaedic Appliances Atlas*, Volume 2. JW Edwards.

[4] Apgar, T., P. Clary, K. Green, A. Fern, and J. Hurst (2018). Fast online trajectory optimization for the bipedal robot cassie. In *Robotics: Science and Systems*, Pittsburg, Pennsylvania.

[5] Au, S. K. and H. Herr (2008). Powered ankle-foot prosthesis. *IEEE Robot. Automat. Mag. 15*(3), 52–59.

[6] Au, S. K., J. Weber, and H. Herr (2009). Powered ankle–foot prosthesis improves walking metabolic economy. *IEEE Transactions on Robotics 25*(1), 51–66.

[7] Azocar, A. F., L. M. Mooney, L. J. Hargrove, and E. J. Rouse (2018). Design and characterization of an open-source robotic leg prosthesis. In *2018 7th IEEE International Conference on Biomedical Robotics and Biomechatronics (Biorob)*, pp. 111–118. IEEE.

[8] Bateni, H. and S. J. Olney (2002). Kinematic and kinetic variations of below-knee amputee gait. *JPO: Journal of Prosthetics and Orthotics 14*(1), 2–10.

[9] Berry, D. (2006). Microprocessor prosthetic knees. *Physical Medicine and Rehabilitation Clinics 17*(1), 91–113.

[10] Bobrow, J. and K. Lum (1996). Adaptive, high bandwidth control of a hydraulic actuator. *Journal of Dynamic Systems, Measurements and Control 118*(4), 714–720.

[11] Bolívar, E., S. Rezazadeh, and R. Gregg (2017). A general framework for minimizing energy consumption of series elastic actuators with regeneration. In *Proceedings of the ASME Dynamic Systems and Control Conference. ASME Dynamic Systems and Control Conference*, Volume 1. NIH Public Access.

[12] Borjian, R., J. Lim, M. B. Khamesee, and W. Melek (2008). The design of an intelligent mechanical active prosthetic knee. In *Industrial Electronics, 34th Annual Conference of IEEE*, pp. 3016–3021. IEEE.

[13] Browning, R. C., J. R. Modica, R. Kram, and A. Goswami (2007). The effects of adding mass to the legs on the energetics and biomechanics of walking. *Medicine & Science in Sports & Exercise 39*(3), 515–525.

[14] Caputo, J. M. and S. H. Collins (2014). A universal ankle–foot prosthesis emulator for human locomotion experiments. *Journal of biomechanical engineering 136*(3).

[15] Carignan, C. R. and K. R. Cleary (2000). Closed-loop force control for haptic simulation of virtual environments. *Haptics-e, The electronic journal of haptics research 1*(2), 1–14.

[16] Cempini, M., L. J. Hargrove, and T. Lenzi (2017). Design, development, and bench-top testing of a powered polycentric ankle prosthesis. In *2017 IEEE/RSJ International Conference on Intelligent Robots and Systems*, pp. 1064–1069.

[17] Census.gov (2017). Table 205. Cumulative Percent Distribution of Population by Height and Sex: 2007 to 2008. [Online]. Available: https://www2.census.gov/library/publications/2010/compendia/statab/130ed/tables/11s0205.pdf.

[18] Chou, C.-P. and B. Hannaford (1996). Measurement and modeling of mckibben pneumatic artificial muscles. *IEEE Transactions on robotics and automation 12*(1), 90–102.

[19] Colgate, J. E. and G. G. Schenkel (1997). Passivity of a class of sampled-data systems: Application to haptic interfaces. *Journal of robotic systems 14*(1), 37–47.

[20] Daerden, F., D. Lefeber, et al. (2002). Pneumatic artificial muscles: actuators for robotics and automation. *European journal of mechanical and environmental engineering 47*(1), 11–21.

[21] De Looze, M., H. Toussaint, D. Commissaris, M. Jans, and A. Sargeant (1994). Relationships between energy expenditure and positive and negative mechanical work in repetitive lifting and lowering. *J. Appl. Physiol. 77*(1), 420–426.

[22] Ding, Y. and H. W. Park (2017). Design and experimental implementation of a quasi-direct-drive leg for optimized jumping. In *2017 IEEE/RSJ International Conference on Intelligent Robots and Systems*, pp. 300–305.

[23] Eilenberg, M., H. Geyer, and H. Herr (2010). Control of a powered ankle–foot prosthesis based on a neuromuscular model. *IEEE Trans. Neural Sys. Rehab. Eng. 18*(2), 164–173.

[24] Elery, T., S. Rezazadeh, C. Nesler, J. Doan, H. Zhu, and R. D. Gregg (2018). Design and benchtop validation of a powered knee-ankle prosthesis with high-torque, low-impedance actuators. In *IEEE International Conference on Robotics and Automation*.

[25] Elery, T., S. Rezazadeh, C. Nesler, and R. D. Gregg (2020, under review). Design and validation of a powered knee-ankle prosthesis with high-torque, low-impedance actuators. *IEEE Trans. Robotics*.

[26] Embry, K. R., D. J. Villarreal, and R. D. Gregg (2016). A unified parameterization of human gait across ambulation modes. In *IEEE Eng. Med. Bio. Conf.*, pp. 2179–2183.

[27] Farley, C. T., H. H. Houdijk, C. Van Strien, and M. Louie (1998). Mechanism of leg stiffness adjustment for hopping on surfaces of different stiffnesses. *Journal of Applied Physiology 85*(3), 1044–1055.

[28] Farris, R. J., H. A. Quintero, and M. Goldfarb (2011). Preliminary evaluation of a powered lower limb orthosis to aid walking in paraplegic individuals. *IEEE Trans. Neural Sys. Rehab. Eng. 19*(6), 652–659.

[29] Flowers, W. C. and R. W. Mann (1977). An electrohydraulic knee-torque controller for a prosthesis simulator. *Journal of Biomechanical Engineering 99*(1), 3–8.

[30] Fu, A., C. Fu, K. Wang, D. Zhao, X. Chen, and K. Chen (2013). The key parameter selection in design of an active electrical transfemoral prosthesis. In *IEEE International Conference on Robotics and Biomimetics*, pp. 1716–1721. IEEE.

[31] Gailey, R., K. Allen, J. Castles, J. Kucharik, and M. Roeder (2008). Review of secondary physical conditions associated with lower-limb amputation and long-term prosthesis use. *Journal of Rehabilitation Research & Development 45*(1), 15–30.

[32] Gailey, R. S., M. A. Wenger, M. Raya, N. Kirk, K. Erbs, P. Spyropoulos, and M. S. Nash (1994). Energy expenditure of trans-tibial amputees during ambulation at self-selected pace. *Prosthetics Orthotics Int. 18*(2), 84.

[33] Gregg, R. D., T. Lenzi, L. J. Hargrove, and J. W. Sensinger (2014). Virtual constraint control of a powered prosthetic leg: From simulation to experiments with transfemoral amputees. *IEEE Trans. Robotics 30*(6), 1455–1471.

[34] Gupta, V. and A. Deb (2012). Analysis of variable gear system on energy consumption in electric vehicle using simulation tool. *IJSSST 13*(2), 7–11.

[35] Halsne, E. G., M. G. Waddingham, and B. J. Hafner (2013). Long-term activity in and among persons with transfemoral amputation. *J Rehabil Res Dev 50*(4), 515–30.

[36] Herr, H. M. and A. M. Grabowski (2011). Bionic ankle–foot prosthesis normalizes walking gait for persons with leg amputation. *Proceedings of the Royal Society B: Biological Sciences 279*(1728), 457–464.

[37] Hogan, N. (1985). Impedance control: An approach to manipulation: Part II-Implementation. *Journal of dynamic systems, measurement, and control 107*(1), 8–16.

[38] Hoover, C. D., G. D. Fulk, and K. B. Fite (2012). The design and initial experimental validation of an active myoelectric transfemoral prosthesis. *Journal of Medical Devices 6*(1), 011005.

[39] Horn, J. C. (2015). Design and implementation of the powered self-contained ampro prostheses. Master's thesis, Texas A&M University.

[40] Houdijk, H., E. Pollmann, M. Groenewold, H. Wiggerts, and W. Polomski (2009). The energy cost for the step-to-step transition in amputee walking. *Gait & posture 30*(1), 35–40.

[41] Huang, S., J. P. Wensman, and D. P. Ferris (2014). An experimental powered lower limb prosthesis using proportional myoelectric control. *Journal of Medical Devices 8*(2).

[42] Hubicki, C., J. Grimes, M. Jones, D. Renjewski, A. Spröwitz, A. Abate, and J. Hurst (2016). Atrias: Design and validation of a tether-free 3d-capable spring-mass bipedal robot. *The International Journal of Robotics Research 35*(12), 1497–1521.

[43] Hurwitz, D. E., D. R. Sumner, and J. A. Block (2001). Bone density, dynamic joint loading and joint degeneration. *Cells Tissues Organs 169*(3), 201–209.

[44] Jaegers, S. M., J. H. Arendzen, and H. J. de Jongh (1995). Prosthetic gait of unilateral transfemoral amputees: a kinematic study. *Archives of physical medicine and rehabilitation 76*(8), 736–743.

[45] Jayaraman, C., S. Hoppe-Ludwig, S. Deems-Dluhy, M. McGuire, C. Mummidisetty, R. Siegal, A. Naef, B. E. Lawson, M. Goldfarb, K. E. Gordon, et al. (2018). Impact of powered knee-ankle prosthesis on low back muscle mechanics in transfemoral amputees: A case series. *Frontiers in neuroscience 12*, 134.

[46] Jindrich, D. L. and R. J. Full (2002). Dynamic stabilization of rapid hexapedal locomotion. *Journal of Experimental Biology 205*(18), 2803–2823.

[47] Johansson, J., D. Sherrill, P. Riley, P. Bonato, and H. Herr (2005). A clinical comparison of variable-damping and mechanically passive prosthetic knee devices. *Amer. J. Phys. Med. Rehab. 84*(8), 563–575.

[48] Kapti, A. O. and M. S. Yucenur (2006). Design and control of an active artificial knee joint. *Mechanism and machine theory 41*(12), 1477–1485.

[49] Kaufman, K. R., S. Frittoli, and C. A. Frigo (2012). Gait asymmetry of transfemoral amputees using mechanical and microprocessor-controlled prosthetic knees. *Clinical Biomechanics 27*(5), 460–465.

[50] Kenneally, G., A. De, and D. E. Koditschek (2016). Design principles for a family of direct-drive legged robots. *IEEE Robotics and Automation Letters 1*(2), 900–907.

[51] Kim, M., T. Chen, T. Chen, and S. H. Collins (2018). An ankle–foot prosthesis emulator with control of plantarflexion and inversion–eversion torque. *IEEE Transactions on Robotics 34*(5), 1183–1194.

[52] Klute, G., J. Czerniecki, and B. Hannaford (2000). Muscle-like pneumatic actuators for below-knee prostheses. In *Proceedings the 7th International Conference on New Actuators*, pp. 289–292.

[53] Kuitunen, S., K. Ogiso, and P. Komi (2011). Leg and joint stiffness in human hopping. *Scandinavian Journal of Medicine & Science in Sports 21*(6), e159–e167.

[54] Kulkarni, J., W. Gaine, J. Buckley, J. Rankine, and J. Adams (2005). Chronic low back pain in traumatic lower limb amputees. *Clinical rehabilitation 19*(1), 81–86.

[55] Lambrecht, B. G. and H. Kazerooni (2009). Design of a semi-active knee prosthesis. In *IEEE International Conference on Robotics and Automation*, pp. 639–645. IEEE.

[56] LaPre, A. K. and F. Sup (2013). Redefining prosthetic ankle mechanics: Non-anthropomorphic ankle design. In *IEEE International Conference on Rehabilitation Robotics*, pp. 1–5. IEEE.

[57] Laschowski, B. and J. Andrysek (2018). Electromechanical design of robotic transfemoral prostheses. In *IEEE Int. Desg. Eng. Tech. Conf. & Info. in Eng. Conf.*

[58] Lawson, B., H. Varol, A. Huff, E. Erdemir, and M. Goldfarb (2013). Control of stair ascent and descent with a powered transfemoral prosthesis. *IEEE Trans. Neural Sys. Rehab. Eng. 21*(3), 466–473.

[59] Lawson, B. E., J. Mitchell, D. Truex, A. Shultz, E. Ledoux, and M. Goldfarb (2014a). A robotic leg prosthesis: Design, control, and implementation. *IEEE Robotics & Automation Magazine 21*(4), 70–81.

[60] Lawson, B. E., J. Mitchell, D. Truex, A. Shultz, E. Ledoux, and M. Goldfarb (2014b). A robotic leg prosthesis: Design, control, and implementation. *IEEE Robotics & Automation Magazine 21*(4), 70–81.

[61] Lawson, B. E., B. Ruhe, A. Shultz, and M. Goldfarb (2014). A powered prosthetic intervention for bilateral transfemoral amputees. *IEEE Transactions on Biomedical Engineering 62*(4), 1042–1050.

[62] Ledoux, E. D. and M. Goldfarb (2017). Control and evaluation of a powered transfemoral prosthesis for stair ascent. *IEEE Trans. Neural Syst. and Rehab. Eng. 25*(7), 917–924.

[63] Lenzi, T., M. Cempini, L. Hargrove, and T. Kuiken (2018). Design, development, and testing of a lightweight hybrid robotic knee prosthesis. *The International Journal of Robotics Research 37*(8), 953–976.

[64] Lenzi, T., M. Cempini, L. J. Hargrove, and T. A. Kuiken (2019). Design, development, and validation of a lightweight nonbackdrivable robotic ankle prosthesis. *IEEE/ASME Transactions on Mechatronics 24*(2), 471–482.

[65] Lenzi, T., L. Hargrove, and J. Sensinger (2014). Speed-adaptation mechanism: Robotic prostheses can actively regulate joint torque. *IEEE Robotics & Automation Magazine 21*(4), 94–107.

[66] Lenzi, T., J. Sensinger, J. Lipsey, L. Hargrove, and T. Kuiken (2015). Design and preliminary testing of the ric hybrid knee prosthesis. In *Engineering in Medicine and Biology Society (EMBC), 2015 37th Annual International Conference of the IEEE*, pp. 1683–1686. IEEE.

[67] Levai, Z. (1968). Structure and analysis of planetary gear trains. *Journal of mechanisms 3*(3), 131–148.

[68] Liu, M., P. Datseris, and H. H. Huang (2012). A prototype for smart prosthetic legs-analysis and mechanical design. In *Advanced Materials Research*, Volume 403, pp. 1999–2006. Trans Tech Publ.

[69] Lv, G., H. Zhu, and R. D. Gregg (2018). On the design and control of highly backdrivable lower-limb exoskeletons: A discussion of past and ongoing work. *IEEE Control Systems Magazine 38*(6), 88–113.

[70] Martin, A. and R. D. Gregg (2017). Stable, robust hybrid zero dynamics control of powered lower-limb prostheses. *IEEE Trans. Automatic Control 62*(8), 3930–3942.

[71] McDowell, M. A., C. D. Fryar, C. L. Ogden, and K. M. Flegal (2008). Anthropometric reference data for children and adults: United states, 2003–2006. *National health statistics reports 10*(1-45), 5.

[72] Michael, J. W. and J. H. Bowker (2004). *Atlas of Amputations and Limb Deficiencies: Surgical, Prosthetic, and Rehabilitation Principles.* Rosemont, IL: American Academy of Orthopaedic Surgeons.

[73] Miller, W., A. Deathe, M. Speechley, and J. Koval (2001). The influence of falling, fear of falling, and balance confidence on prosthetic mobility and social activity among individuals with a lower extremity amputation. *Arch. Phys. Med. Rehab. 82*(9), 1238–1244.

[74] Morgenroth, D. C., A. D. Segal, K. E. Zelik, J. M. Czerniecki, G. K. Klute, P. G. Adamczyk, M. S. Orendurff, M. E. Hahn, S. H. Collins, and A. D. Kuo (2011). The effect of prosthetic foot push-off on mechanical loading associated with knee osteoarthritis in lower extremity amputees. *Gait & posture 34*(4), 502–507.

[75] Nolan, L. and A. Lees (2000). The functional demands on the intact limb during walking for active transfemoral and transtibial amputees. *Prosthetics and orthotics international 24*(2), 117–125.

[76] Norvell, D. C., J. M. Czerniecki, G. E. Reiber, C. Maynard, J. A. Pecoraro, and N. S. Weiss (2005). The prevalence of knee pain and symptomatic knee osteoarthritis among veteran traumatic amputees and nonamputees. *Archives of physical medicine and rehabilitation 86*(3), 487–493.

[77] Össur (2018). Power Knee. [Online]. Available: https://www.ossur.com/prosthetic-solutions/products/dynamic-solutions/power-knee.

[78] Ottobock (2018). Empower. [Online]. Available: https://www.ottobockus.com /prosthetics/lower-limb-prosthetics/solution-overview/empower-ankle/.

[79] Paine, N., S. Oh, and L. Sentis (2014). Design and control considerations for high-performance series elastic actuators. *IEEE/ASME Transactions on Mechatronics 19*(3), 1080–1091.

[80] Patterson, K. K., W. H. Gage, D. Brooks, S. E. Black, and W. E. McIlroy (2010). Evaluation of gait symmetry after stroke: a comparison of current methods and recommendations for standardization. *Gait & posture 31*(2), 241–246.

[81] Pfeifer, S., R. Riener, and H. Vallery (2012). An actuated transfemoral prosthesis with optimized polycentric knee joint. In *IEEE RAS & EMBS International Conference on Biomedical Robotics and Biomechatronics*, pp. 1807–1812. IEEE.

[82] Pieringer, D. S., M. Grimmer, M. F. Russold, and R. Riener (2017). Review of the actuators of active knee prostheses and their target design outputs for activities of daily living. In *IEEE Int. Conf. Rehabilitation Robotics*, pp. 1246–1253.

[83] Pillai, M. V., H. Kazerooni, and A. Hurwich (2011). Design of a semi-active knee-ankle prosthesis. In *IEEE International Conference on Robotics and Automation*, pp. 5293–5300. IEEE.

[84] Price, M. A., P. Beckerle, and F. C. Sup (2019). Design optimization in lower limb prostheses: A review. *IEEE Transactions on Neural Systems and Rehabilitation Engineering 27*(8), 1574–1588.

[85] Quintero, D., E. Reznick, D. J. Lambert, S. Rezazadeh, L. Gray, and R. D. Gregg (2018). Intuitive clinician control interface for a powered knee-ankle prosthesis: A case study. *IEEE J. Trans. Eng. in Health and Medicine 6*, 1–9.

[86] Quintero, D., D. J. Villarreal, and R. D. Gregg (2016). Preliminary experimental results of a unified controller for a powered knee-ankle prosthetic leg over various walking speeds. In *IEEE Int. Conf. Intelligent Robots Systems*, pp. 5427–5433.

[87] Quintero, D., D. J. Villarreal, D. J. Lambert, S. Kapp, and R. D. Gregg (2018). Continuous-phase control of a powered knee–ankle prosthesis: Amputee experiments across speeds and inclines. *IEEE Transactions on Robotics 34*(3), 686–701.

[88] R L Craig Company (2018). dBA Comparisons. [Online]. Available: https://www.rlcraigco.com /pdf/dba-comparison.pdf.

[89] Radin, E. L., H. G. Parker, J. W. Pugh, R. S. Steinberg, I. L. Paul, and R. M. Rose (1973). Response of joints to impact loading—iii: Relationship between trabecular microfractures and cartilage degeneration. *Journal of biomechanics 6*(1), 51–57.

[90] Ramos, J., B. Katz, M. Y. M. Chuah, and S. Kim (2018). Facilitating model-based control through software-hardware co-design. In *IEEE International Conference on Robotics and Automation*.

[91] Rezazadeh, S., A. Abate, R. L. Hatton, and J. W. Hurst (2018). Robot leg design: A constructive framework. *IEEE Access 6*(1), 54369–54387.

[92] Rezazadeh, S., C. Hubicki, M. Jones, A. Peekema, J. Van Why, A. Abate, and J. Hurst (2015). Spring-mass walking with atrias in 3d: Robust gait control spanning zero to 4.3 kph on a heavily underactuated bipedal robot. In *ASME Dynamic Systems and Control Conference*, Columbus, OH, pp. V001T04A003.

[93] Rezazadeh, S., D. Quintero, N. Divekar, and R. D. Gregg (2018). A phase variable approach to volitional control of powered knee-ankle prostheses. In *IEEE/RSJ International Conference on Intelligent Robots and Systems*, Madrid, Spain.

[94] Rezazadeh, S., D. Quintero, N. Divekar, E. Reznick, L. Gray, and R. D. Gregg (2019). A phase variable approach for improved rhythmic and non-rhythmic control of a powered knee-ankle prosthesis. *IEEE Access 7*, 109840–109855.

[95] Rouse, E. J., L. M. Mooney, and H. M. Herr (2014). Clutchable series-elastic actuator: Implications for prosthetic knee design. *Int. J. Robotics Research 33*(13), 1611–1625.

[96] Sagawa Jr, Y., K. Turcot, S. Armand, A. Thevenon, N. Vuillerme, and E. Watelain (2011). Biomechanics and physiological parameters during gait in lower-limb amputees: a systematic review. *Gait & posture 33*(4), 511–526.

[97] Saranli, U., M. Buehler, and D. E. Koditschek (2001). Rhex: A simple and highly mobile hexapod robot. *The International Journal of Robotics Research 20*(7), 616–631.

[98] Satkunskienė, D., V. Grigas, V. Eidukynas, and A. Domeika (2009). Acceleration based evaluation of the human walking and running parameters. *Journal of Vibroengineering 11*(1), 506–510.

[99] Schaarschmidt, M., S. W. Lipfert, C. Meier-Gratz, H.-C. Scholle, and A. Seyfarth (2012). Functional gait asymmetry of unilateral transfemoral amputees. *Human movement science 31*(4), 907–917.

[100] Segal, A., M. Orendurff, G. Klute, M. McDowell, J. Pecoraro, J. Shofer, and J. Czerniecki (2006). Kinematic and kinetic comparisons of transfemoral amputee gait using C-Leg® and Mauch SNS® prosthetic knees. *J. Rehab. Res. Dev. 43*(7), 857–870.

[101] Sellegren, K. R. (1982). An early history of lower limb amputations and prostheses. *The Iowa orthopaedic journal 2*, 13.

[102] Sensinger, J. W. and J. H. Lipsey (2012). Cycloid vs. harmonic drives for use in high ratio, single stage robotic transmissions. In *IEEE International Conference on Robotics and Automation*, pp. 4130–4135. IEEE.

[103] Seok, S., A. Wang, M. Y. M. Chuah, D. J. Hyun, J. Lee, D. M. Otten, J. H. Lang, and S. Kim (2015). Design principles for energy-efficient legged locomotion and implementation on the mit cheetah robot. *IEEE/ASME Transactions on Mechatronics 20*(3), 1117–1129.

[104] Seok, S., A. Wang, D. Otten, and S. Kim (2012). Actuator design for high force proprioceptive control in fast legged locomotion. In *IEEE/RSJ International Conference on Intelligent Robots and Systems (IROS)*, pp. 1970–1975.

[105] Seroussi, R. E., A. Gitter, J. M. Czerniecki, and K. Weaver (1996). Mechanical work adaptations of above-knee amputee ambulation. *Arch. of Physical Medicine and Rehabil. 77*(11), 1209–1214.

[106] Shamaei, K., G. S. Sawicki, and A. M. Dollar (2013a). Estimation of quasi-stiffness and propulsive work of the human ankle in the stance phase of walking. *PloS one 8*(3), e59935.

[107] Shamaei, K., G. S. Sawicki, and A. M. Dollar (2013b). Estimation of quasi-stiffness of the human knee in the stance phase of walking. *PloS one 8*(3), e59993.

[108] Shorter, K. A., A. Wu, and A. D. Kuo (2017). The high cost of swing leg circumduction during human walking. *Gait & posture 54*, 265–270.

[109] Shultz, A. H., B. E. Lawson, and M. Goldfarb (2016). Variable cadence walking and ground adaptive standing with a powered ankle prosthesis. *IEEE Transactions on Neural Systems and Rehabilitation Engineering 24*(4), 495–505.

[110] Silverman, A. K., N. P. Fey, A. Portillo, J. G. Walden, G. Bosker, and R. R. Neptune (2008). Compensatory mechanisms in below-knee amputee gait in response to increasing steady-state walking speeds. *Gait & posture 28*(4), 602–609.

[111] Simon, A. M., K. A. Ingraham, N. P. Fey, S. B. Finucane, R. D. Lipschutz, A. J. Young, and L. J. Hargrove (2014a). Configuring a powered knee and ankle prosthesis for transfemoral amputees within five specific ambulation modes. *PloS ONE 9*(6), e99387.

[112] Simon, A. M., K. A. Ingraham, N. P. Fey, S. B. Finucane, R. D. Lipschutz, A. J. Young, and L. J. Hargrove (2014b, 06). Configuring a powered knee and ankle prosthesis for transfemoral amputees within five specific ambulation modes. *PLOS ONE 9*(6), 1–10.

[113] Smidt, G. L. (1973). Biomechanical analysis of knee flexion and extension. *Journal of biomechanics 6*(1), 79IN1381–8092.

[114] Sup, F., A. Bohara, and M. Goldfarb (2008). Design and control of a powered transfemoral prosthesis. *Int. J. Robot. Res. 27*(2), 263–273.

[115] Sup, F., H. A. Varol, J. Mitchell, T. J. Withrow, and M. Goldfarb (2009). Preliminary evaluations of a self-contained anthropomorphic transfemoral prosthesis. *IEEE/ASME Transactions on Mechatronics 14*(6), 667–676.

[116] Sup, F. C. and M. Goldfarb (2006). Design of a pneumatically actuated transfemoral prosthesis. In *ASME 2006 International Mechanical Engineering Congress and Exposition*, pp. 1419–1428. American Society of Mechanical Engineers.

[117] Sup IV, F. C. (2009). *A Powered self-contained knee and ankle prosthesis for near normal gait in transfrmoral amputees*. Ph. D. thesis, Vanderbilt University.

[118] Thatte, N. and H. Geyer (2016). Toward balance recovery with leg prostheses using neuromuscular model control. *IEEE Transactions on Biomedical Engineering 63*(5), 904–913.

[119] Tran, M., L. Gabert, M. Cempini, and T. Lenzi (2019). A lightweight, efficient fully powered knee prosthesis with actively variable transmission. *IEEE Robotics and Automation Letters 4*(2), 1186–1193.

[120] Tucker, M. R., J. Olivier, A. Pagel, H. Bleuler, M. Bouri, O. Lambercy, J. del R Millán, R. Riener, H. Vallery, and R. Gassert (2015). Control strategies for active lower extremity prosthetics and orthotics: a review. *J. Neuroeng. Rehabil. 12*(1), 1.

[121] Versluys, R., A. Desomer, G. Lenaerts, M. Van Damme, P. Beyl, G. Van der Perre, L. Peeraer, and D. Lefeber (2008). A pneumatically powered below-knee prosthesis: Design specifications and first experiments with an amputee. In *2008 2nd IEEE RAS & EMBS International Conference on Biomedical Robotics and Biomechatronics*, pp. 372–377. IEEE.

[122] Villarreal, D. J. and R. D. Gregg (2020). Controlling a powered transfemoral prosthetic leg using a unified phase variable. In *Wearable Robotics*, pp. 487–506. Elsevier.

[123] Voloshina, A. S. and S. H. Collins (2020). Lower limb active prosthetic systems—overview. In *Wearable Robotics*, pp. 469–486. Elsevier.

[124] Wang, J., X. Li, T.-H. Huang, S. Yu, Y. Li, T. Chen, A. Carriero, M. Oh-Park, and H. Su (2018). Comfort-centered design of a lightweight and backdrivable knee exoskeleton. *IEEE Robotics and Automation Letters 3*(4), 4265–4272.

[125] Waters, R., J. Perry, D. Antonelli, and H. Hislop (1976). Energy cost of walking of amputees: the influence of level of amputation. *J Bone Joint Surg Am 58*(1), 42–46.

[126] Wensing, P. M., A. Wang, S. Seok, D. Otten, J. Lang, and S. Kim (2017). Proprioceptive actuator design in the mit cheetah: Impact mitigation and high-bandwidth physical interaction for dynamic legged robots. *IEEE Transactions on Robotics 33*(3), 509–522.

[127] Windrich, M., M. Grimmer, O. Christ, S. Rinderknecht, and P. Beckerle (2016). Active lower limb prosthetics: a systematic review of design issues and solutions. *Biomedical engineering online 15*(3), 140.

[128] Winter, D. A. (2009). *Biomechanics and Motor Control of Human Movement* (2 ed.). New York, NY: Wiley.

[129] Winter, D. A. and S. E. Sienko (1988). Biomechanics of below-knee amputee gait. *Journal of biomechanics 21*(5), 361–367.

[130] Wolf, S., G. Grioli, O. Eiberger, W. Friedl, M. Grebenstein, H. Höppner, E. Burdet, D. G. Caldwell, R. Carloni, M. G. Catalano, et al. (2015). Variable stiffness actuators: Review on design and components. *IEEE/ASME transactions on mechatronics 21*(5), 2418–2430.

[131] Yang, U.-J. and J.-Y. Kim (2015). Mechanical design of powered prosthetic leg and walking pattern generation based on motion capture data. *Advanced Robotics 29*(16), 1061–1079.

[132] Yeatman, M., G. Lv, and R. D. Gregg (2019). Decentralized passivity-based control with a generalized energy storage function for robust biped locomotion. *Journal of dynamic systems, measurement, and control 141*(10).

[133] Zhao, H., J. Reher, J. Horn, V. Paredes, and A. D. Ames (2015). Realization of nonlinear real-time optimization based controllers on self-contained transfemoral prosthesis. In *Proceedings of the ACM/IEEE Sixth International Conference on Cyber-Physical Systems*, pp. 130–138. ACM.

[134] Zhu, H., J. Doan, C. Stence, G. Lv, T. Elery, and R. D. Gregg (2017). Design and validation of a torque dense, highly backdrivable powered knee-ankle orthosis. In *IEEE Int. Conf. Robotics Autom.*, pp. 504–510.

[135] Zhu, H., C. Nesler, N. Divekar, M. T. Ahmad, and R. D. Gregg (2019). Design and validation of a partial-assist knee orthosis with compact, backdrivable actuation. In *IEEE Int. Conf. on Rehab. Robot.*

[136] Zmitrewicz, R. J., R. R. Neptune, J. G. Walden, W. E. Rogers, and G. W. Bosker (2006). The effect of foot and ankle prosthetic components on braking and propulsive impulses during transtibial amputee gait. *Archives of physical medicine and rehabilitation 87*(10), 1334–1339.

BIOGRAPHICAL SKETCH

Toby Elery received his BS (2014) and MS (2017) degree in mechanical engineering from The University of Texas at Dallas. He is currently studying to complete his PhD in mechanical engineering at The University of Texas at Dallas. His research is in design innovation for powered prosthetic legs, orthoses, exoskeletons, and assistive devices.

Toby Elery

University of Texas at Dallas
Department of Mechanical Engineering
800 West Campbell Road
Richardson, Tx 75080

toby.elery@utdallas.edu
linkedin.com/in/tobyelery
sites.google.com/view/tobyelery

POSITIONS

Graduate Research Assistant, University of Texas at Dallas — September 2014-Present
Locomotor Control Systems Laboratory

- Lead designer; next generation powered transfemoral prosthetic leg with high-torque, low-impedance actuators
- Designed hardware, software, and power electronics system for prosthetic leg
- Conducted amputee and able-body experiments for device validation

Graduate Teaching Assistant, University of Texas at Dallas — Fall 2015
Feedback Systems in Biomedical Engineering

Undergraduate Research Intern, University of Texas at Dallas — Summer 2014
Locomotor Control Systems Laboratory

EDUCATION

PhD, Mechanical Engineering, University of Texas at Dallas — May 2020
Concentration: Manufacturing & Design Innovation
Dissertation: *Design and Implications of a Robotic Prosthetic Leg with Low-Impedance Actuation*
Advisor: Dr. Robert Gregg

MS, Mechanical Engineering, University of Texas at Dallas
Concentration: Dynamic Systems and Controls — May 2017
Advisor: Dr. Robert Gregg

BS, Mechanical Engineering (cum laude), University of Texas at Dallas — August 2014

RESEARCH INTERESTS

Robotics, Wearable Robots, Prosthetics & Orthotics, Rehabilitation Engineering, Legged Robots

HONORS AND AWARDS

IEEE RAS Travel Grant — March 2018
International Conference on Robotics and Automation

Jonsson School Undergraduate Experience Research Award — August 2014
University of Texas at Dallas

PEER-REVIEWED JOURNAL ARTICLES

1. **T. Elery**, S. Rezazadeh, E. Reznick, L. Gray, and R. Gregg, "Reducing Transfemoral Amputee Hip Compensations with a Powered Prosthesis: A Case Series," IEEE Transactions on Neural Systems & Rehabilitation Engineering, under review.
2. **T. Elery**, E. Reznick, S. Shearin, K. McCain, and R. Gregg, "Design and Validation of a Multiple Degree-of-Freedom Joint for an Ankle-Foot Orthosis," ASME Journal on Medical Devices, under review.
3. **T. Elery**, S. Rezazadeh, C. Nesler, and R. Gregg, "Design and Validation of a Powered Knee-Ankle Prosthesis with High-Torque, Low-Impedance Actuators," *IEEE Transactions on Robotics*, 2020, conditionally accepted.

PEER-REVIEWED CONFERENCE PROCEEDINGS

1. **T. Elery**, S. Rezazadeh, C. Nesler, J. Doan, H. Zhu, and R. Gregg, "Design and Benchtop Validation of a Powered Knee-Ankle Prosthesis with High-Torque, Low-Impedance Actuators," Accepted to IEEE Int Conf Robotics & Automation, Brisbane, Australia, 2018. (41% acceptance rate)
2. H. Zhu, J. Doan, C. Stence, G. Lv, **T. Elery**, and R. Gregg, "Design and Validation of a Torque Dense, Highly Backdrivable Powered Knee-Ankle Orthosis," in IEEE Int Conf Robotics & Automation, Singapore, pp. 504-510, 2017. (41% acceptance rate)
3. G. Lv, H. Zhu, **T. Elery**, L. Li, and R. Gregg, "Experimental Implementation of Underactuated Potential Energy Shaping on a Powered Ankle-Foot Orthosis," in IEEE Int Conf Robotics & Automation, Stockholm, Sweden, pp. 3493-3500, 2016. (34.7% acceptance rate)

PATENTS

"Powered Prosthesis with Torque Dense, Low Ratio Actuation." R. Gregg, **T. Elery**, C. Nesler, S. Rezazadeh. U.S. patent app. 16/398,895, 2019.

MENTORING

Undergraduate Senior Design Teams

1. Enhanced Design of Robotic Leg, Technical Manager, 2017-18
2. Multi-Degree-of-Freedom Ankle-Foot Orthosis, Technical Manager, 2015-16

Graduate Researchers

1. Zhiqi (Jim) Mao, PE, 2019-2020 (ME intern)

Undergraduate Researchers

1. Kayla Shepodd 2019 (ME intern)
2. Lukas Zekarias 2017-2018 (EE intern)
3. Parikshit Krishnia 2017-2018 (EE intern)
4. Philip Katterjohn 2016-2017 (ME intern)
5. David Merz 2016-2017 (ME intern)
6. Emanuel Grella-2016-2017 (ME intern)
7. Anurag Madan 2016-2017 (EE intern)

8. Patterson Kaduvinal Abraham 2015 (ME intern)
9. Jeremiah Plauche 2015 (ME intern)
10. Yulin Yang 2015 (ME intern)
11. Caitlyn Conley 2014 (Summer intern)

UT Dallas – Mexico Summer Research Program
1. Juan Maldonado Jáuregui 2017
2. Oscar Alejandro Martínez Mancilla 2016

SCHOLARLY REVIEW

Journal Reviewer
IEEE Transactions on Robotics, ASME Journal of Mechanical Design, ASME Applied Mechanics Reviews

Conference Reviewer
IEEE Conference on Robotics and Automation, IEEE International Conference on Engineering in Medicine and Biology Society, International Conference on Rehabilitation Robotics

TRAINING AND CERTIFICATIONS

Certified Solidworks Associate (CSWA) - Mechanical Design, ID: C-XFPY9R8YMK 2015
NIH Responsible Conduct of Research (RCR) Training, University of Texas at Dallas 2018

PROFESSIONAL MEMBERSHIPS

Student Member, Institute of Electrical & Electronics Engineers (IEEE)
- Robotics & Automation Society

VOLUNTEER EXPERIENCE

Site Development & Facilities Committee Chair, Hidden Acres Retreat Center 2018-Present
- Organized and lead committee meetings to plan, schedule, and execute ongoing development projects
- Coordinated, from concept to completion, the development of a 1500 sq. ft. building in ~1 year

REFERENCES

Professional
1. Robert D. Gregg, Ph.D., University of Michigan, Associate Professor
   Department of Electrical Engineering and Computer Science, Robotics Institute
   Email: rdgregg@umich.edu, Phone: (510) 872-9096
2. Siavash Rezazadeh, Ph.D., University of Denver, Assistant Professor
   Department of Mechanical & Materials Engineering
   Email: siavash.rezazadeh@du.edu, Phone: (303) 871-6587
3. Yonas Tadesse, Ph.D., University of Texas at Dallas, Associate Professor
   Department of Mechanical Engineering
   Email: yonas.tadesse@utdallas.edu, Phone: (972) 883-4556

Personal

4. Tim Carpenter, Hidden Acres, Executive Director
   Email: tcarpenter@hiddenacres.org, Phone (214) 673-5117
5. Matt Arnett, Omni Signs & Graphics, Owner
   Email: Omnisignsandgraphics@gmail.com, Phone: (432) 631-1741